UNIVERSIDADE FEDERAL DE PERNAMBUCO
DEPARTAMENTO DE FÍSICA – CCEN
PROGRAMA DE PÓS-GRADUAÇÃO EM FÍSICA

MELISSA ESTHER MALDONADO CANTILLO

LINEAR AND NONLINEAR OPTICAL CHARACTERIZATION OF PLASMONIC NANOSTRUCTURES OF GOLD NANORODS AND METASURFACES

Recife
2017

MELISSA ESTHER MALDONADO CANTILLO

LINEAR AND NONLINEAR OPTICAL CHARACTERIZATION OF PLASMONIC NANOSTRUCTURES OF GOLD NANORODS AND METASURFACES

Tese apresentada ao Programa de Pós-Graduação em Física da Universidade Federal de Pernambuco, como requisito parcial para a obtenção do título de Doutora em Física.

Orientador:
Prof. Dr. Anderson Stevens Leônidas Gomes
Universidade Federal de Pernambuco

:

Recife
2017

Catalogação na fonte
Bibliotecário Jefferson Luiz Alves Nazareno CRB 4-1758

M244l Maldonado Cantillo, Melissa Esther.
Linear and nonlinear optical characterization of plasmonic nanostructures of gold nanorods and metasurfaces / Melissa Esther Maldonado Cantillo – 2017.
104f.: fig.; tab.

Orientador: Anderson Stevens Leônidas Gomes.
Tese (Doutorado) – Universidade Federal de Pernambuco. CCEN. Física. Recife, 2017.
Inclui referências e apêndices.

1. Óptica. 2. òptica não linear. I. Gomes, Anderson Stevens Leônidas. (Orientador). II. Titulo.

535.2 CDD (22. ed.) UFPE-FQ 2017-53

MELISSA ESTHER MALDONADO CANTILLO

LINEAR AND NONLINEAR OPTICAL CHARACTERIZATION OF PLASMONIC NANOSTRUCTURES OF GOLD NANORODS AND METASURFACES

Tese apresentada ao Programa de Pós-Graduação em Física da Universidade Federal de Pernambuco, como requisito parcial para a obtenção do título de Doutora em Física.

Aprovada em: 07/07/2017.

BANCA EXAMINADORA

Prof. Dr. Anderson Stevens Leônidas Gomes
Orientador
Universidade Federal de Pernambuco

Prof. Dr. Cid Bartolomeu de Araújo
Examinador Interno
Universidade Federal de Pernambuco

Prof. Dr. Edilson Lucena Falcão Filho
Examinador Interno
Universidade Federal de Pernambuco

Prof. Dr. Paras Nath Prasad
Examinador Externo
Universidade de Buffalo

Prof. Dr. Jake Fontana
Examinador Externo
Laboratório de Pesquisa Naval dos Estados Unidos

"Educação não transforma o mundo, a educação muda pessoas...

Pessoas transformam o mundo".

Paulo Freire.

Resumo

Nanopartículas (NPs) dielétricas e/ou metálicas têm sido pesquisadas intensamente ao longo das últimas décadas devido a suas propriedades elétricas, ópticas e magnéticas. Um dos aspectos importantes no estudo de NPs metálicas está na ressonância de plasmon de superfície resultante da interface metal/dielétrico. Uma NP assimétrica como um nanobastão pode ser excitada em dos modos dipolares dependendo da polarização da luz incidente. A forma, o tamanho e a escolha do metal das NP são fatores importantes para determinar a resposta do material, e o controle destas propriedades conduzem a aplicações especificas. Como o modo longitudinal (LSPR) é o mais atraente do ponto de vista das aplicações, cresce o interesse de orientar/alinhar as partículas para aumentar a eficiência das suas propriedades ópticas. Por outro lado, metamateriais – materiais projetados com características não encontradas na natureza – utilizando nanoestruturas metálicas tem sido objeto de pesquisa recente, com inúmeras aplicações. Nesta tese foram caracterizadas amostras de nanobastões de ouro orientados em um filme fino de Polyvinyl alcohol (PVA), nanobastões de ouro em óleo Cargille e metasuperficies de ouro em substrato de vidro. Num primeiro trabalho os nanobastões de ouro em um filme de PVA foram mecanicamente esticado, produzindo amostras anisotrópicas. As amostras apresentaram uma forte anisotropia e um fator de engrandecimento da absorção não linear – um fator de ~ 57 com relação à amostra isotrópica – que ainda não havia sido descrito na literatura. Os dados experimentais foram reproduzidos a partir de simulação numérica, com um ótimo acordo teoria/experimento. A origem deste aumento foi entendida como sendo devido à presença de clusters com número especifico de nanobastões. Dependendo da polarização da luz incidente, verificou-se também a inversão do sinal da refração não linear, o que faz nosso material muito atraente desde o ponto de vista das aplicações como chave ultrarrápida de polarização. Em um segundo experimento, também conseguimos fazer o controle óptico de nanobastões de ouro em óleo Cargille com a ajuda da aplicação de um campo elétrico e medimos suas propriedades ópticas não lineares. Em um terceiro trabalho, foram estudadas metasuperficies de ouro com separação entre as NPs de 0.6nm. Estes metamateriais foram preparados por um método de auto-montagem, e apresentaram índice de refração linear variando entre 0.87 até 4.2. Devido às propriedades da metasuperficie, um índice de refração não linear negativo foi medido. O valor de n_2 é pelo menos duas ordens de grandeza maior que outras nanoestruturas de ouro, conforme dados disponíveis na literatura. O índice de absorção não linear negativo correspondendo a absorção saturada foi medido. O valor de β_2 pode ser considerado típico quando comparado a outras NPs de ouro, Todas as medidas foram realizadas com pulsos de 100fs, 800nm a taxas de repetição de 20Hz, 1kHz e 76MHz. A técnica Z-scan e uma técnica conhecida como Beam Collimated Hartmann-Shack foram utilizadas para os estudos de óptica não linear.

Palavras-chave: Metasuperficies. Nanobastões de ouro. Óptica Não Linear. Plasmonica.

Abstract

Particles with characteristic length less than one hundred nanometers are known as nanoparticles (NP). Dielectric and/or metallic nanoparticles have been investigated in the last decades based on their electrical, optical and magnetic properties. One of the most important aspects in the study of metal nanoparticles is the surface plasmon resonance (SPR), an effect that occurs at the metal-dielectric interface, where the dielectric is the material that hosts the nanoparticles. The shape, size, and choice of the metal are important factors for determining the response of the material and the control of these characteristics for specific applications. Configurations that lead to the production of materials or metamaterials with different features from those known in the current literature are intended for new technological applications. In this thesis, we studied samples of gold nanorods oriented in a thin-film of Polyvinyl alcohol (PVA), Nanorods in Cargille oil and Gold metasurfaces in a glass substrate. In a first work, the PVA film was mechanically stretched, producing gold nanorods anisotropically distributed. The high anisotropy implies in this case that the non-linear absorption increases about fifty-seven times in comparison to the isotropic sample. We reported for the first time in the scientific literature this effect. Our experimental results were corroborated through numerical simulations, leading to very good agreement. Based on our research we attribute that the increase in the nonlinear absorption is due to the presence of clusters of a specific nanorods number. We verify the inversion of the nonlinear refractive signal as a function of the polarization of the incident light, a condition by which our material becomes an optimal candidate for making ultra-fast polarization keys. In a second experiment, we did optical control of gold nanorods suspended in Cargille oil, by applying an electric field we measured its nonlinear optical properties. In a third work, we characterized metasurfaces of gold where the average separation between nanoparticles is estimated to be 0.6nm. The metamaterials were prepared by a self-assembly method. The linear refractive index can vary from 0.87 to 4.2. The properties of these metasurfaces lead to a negative nonlinear refractive index. Therefore, it is a material with high self-defocusing. We measured a nonlinear negative absorption index of β_2, corresponding to saturated absorption. The value of β_2 is considered typical when compared to other gold nanoparticles, while the value of n_2 is approximately two magnitude orders greater. We used incident laser pulses with 100fs and 800nm, using repetition rates of 20Hz, 1kHz and 76MHz. The experimental techniques used were conventional Z-scan and Beam Collimated Hartmann-Shack for the studies of nonlinear optics.

Keywords: Metasurfaces. Gold Nanorods. Nonlinear Optics. Plasmonics.

Nomenclature

CS_2	Carbon Disulfide
AuNRs	Gold Nanorods
C5	Defocalization coefficient
CA	Closed Aperture
CA/CO	Closed Aperture divided by Open Aperture
CCD	Charge-Coupled Device
CW	Continuous Wave
FFT	Fast Fourier Transform
FOM	Figure of Merit fs Femtosecond
FWHM	Full Width at Half Maximum
FWM	FourWave Mixing
GNR	Gold Nanorod
GW	Gigawatt
HS	Hartmman-Shack
HSWFS	Hartmann-Shack Wavefront sensor
ITO	Indium Tin Oxide
kHz	KiloHertz
kV	Kilovolts
L-LSPR	Longitudinal Local Surface Plasmon Resonance
MHz	Megahertz
MLA	Microlenses Array
MW	Megawatt
NIR	Near-Infrared

NL	Nonlinear
NLA	Nonlinear Absorption
NLO	Nonlinear Optics
NLR	Nonlinear Refraction
OA	Open Aperture
OD	Optical Density
PMLs	Perfectly matched layers
PVA	Polyvinyl alcohol SA Saturation Absorption
SAXS	Small-Angle X-ray scattering
SHG	Second Harmonic Generation
SPR	Surface Plasmon Resonance
T-LSPR	Transversal Local Surface Plasmon Resonance
TEM	Transmission Electron Microscopy
THF	Tetrahydrofuran
TPA	Two Photon Absorption
UV-Vis	UltraViolet to Visible
WFS	Wavefront Sensor
WLC	White-Light Continuum

List of Figures

Lists of Tables

Contents

1 Introduction

Metal nanostructures are well known to produce colors, due to their strong light absorption and scattering in the visible region of the spectrum. This effect is caused by one of the most important types of interactions of metal nanoparticles with the electromagnetic field, known as plasmons. Metals are characterized by the presence of free electrons, which can be promoted via intraband transitions to empty energy levels in the same band or to empty levels of an empty overlapping band, via absorption of low energy photons. An incident electromagnetic field can elicit collective oscillations of these free electrons [1, 2, 3, 4]. Such oscillations become quickly resonant with the electromagnetic field, and the energy from the incoming radiation is absorbed and transformed into heat (absorption) and back into light (scattering). These collective and coherent oscillations of electrons cause a displacement of the electrons from the nuclei, leading to the formation of various possible distributions in the surface charges (Figure 1.0.1). This in turn creates Coulomb interactions between positive and negative charges, which induce restoring oscillating forces acting on these free electrons. Each type of surface charge distribution is characterized by a collective oscillation mode, also termed as localized surface plasmon resonance (SPR). Various factors influence the possible types of SPRs in nanostructures and the frequencies at which they are observed.

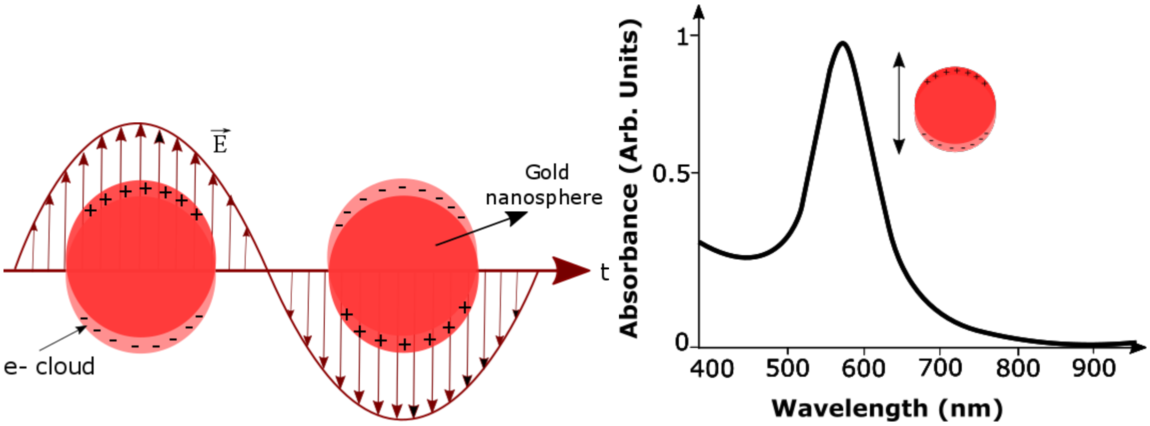

Figure 1.0.1: Localized surface plasmon resonance for spherical nanoparticle.

For nanoparticles with diameters between 10 and $30nm$, the dominant effect in the visible region is the excitation of plasmon modes. In this size regime, and in the simple case of spherical nanoparticles, basically a single plasmon mode of dipolar characters excited and its wavelength is independent of particle size, but is strongly dependent on the dielectric function of the surrounding medium, and also the width of the plasmon resonance band remains poorly correlated with size. For particles smaller than $10nm$, a size that is significantly smaller than the mean free path of electrons, free electrons collide frequently with the surface of the nanoparticles, and this leads to broadening of the plasmon resonance band due to dephasing effects. At sizes above $30nm$ other effects become non-negligible, like retardation, which lead to broadening and loss in intensity of the plasmon band, as well as to a spectral shift in the red. At sizes above $100nm$, the optical properties are dominated by scattering of light. In addition, higher order modes (i.e. quadrupolar, octupolar) start contributing to absorption.

The shape of metal nanoparticles has perhaps the most striking influence on their optical properties. As an example, in rod shape nanoparticles the plasmon mode can be selectively excited in two dipolar SPR modes (see Figure 1.0.2), depending on the polarization direction of the incident light: longitudinal (LSPR) or transverse (TSPR) with respect to the long-axis of the NRs. The most attractive from the application standpoint is the longitudinal one, because it can be excited within a much larger wavelength range, from mid-visible to near-infrared.

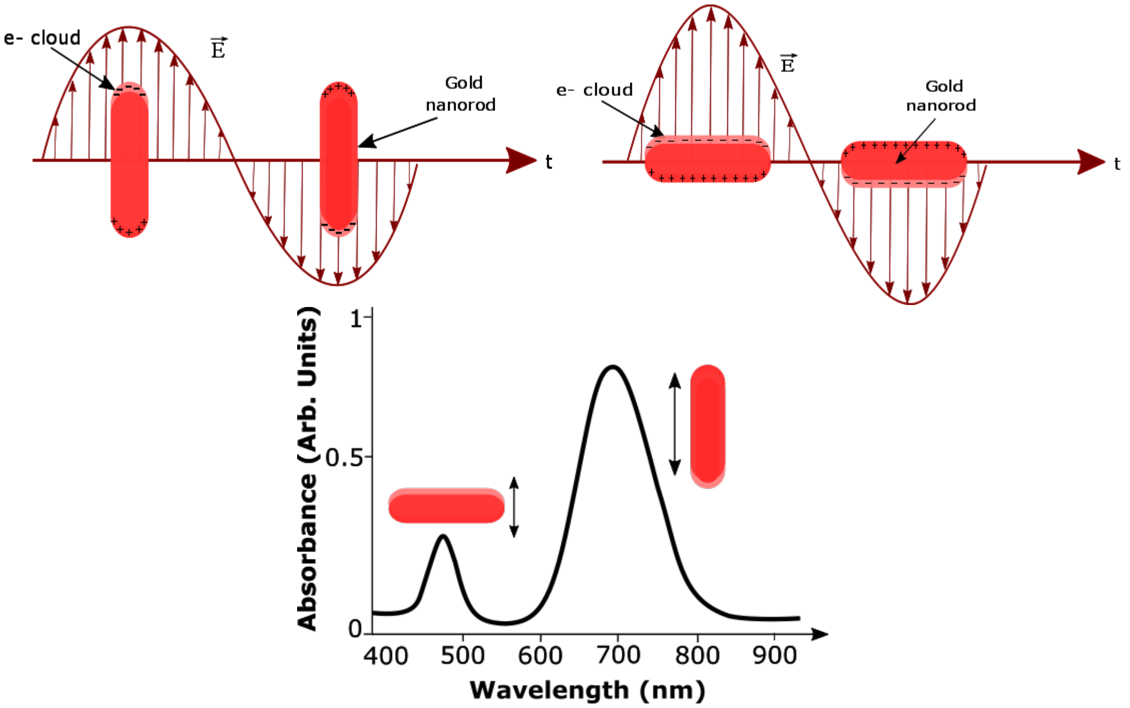

Figure 1.0.2: Localized surface plasmon resonance for nanorod. The nanorod has two modes of SPR. A longitudinal (L-SPR) and transversal (T-SPR) mode.

The L-SPR strongly depends on the nanorod aspect ratio R, which is defined as the length of the rod divided by the width of the rod ($R = L/d$). The simulated absorption spectra of gold nanorods with varying aspect ratios is shown in Figure 1.0.3a. The medium dielectric constant was chosen to be a fixed value of 4. The maximum of the transverse mode shifts to shorter wavelength when increasing aspect ratio. On the other hand, the maximum of the L-SPR red-shifts 150 nm when the aspect ratio is increased from 2.6 to 3.6. Furthermore, the increase in the peak position of the longitudinal plasmon band with increasing nanorod aspect ratio follows a linear trend, which is illustrated in the inset of the Figure 1.0.3. In Figure 1.0.3b) is plotted the absorption espectra for different values of the medium dielectric constant with a fixed aspect ratio of 3.3. In this case both maxima shift to longer wavelength and the intensity of both resonances increases with an increasing medium dielectric constant. Again, the longitudinal mode is more sensitive.

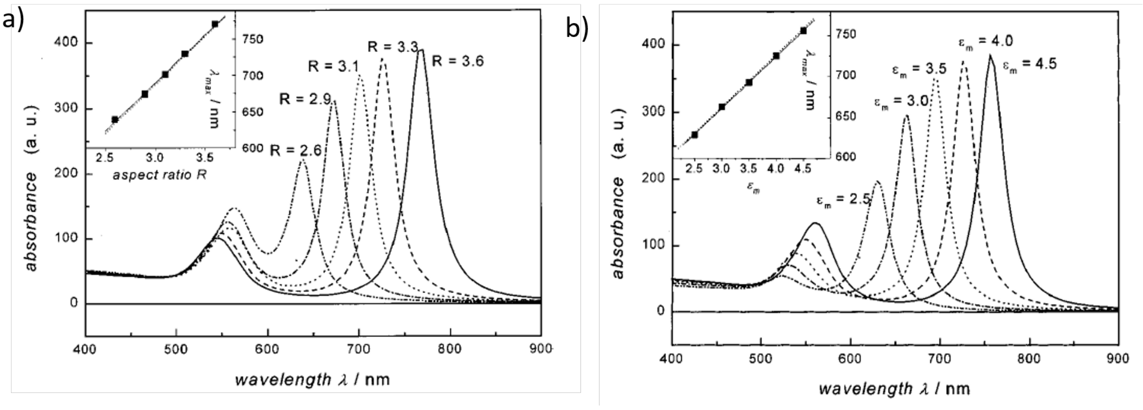

Figure 1.0.3: a) Absorption spectra of elongated elipsoids with varying aspects ratios R. The medium dielectric constant was fixed at a value of 4. The inset shows a plot of the maximum of the L-SPR as a function of the aspect ratio. b) Absorption spectra of elongated elipsoids with varying medium dielectric constant ϵ. The aspect ratio was fixed at a value of 3.3. The inset shows a plot of the maximum of the L-SPR as a function of the medium dielectric constant [5].

When the NRs are randomly oriented or misaligned, their optical properties are averaged out and the nanostructures functionalities are less effective. Applications based on the excitation of the LSPR of NR-structures can work at their highest efficiency only if they use either a single rod or an ensemble of fully aligned ones [6]. But, applications based on single NRs would still require some more expensive equipment and would be difficult to be miniaturized and implemented in practical devices.

The *directional growth* of AuNRs, starting from seeds implanted on different substrates was studied as well, but this method could not provide a transparent substrate [7, 8]. Another method is to use the *electric field* to induce alignment moments in AuNRs suspended in liquid solutions. In this case it was shown to require very high field strengths. However, besides generating alignment moments, the electric field also induced dielectrophoretic forces in the rods, which caused their accumulation around the electrodes and hence a nonuniform spatial distribution [9]. Another method used for alignment of AuNRs is the *uniaxial stretching*. It consists in embedding the rods in a thin film of thermoplastic polymers, such as polyvinyl alcohol (PVA), heating up the composite film to its glass transition temperature (softening temperature of the polymer) and stretching it uniaxially [6].

In the search of materials ordered to increase the efficiency of the optical properties arises the need to talk about metamaterials. Metamaterials comprise periodically or randomly distributed artificial structures with the size and spacing much smaller than the wavelength of interest [10, 11]. Because most metamaterials are composed of metals, the plasmonic effect of metals plays an important role in optical metamaterials.

The unique properties of metamaterials based on strong field enhancement, promise a variety of novel applications in biomedical sensing [8, 12], super-resolution imaging [13], and next-generation optical circuits [14].

The enhancement of the linear properties leads to the enhancement of the nonlinear properties of this materials. Third-order nonlinear optical effects are the physical basis of a number of applications in future high-capacity communication networks1 in which ultrafast switching, signal regeneration, and high-speed demultiplexing would be performed all-optically through the use of third order optical nonlinearities. Optimization of the design of these materials for a given application depends, to a large extent, on comprehension of the physical mechanisms responsible for the nonlinear response.

Gold nanoparticles can be applied as NLO materials because it is expected that the particles show large third-order nonlinear optical properties enhanced in the vicinity of the SPR wavelength.

In the search of materials ordered to increase the efficiency of the optical properties we study in this thesis films of Gold NRs in PVA [15], Gold nanorods suspended in Cargille oil [16] and the new structures called metasurfaces [17].

2 Measurement techniques

In this chapter, we describe the measurements methods used to characterize the optical materials employed. Optical density, Small Angle X-Ray Scattering (SAXS) [18, 19, 20, 21], Spectroscopy ellipsometry [22, 23, 24, 25], Z-scan [26, 27, 28, 29] and Beam collimated Hartmann-Shack [30].

2.1 Linear Techniques

Typically, the first step in characterizing a material is to determine its linear optical properties. This data is used to identify wavelength regions of low one photon absorption (1PA), which are of interest for nonlinear spectroscopy.

2.1.1 Linear Optical Properties

When light is incident on a sample in a cuvette, it can be transmitted, absorbed, or scattered. This is often written as $T+A+S=1$ due to conservation rules. Transmission is the light that passes through the sample without interacting with it. Light that encounters a molecule or particle can be either absorbed or scattered. Elastic scattering occurs when the interaction changes the direction of light, but not its wavelength or energy.

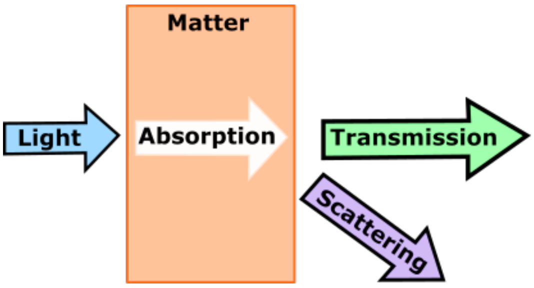

Figure 2.1.1: Interaction of light and matter.

When an absorption measurement is made, however, it is assumed that scatter is zero, in which case all light not transmitted to the detector is absorbed by the sample, i.e., $T+A=1$. This is true for the ideal case of an infinitely dilute solution of infinitely small particles in a transparent solvent. Luckily, it is also reasonably accurate in practice for a wider range of absorbing substances, solvents and concentrations. Absorbance occurs when the light encountering the molecule in the solvent matches the frequency of molecular vibrations or transitions in electronic energy level states within the molecule. The chance of this happening is dependent on the cross section of the molecule for a particular energy level transition and determines how absorptive a molecule is in solution. The more concentrated the solution, the greater the chance that a photon traveling through the solution will be absorbed. In fact, the probability of absorption increases linearly with both the pathlength and concentration of the solution, a relationship which has been quantified in the Beer-Lambert Law, also known as Beer's Law.

Beer Law

Beer's Law (also called the Beer-Lambert law) says that the absorbance of a solution will depend directly on the concentration of the absorbing molecules and the pathlength traveled by light through the solution.

$$A(\lambda) = \varepsilon(\lambda)cl \tag{2.1.1}$$

where, $A(\lambda)$ is the linear absorption of the solution as a function of wavelength, $\varepsilon(\lambda)$ is the extinction coefficient of the absorbing molecule as a function of wavelength in $[mol/L]$, c is the concentration of the solution and l is the pathlength traveled by the light beam through the solution in $[cm]$.

By measuring the transmission through the sample we can determine the amount of light absorbed. Provided the sample has low scatter (as with a relatively dilute, clean solution), almost all of the light not absorbed will be transmitted. Transmission is the ratio of incident intensity, I_0 to transmitted intensity, I, and will decrease with increasing path length or concentration.

$$T = \frac{I}{I_0} = e^{-\varepsilon lc} \tag{2.1.2}$$

By taking the negative log_{10} of each side of this equation, we get a linear absorbance equation that is useful for calculations from measurements.

$$A(\lambda) = -logT = \varepsilon(\lambda)cl \tag{2.1.3}$$

A perfectly transparent sample (T = 100%) will have an absorbance value of zero, while a perfectly opaque sample (T = 0%) will have an absorbance value of infinity. When units are specified, absorbance is usually described in terms of absorbance units (AU) or optical density (OD). The linearity of absorbance makes it conveniently additive.

2.1.2 Small Angle X-Ray Scattering (SAXS)

The interaction of radiation with inhomogeneities in matter can cause a small deviation of the radiation from its incident direction, called small-angle scattering (See Figure (2.1.2)).

Such small-angle scattering (SAS) occurs in all kinds of materials, be they (partially) crystalline or amorphous solids, liquids or even gases, and can take place for a wide variety of radiation, such as electrons (SAES) [31], gamma rays (SAGS) [32], light (LS) [19], x-rays (SAXS) [19, 18, 21, 20] and even neutrons (SANS) [19, 20].

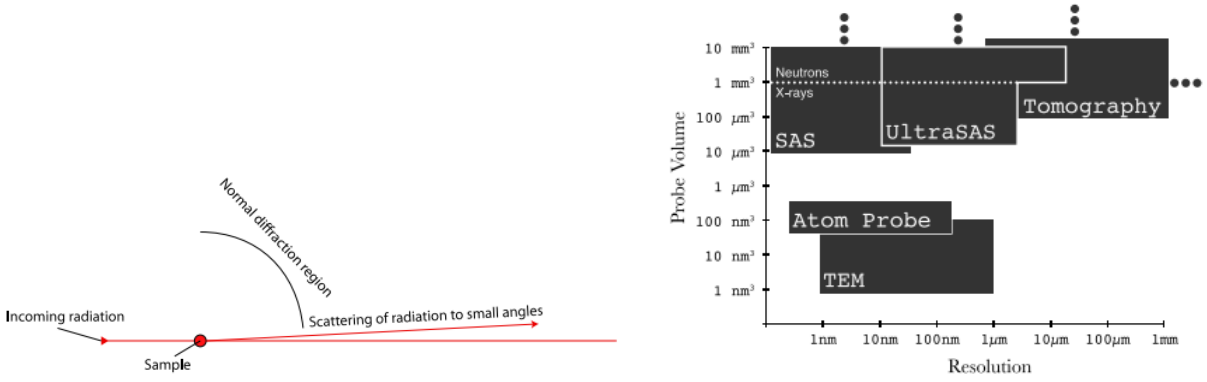

Figure 2.1.2: a) The scattering of radiation to small angles by a sample (SAS). b) Typical size range of distinguishable nanostructural features (horizontal axis) and sampling volume (vertical axis) of various volumetric techniques. [33]

The Figure 2.1.2b) shows the typical size range of distinguishable nanostructural features and sampling volume of various volumetric techniques: transmission electron microscopy (TEM), atom probe (AP), tomography and small-angle and ultra-small-angle scattering techniques (SAS/ultraSAS).

SAXS is a well-known technique to characterize the nanometer scale microstructure of polymer [34]. SAXS is a study of X-ray scattering in reciprocal space at angles very close to the main beam, typically $2\theta < 2°$, where θ is half the scattering angle. This technique depends on the occurrence of large-scale $(10–500)Å$ periodic heterogeneity in the structure and can provide a broad range of structural features [18, 33]. It also measures the distance in the range of hundreds of angstrom units. Most frequently, the only cooperative reflections that usually appear in the SAXS patterns occur because of the periodic arrangement of the sample along the axis direction. Therefore, SAXS is an ideal technique to investigate the orientation of lamellae with respect to the fabrication or stretching direction [21].

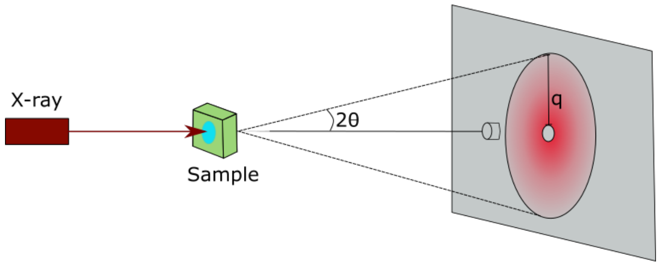

Figure 2.1.3: Schematic of the SAXS instrument. SAXS tipically recorded as a function of momentum transfer $q = 4\pi \sin\theta/\lambda$, where 2θ is the total scattering angle and λ is the X-ray wavelength.

A schematic of the experimental set-up is shown in Figure 2.1.3. A collimated, monochromatic X-ray beam incident on the sample generates scattered x-rays, which are imaged by detector. The transmitted beam usually blocked by a beamstop, resulting in a shadow in the image. The SAXS scattering data are collected in the form of a 2-D image. A radial average is then performed on the 2-D scattering pattern, which is a quantitative measure of the intensity of X-ray scattering. From the radial average plots, the orientation function is determined using Herman's orientation function.

Herman's Orientation Function

For uniaxial orientation, the orientation distribution function of chain segments is defined by a series of orthogonal spherical harmonic orientation functions. Crystalline orientation will be characterized in terms of average squared cosine values that represent the average orientation of the normal to the crystalline plane with respect to each of the reference axes. The second harmonic orientation function is known as Herman's orientation function and is given by [35]

$$f = \frac{1}{2}\left\langle 3\cos^2\theta - 1\right\rangle, \tag{2.1.4}$$

where θ is the angle between the stretching direction and the longitudinal axis of aggregate, and $\langle\cos^2\theta\rangle$ is the averaging over all θ given by

$$\left\langle \cos^2\theta \right\rangle = \frac{\int_0^{2\pi} I(\theta)\cos^2\theta \sin\theta d\theta}{\int_0^{\pi/2} I(\theta)\sin\theta d\theta}. \tag{2.1.5}$$

Where $I(\theta)$ is the intensity in photons and is defined as

$$I(\theta) = \int_0^{2\pi} I(\theta,\beta) d\beta. \tag{2.1.6}$$

$I(\theta,\beta)$ represents the intensity distribution measured on the pole figure of the (hkl) plane as a function of the angle a $\alpha\,(\pi/2 \geq \alpha \geq 0)$ where $\alpha = \pi/2 - \theta$; and $\beta\,(2\pi \geq \beta \geq 0)$. When the chains are perfectly aligned along the reference axis, $f = +1 (\theta = 0°)$; whereas $f = -1/2$ for chains aligned perfectly normal to the reference axis $(\theta = 90°)$. For a perfect random orientation, $f = 0$ [36].

2.1.3 Spectroscopic Ellipsometry

Ellipsometry measures a change in polarization as light reflects or transmits from a material structure. The polarization change is represented as an amplitude ratio, Ψ, and the phase difference, Δ. The measured response depends on optical properties and thickness of individual materials. Thus, ellipsometry is primarily used to determine film thickness and optical constants. However, it is also applied to characterize composition, crystallinity, roughness, doping concentration, and other material properties associated with a change in optical response.

Since the 1960s, as ellipsometry was developed to provide the sensitivity necessary to measure nanometer-scale layers used in microelectronics, interest in ellipsometry has grown steadily. Today, the range of its applications has spread to the basic research in physical sciences, semiconductor and data storage solutions, flat panel display, communication, biosensor, and optical coating industries. This widespread use is explained by increased dependence on thin films in many areas and the flexibility of ellipsometry to measure most material types: dielectrics, semiconductors, metals, superconductors, organics, biological coatings, and composites of materials.[1]

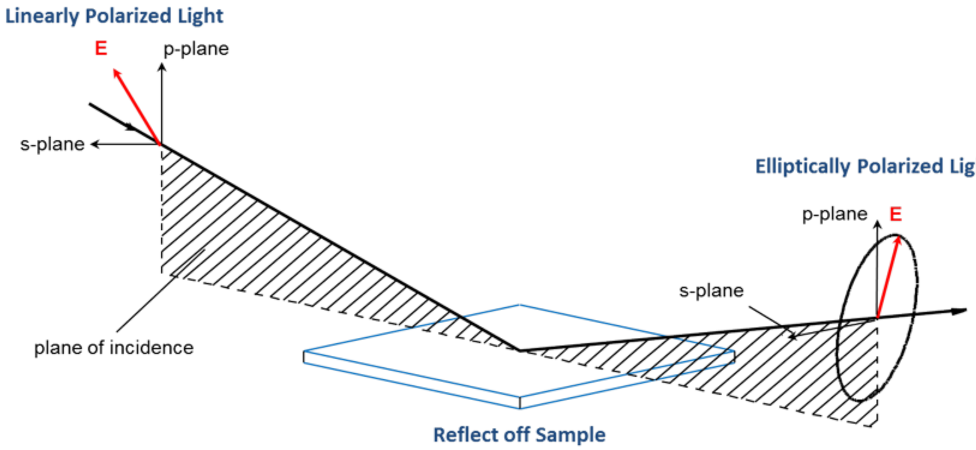

Figure 2.1.4: Basic setup for the ellipsometry[25].

Polarized light

Light can be described as an electromagnetic wave traveling through space. For purposes of ellipsometry, it is adequate to discuss the waves's electric field behavior in space and time, also known as polarization. The electric field of a wave is always orthogonal to the

---

[1] This tutorial provided by the J. A. Woollam Co. is an introduction to ellipsometry for anyone interested in learning more about ellipsometry and its applications. It provides a fundamental description of ellipsometry measurements along with the typical data analysis procedures. The primary applications of ellipsometry are also surveyed. `https://www.jawoollam.com/resources/ellipsometry-tutorial`

propagation direction. Therefore, a wave traveling along the z-direction can be described by its $x-y$ components. When the light has completely random orientation and phase, it is considered unpolarized. For ellipsometry, however, we are interested in the kind of electric field that follows a specific path and traces out a distinct shape at any point. This is known as polarized light. When two orthogonal light waves are in-phase, the resulting light will be linearly polarized. The relative amplitudes determine the resulting orientation. If the orthogonal waves are 90° out-of-phase and equal in amplitude, the resultant light is circularly polarized. The most common polarization is "elliptical", one that combines orthogonal waves of arbitrary amplitude and phase. This is where ellipsometry gets its name.

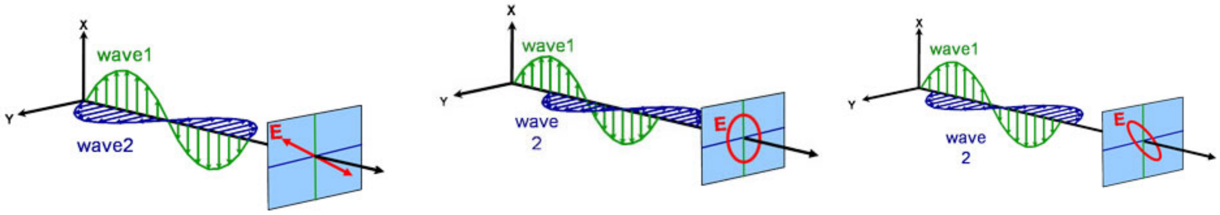

Figure 2.1.5: Orthogonal waves combined to demonstrate polarization: a) Lineal polarization, b) Circular Polarization and c) Elliptical polarization [25].

Light and materials

Two values are used to describe the optical properties which determine how light interacts with a material. They are generally represented as a complex number. The complex refractive index ($\tilde{n}$) consists of the index (n) and extinction coefficient (k):

$$\tilde{n} = n + ik \tag{2.1.7}$$

Alternatively, the optical properties can be represented as the complex dielectric function:

$$\tilde{\varepsilon} = \varepsilon_1 + i\varepsilon_2 \tag{2.1.8}$$

with the following relation between conventions:

$$\tilde{\varepsilon} = \tilde{n}^2 \tag{2.1.9}$$

The index describes the phase velocity of light as it travels in a material compared to the speed of light in vacuum, c:

$$v = \frac{c}{n} \tag{2.1.10}$$

Light slows as it enters a material with higher index. Because the frequency of light waves remains constant, the wavelength will shorten. The extinction coefficient describes the loss of wave energy to the material. It is related to the absorption coefficient, as:

$$\alpha = \frac{4\pi k}{\lambda} \tag{2.1.11}$$

Light loses intensity in an absorbing material according to Beer's Law:

$$I(x) = I_0 e^{-i\alpha x} \tag{2.1.12}$$

Thus, the extinction coefficient relates how quickly light vanishes in a material. These concepts are demonstrated in Figure 2.1.6 where a light wave travels through two different materials of varying properties before returning to the ambient.

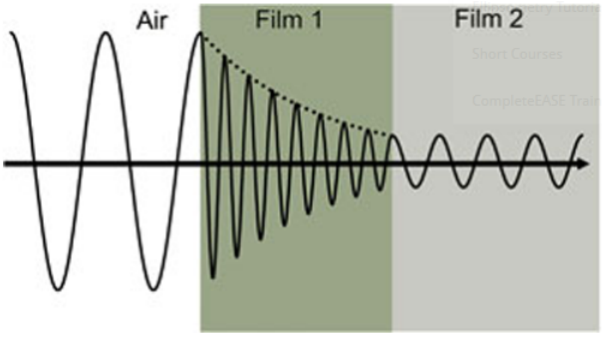

Figure 2.1.6: Wave travels from air into absorbing Film 1 and then transparent Film 2. The phase velocity and wavelength change in each material depending on index of refraction (Film 1: $n = 4$, Film 2: $n = 2$) [25].

Figure (2.1.7) shows the basic setup in order to calculate the refractive index. Maxwell's equations must remain satisfied when light interacts with a material, which leads to boundary conditions at the interface. Incident light will reflect and refract at the interface, as shown in the figure below. The angle between the incident ray and sample normal (θ_i) will be equal to the reflected angle, (θ_r). Light entering the material is refracted at an angle θ_t given by:

$$n_i \sin\theta_i = n_t \sin\theta_t \tag{2.1.13}$$

by means of simple geometrical manipulations, an expression for $cos(\theta_t)$ can be deduced

$$cos(\theta_t) = \sqrt{1 - \left(\frac{n_i}{n_t}\right)^2 \sin^2(\theta_i)} \tag{2.1.14}$$

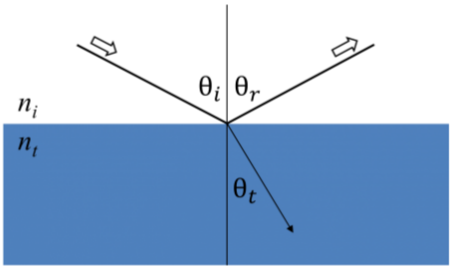

Figure 2.1.7: Light reflects and refracts according to Snell's law.

The same occurs at each interface where a portion of light reflects and the remainder transmits at the refracted angle. The boundary conditions provide different solutions for electric fields parallel and perpendicular to the sample surface. Therefore, light can be separated into orthogonal components with relation to the plane of incidence. Electric fields parallel and perpendicular to the plane of incidence are considered $p-$and $s-$ polarized, respectively. These two components are independent and can be calculated separately. Fresnel described the amount of light reflected and transmitted at an interface between materials:

$$r_p = \frac{E_{rp}}{E_{ip}} = \frac{n_t \cos\theta_i - n_i \cos\theta_t}{n_t \cos\theta_i + n_i \cos\theta_t} \tag{2.1.15}$$

$$t_p = \frac{E_{tp}}{E_{ip}} = \frac{2n_i \cos\theta_i}{n_t \cos\theta_i + n_i \cos\theta_t} \tag{2.1.16}$$

$$r_s = \frac{E_{rs}}{E_{is}} = \frac{n_i \cos\theta_i - n_t \cos\theta_t}{n_i \cos\theta_i + n_t \cos\theta_t} \tag{2.1.17}$$

$$t_s = \frac{E_{ts}}{E_{is}} = \frac{2n_i \cos\theta_i}{n_i \cos\theta_i + n_t \cos\theta} \tag{2.1.18}$$

Thin film and multilayer structures involve multiple interfaces, with Fresnel reflection and transmission coefficients applicable at each. It is important to track the relative phase of each light component to determine correctly the overall reflected or transmitted beam. For this purpose, we define the film phase thickness as:

$$\beta = 2\pi \left(\frac{d_1}{\lambda}\right) n_1 \cos\theta_1 \tag{2.1.19}$$

The superposition of multiple light waves introduces interference that depends on the relative phase of each light wave. The Figure 2.1.8 illustrates the combination of light waves in the reflected beam and their corresponding Fresnel calculations.

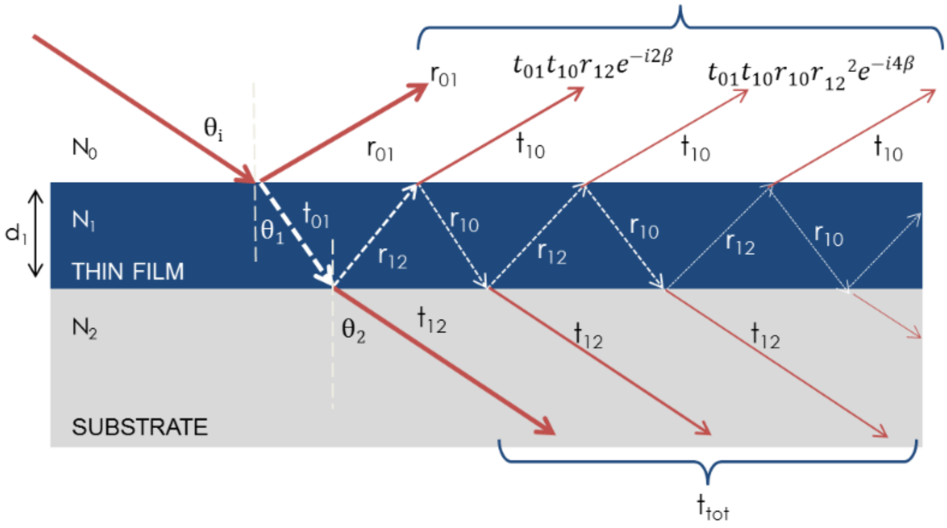

Figure 2.1.8: Light reflects and refracts at each interface, which leads to multiple beams in a thin film.

The data from the ellipsometer are values of Ψ and Δ as a function of wavelength.

$$\rho = \tan(\Psi)e^{i\Delta} \tag{2.1.20}$$

The Fresnel reflection coefficients are introduced as the reflected amount of the E-field in proportion to the incident amount. This is viewed either parallel or perpendicular to the plane of incidence as

$$\rho = \frac{r_p}{r_s} \tag{2.1.21}$$

This correlation is utilized to derive expressions for the refractive index of a material as a function of Ψ and Δ.

$$\tilde{n}_t = \frac{\left[\sqrt{1 - 4\sin^2\theta_i \tan\Psi e^{j\Delta} + 2\tan\Psi e^{j\Delta} + \tan^2\Psi e^{j\Delta}}\right] \tilde{n}_i \sin\theta_i}{\cos\theta_i \left[1 + \tan\Psi e^{j\Delta}\right]} \tag{2.1.22}$$

Here, $\tilde{n}_t$ is the complex refractive index of medium $\tilde{n}_i$ is the complex refractive index of the ambient, θ_i is the angle of incidence and θ_t is the unknown angle of transmission.

Ellipsometry measurements

A sample ellipsometry measurement is shown in Figure 2.1.4. The incident light is linear with both p- and s- components. The reflected light has undergone amplitude and phase changes for both p- and s- polarized light, and ellipsometry measures their changes.
The primary tools for collecting ellipsometry data all include the following: light source, polarization generator, sample, polarization analyzer, and detector. The polarization generator and analyzer are constructed of optical components that manipulate the polar-

ization: polarizers, compensators, and phase modulators. Common ellipsometer configurations include rotating analyzer (RAE), rotating polarizer (RPE), rotating compensator (RCE), and phase modulation (PME).

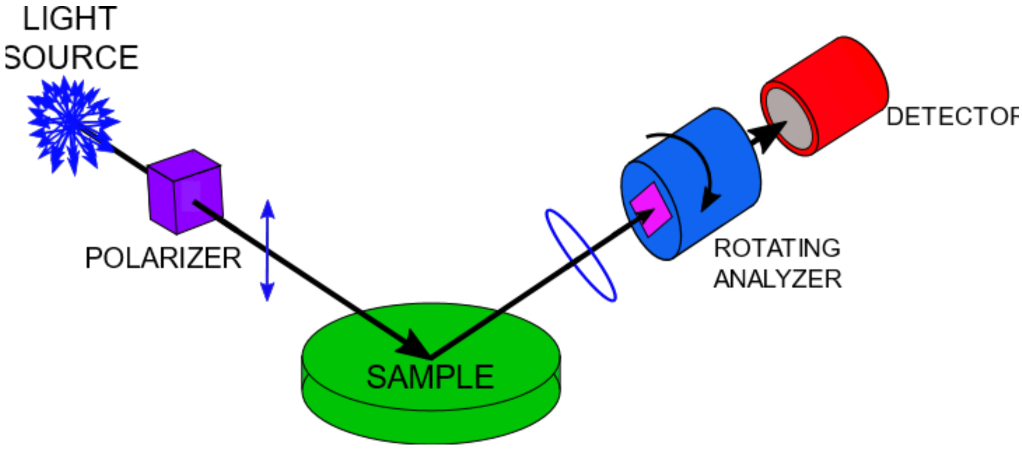

Figure 2.1.9: The RAE configuration

The RAE configuration is shown in the Figure 2.1.9. A light source produces unpolarized light which is then sent through a polarizer. The polarizer allows light of a preferred electric field orientation to pass. The polarizer axis is oriented between the p- and s-planes, such that both arrive at the sample surface. The linearly polarized light reflects from the sample surface, becomes elliptically polarized, and travels through a continuously rotating polarizer (referred to as the analyzer). The amount of light allowed to pass will depend on the polarizer orientation relative to the electric field "ellipse" coming from the sample. The detector converts light to electronic signal to determine the reflected polarization. This information is compared to the known input polarization to determine the polarization change caused by the sample reflection.

Using (2.1.22), these data can be used to calculate the complex index of refraction as a function of wavelength.

2.2 Nonlinear Optics and Techniques

The characterization of nonlinear optical properties of materials is essential for the development of new techniques for the diagnostics [37].

When the light incident on the medium is sufficiently intense, the response of the medium becomes non-linear with the applied electric field. This non-linear response can be written as a series expansion of electrical field powers given by [26]:

$$\vec{P} = \varepsilon_0 \left\{ \chi^{(1)} \cdot \vec{E} + \chi^{(2)} : \vec{E}\vec{E} + \chi^{(3)} \vdots \vec{E}\vec{E}\vec{E} + \dots \right\} \tag{2.2.1}$$

Where $\chi^{(2)}$ is the second order of polarization and is responsible for three wave mixing pro-

cess. The second order originate phenomen as such as second harmonic generation (SHG), sum and difference frequency generation (SFG and DFG), linear electro-optic effect and optical rectification. In materials with inversion symmetry such as gases and liquids this term vanishes. $\chi^{(3)}$ is the third order of the polarization and it is responsible for four wave mixing process for phenomena as such third-harmonic generation (THG), Raman scattering, two-photon absorption (2PA), four-wave mixing (FWM), and the optical Kerr effect and is non-null for materials with any special symmetry.
As mentioned before, in centro-symetric materials:

$$\overrightarrow{P} = \varepsilon_0 \left\{ \chi^{(1)} \cdot \overrightarrow{E} + \chi^{(3)} \vdots \overrightarrow{E}\overrightarrow{E}\overrightarrow{E} \right\} \tag{2.2.2}$$

Only the first- and the third order susceptibilities are considered, the intensity dependent refractive index and the intensity dependent absorption coefficient are given by:

$$n = n_0 + n_2 I \tag{2.2.3}$$

$$\alpha = \alpha_0 + \alpha_2 I \tag{2.2.4}$$

Hence n_2 describes the change in refractive index of a material due to an increasing electric field strength and is directly proportional to the nonlinear polarization response of order 3. Thus we can observe the frequency dependence of a temporally Gaussian pulse as it propagates through a medium of length z. This phase accumulation through propagation through a nonlinear medium is referred to as self-phase modulation (SPM). Thus, for large $\overrightarrow{E}$ field magnitudes, i.e. large irradiance, Δn increases and the total phase accumulation due to propagation in the medium becomes appreciable which causes spectral broadening of the input pulse. See Figure (2.2.1). In the case of SPM, this change in index is a Kerr-type effect and therefore depends on the intensity of the input light.

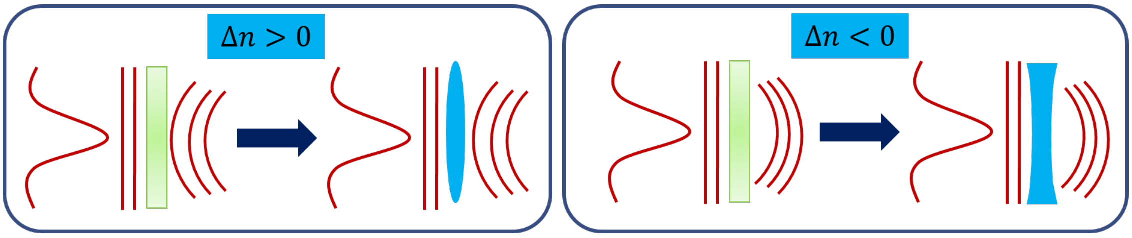

Figure 2.2.1: Representation of the Self-focusing and self-defocusing effects of a Gaussian beam.

Another nonlinear process associated with the interaction of the beam laser with a nonlinear medium it is the nonlinear absorption. NLA is expressed in terms of a change in intensity of the incident laser beam transmitted by the sample. The two NLA processes can be due to TPA or excited state absorption (ESA).

- *Two-photon absorption* is a process where the sample simultaneously absorbs two photons under high intensity illumination without one-photon resonance with intermediate states.
- *Excited State Absorption* (ESA) can be an important process when there are simultaneous one and two-photon resonances with the medium eigenstates. In this case the materials may present saturated absorption for ground state absorption at low intensity and increased absorption due to ESA, when the laser intensity is increased.

2.2.1 Z-scan

The Z-scan technique is the most widely used method to measure the nonlinear index of refraction and the nonlinear absorption of organic materials, optical materials, nanostructured materials, etc. The Z-scan method exploits the wavefront distortion of a focused Gaussian beam, analyzing the transmittance value of the sample measured through a finite aperture in the far field as the sample is moved along the propagation path z. The Z-scan experimental apparatus is shown in Figure (2.2.2).

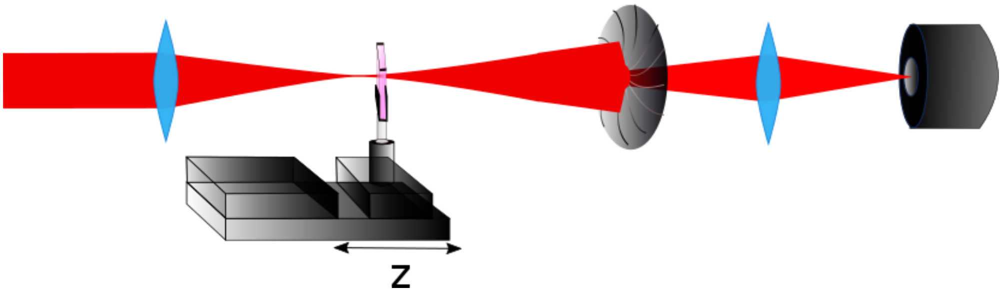

Figure 2.2.2: Basic experimental setup for Z-scan technique.

The physical origin of this technique is related to the self-focusing phenomenon. The latter occurs when a light beam of non-uniform spatial intensity distribution, as Gaussian one, falls on a medium with a nonlinear index of refraction. Since the nonlinear index follows the shape of the beam, an index gradient is induced in the medium. For a positive nonlinearity, this means that a greater index, and hence the larger phase retardation, is induced in the on-axis center than in the wings of the beam. In the case of the negative n_2 we have an inverse situation. The nonlinear focusing has the effect of creating a positive ($n_2 > 0$) or negative ($n_2 < 0$) lens in the medium that tends to focus or defocus slightly the beam.

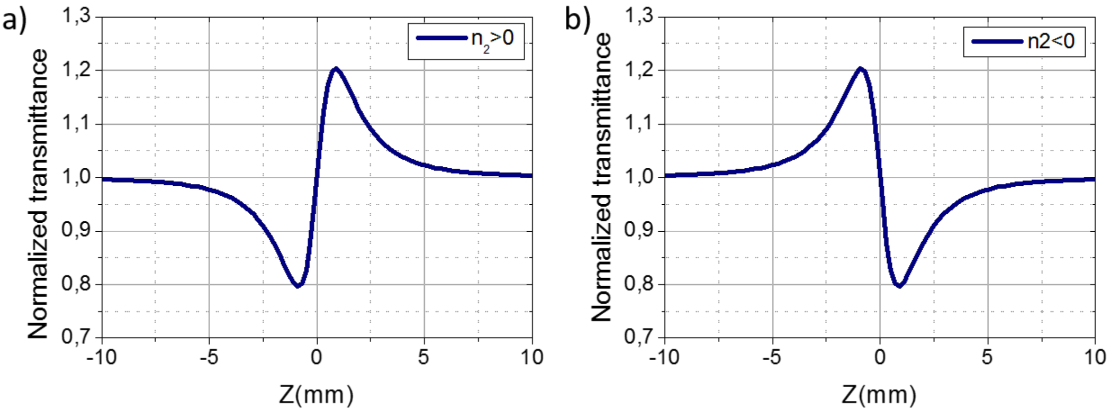

Figure 2.2.3: Typical Closed aperture Z-scan transmittance for a) positive and b) negative third order nonlinear refraction.

The Z-scan trace is characterized by a valley-peak (a minimum followed by a maximum) configuration for a positive nonlinearity (Figure 2.2.3a)) and a peak-valley trace for a negative one (Figure 2.2.3b)). The transmittance is normalized to unity for the sample far from the focus where the incident intensity is low and so the nonlinearity is negligible.

$$T(z) = \frac{\int P(z)}{\int P(z_\infty)} \tag{2.2.5}$$

In the theorical formulation the transverse profile of laser light is often described by TEM_{00} mode of circular Gaussian beam:

$$E(r,t,z) = E_0(t)\frac{w_0}{w_z}\exp\left(-\frac{r^2}{w(z)} - \frac{ikr}{2R(z)}\right)e^{-i\phi(z,t)} \tag{2.2.6}$$

The Gaussian beam symmetry is illustrated in Figure 2.2.4.

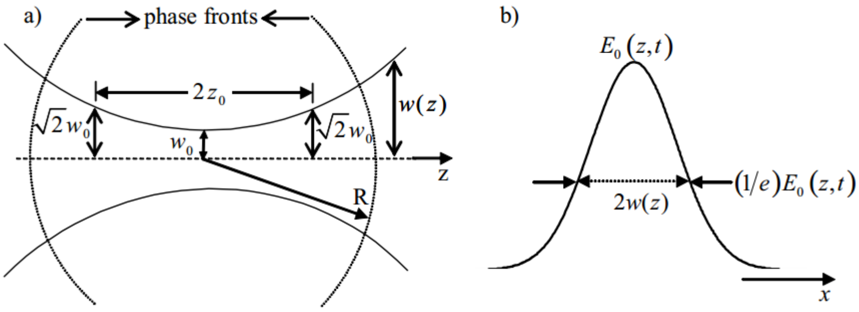

Figure 2.2.4: Schematic illustration of a TEM_{00} Gaussian beam. a) beam propagation profile and b) beam cross section.

The beam cross section is described by radius $w(z)$ which is defined as a the half-width of the Gaussian curve at the point r, where the curve is at $1/e$ of its maximum value. The radius has a minimum, defined by w_0 (so called beam waist), at the plane $z = 0$. Outside this plane the waist changes with z according to:

$$w^2(z) = w_0^2 \left(1 + \frac{z^2}{z_0^2}\right) \tag{2.2.7}$$

where z_0 is a Rayleigh range which corresponds to the distance from $z = 0$ at which the beam radius increases by a factor of $\sqrt{2}$. The Rayleigh range can be also defined as:

$$z_0 = k\frac{w_0^2}{2}. \tag{2.2.8}$$

The radius of the curvature of the Gaussian wavefront is given by

$$R(z) = z\left(1 + \frac{z_0^2}{z^2}\right), \tag{2.2.9}$$

when a beam propagating through a thin sample ($L < z_0$) undergo a change in the phase that in the slowly varying envelope approximation is give by

$$\Delta\Phi_0 = \frac{\Delta\Phi_0^{(3)}}{1 + z^2/z_0^2} \exp\left(-\frac{2r^2}{w^2(z)}\right). \tag{2.2.10}$$

The change in the phase is related with the variation of the nonlinear refractive index by:

$$\Delta\Phi_0^{(3)} = k\Delta n L_{eff} \tag{2.2.11}$$

where L_{eff} is the effective optical path length in the sample.

$$L_{eff} = \frac{1 - e^{-\alpha L}}{\alpha}, \tag{2.2.12}$$

L is the sample thickness and α is the linear absorption coefficient. In the near field region the phase has practically an infinite radius of curvature, and hence the Gaussian beam mimics a plane wave. The model of the Gaussian beam is very useful to treat problems in nonlinear optics. The measured normalized energy transmittance in a closed aperture Z-scan experiment can be fitted numerically in order to find n_2 [26].

$$T(z, \Delta\Phi_0) \simeq 1 + \frac{4(z/z_0)\Delta\Phi_0}{\left[(z/z_0)^2 + 1\right]\left[(z/z_0)^2 + 9\right]}, \tag{2.2.13}$$

in the absence of NLA, the peak-to-valley transmittance variation for $\Delta\Phi_0 < \pi$ is given by:

$$\Delta T_{pv} = 0.406(1 - S)^{0.25} \left|\Delta\Phi_0\right|. \tag{2.2.14}$$

S is the aperture linear in the far field. Typical experimental values used for S range from 0.1 to 0.8.

$$S = 1 - \exp\left(-2r_a^2/w_a^2\right), \tag{2.2.15}$$

where w_a is the beam radius at the aperture in the linear regime.
For the Open aperture signal these can be solved analytically,

$$T(z, q_0) = \sum_{m=0}^{\infty} \frac{(-q_0)^m}{(m+1)^{3/2}\left[1 + (z/z_0)^2\right]} \tag{2.2.16}$$

where,

$$q_0 = \beta_2 I_0 L_{eff} \tag{2.2.17}$$

For $|q_0| < 1$. Typical open aperture normalized transmittance is shown in Figure 2.2.5.

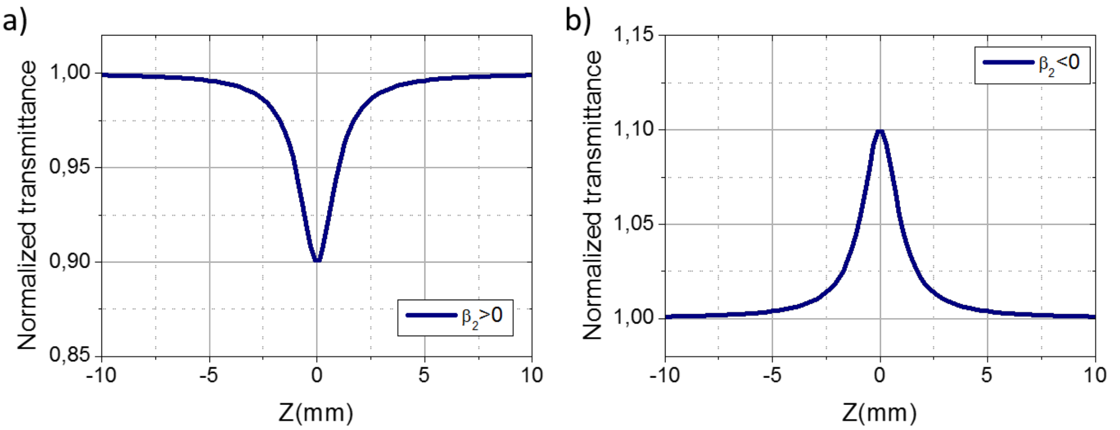

Figure 2.2.5: Typical Open Z-scan transmittance for a) positive and b) negative third order nonlinear absorption.

2.2.2 Dual Arm Z-scan

The experimental apparatus used in our experiments is shown in Figure 2.2.6. This setup consists of a standard Z-Scan setup with an additional arm similar to the Dual arm technique used by Ferdinandus *et. al.* in [28]. We have a Coherent Opera, 800 nm, 120 fs, 1 kHz, laser and Mira, 800nm , 150fs, 76MHz. The polarizer and $\lambda/2$ are used for controlling the power of the laser. The first beam splitter divided the beam laser in 5%. One beam with 95% is directed to the sample arm (arm 1), and the another 5% is directed to the reference arm (arm 2).

Arm 1: The first beam passes through a focusing lens with focal distance of 10cm and then for the sample that which is placed in a motorized system. After that, another beam splitter divide the beam in order to measure the both nonlinear responses. One beam passes through an aperture (iris with S=0.4) and after to photodetector for to collecting the nonlinear refraction contribution. The another beam (non-aperture or S=1) measure the nonlinear absorption. Arm 2: Have the same path that the arm 1, but no have a sample in the motorized system.

This configuration is used for the purpose of reducing the influence of the fluctuations of the laser in the measurement. The two arms have been carefully aligned so that both arms have the same response, the equipment in each arm is also matched using the same optics and model of photodetectors. The beam polarization could be adjusted in order to orient it properly with respect to the SPR mode of the sample.

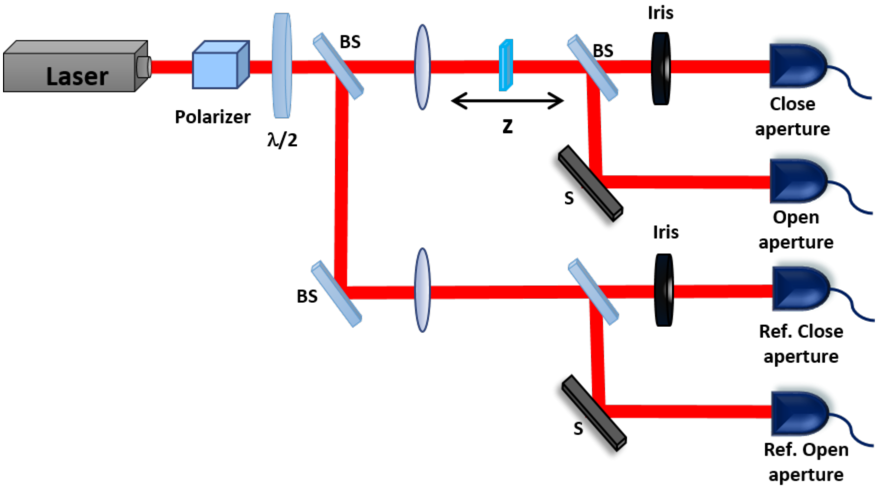

Figure 2.2.6: Dual arm Z-scan.

The system was calibrated using CS_2, which is a kind of standard material whose NLO properties are well known and characterized [26, 38, 29].
From the data with CS_2, and an aperture corresponding to $S = 0.4$ in the Z-scan setup, a beam waist of $21\mu m$ at the focus was inferred, which was then used to calculate the intensities. The characteristics curves of CS_2 are in the Figure 2.2.7 for excitation beam at $800nm$, $20Hz$ and $120fs$. We observed a positive NLR and did not observe NLA for the range of intensities employed $(10-40)GW/cm^2$. The value of $n_2 = 2.2 \times 10^{-15} cm^2/W$ was taken of the literature [38] for to find the parameters characteristics of the system.

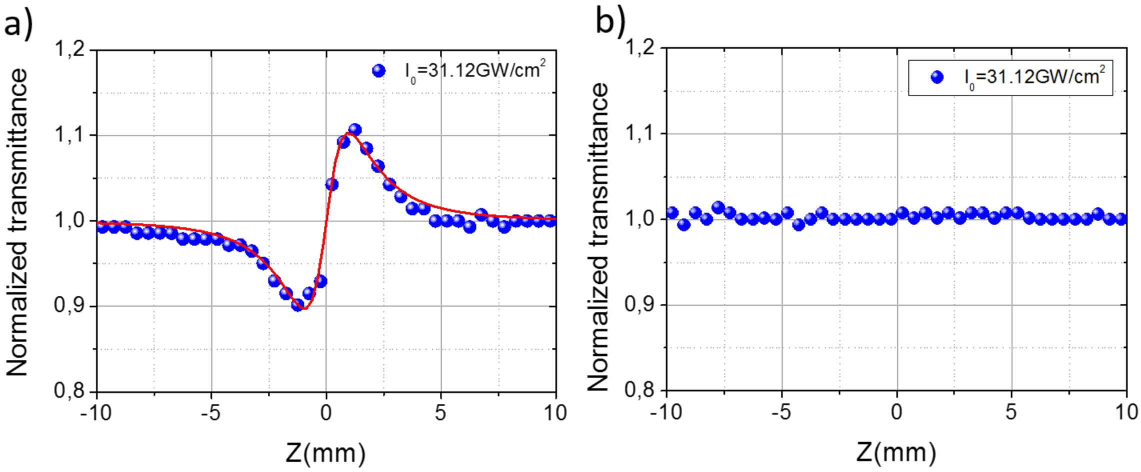

Figure 2.2.7: Z-scan signature for CS_2 at $20Hz$. a) Closed aperture and b) Open aperture Z-scan.

For the configuration with excitation beam at $800nm$, $120fs$, and $1kHz$, the curves for

CS_2 was shown in Figure 2.2.8. We observed again the best alignment of the system and the positive signal for NLR and no signal for NLA. Was used the same value of the n_2 mentioned above and was find the same values for the parameters.

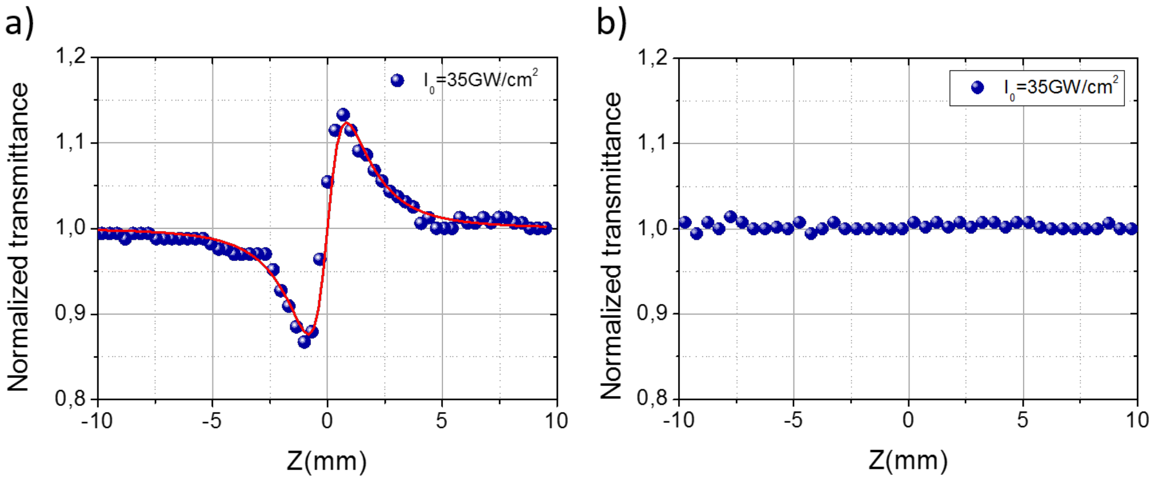

Figure 2.2.8: Z-scan signature for CS_2 at $1kHz$. a) Closed aperture and b) Open aperture Z-scan.

Thermal lensing induced by high repetition rate lasers in Z-scan experiments has been reported by various authors [38, 29, 26, 39]. The light passing through the sample is partially absorbed and converted in heat.

For the excitation beam at $800nm$, $76MHz$ and $150fs$, cumulative thermal effects is present due to the high repetition rate of the laser and it is reflected in the change of the signal of the NLR. In the Figure 2.2.9 we observed the negative NLR and not signal for NLA. The value for $n_2 = -4.4 \times 10^{-15} GW/cm^2$ was take of the references [30, 38] for to obtain the parameters of the system.

The red solid curve in all figures representing the fit with the equation (2.2.13). This thermal effect can be overcome using a low ($<$1kHz) repetition rate laser.

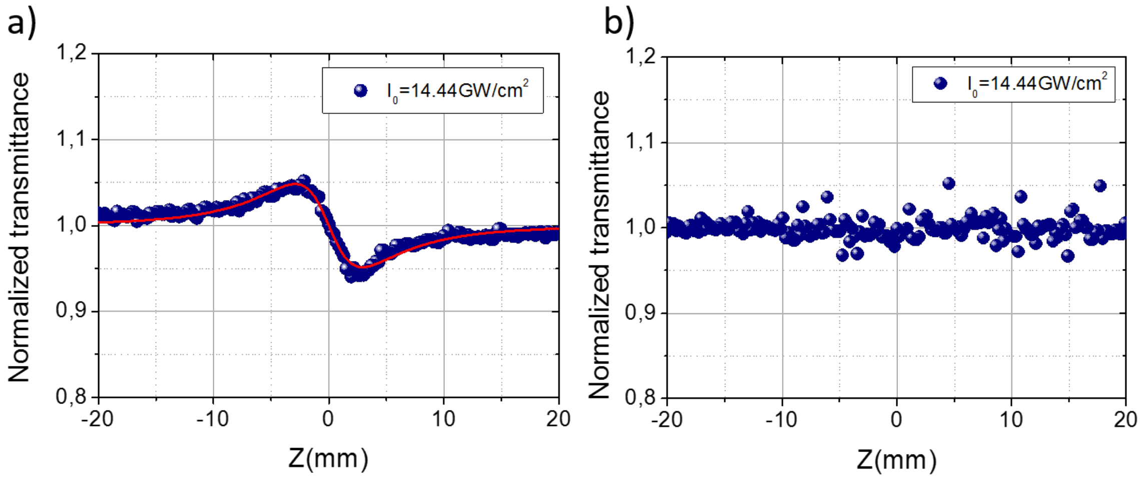

Figure 2.2.9: Z-scan signature for CS_2 at $76MHz$. a) Closed aperture and b) Open aperture Z-scan.

2.2.3 Beam collimated technique using a HSWFS

The idea of using this technique is to exploit the ability of the Hartmann-Shack wavefront sensor (HSWFS) to measure wavefront distortions. The sensor consists of a CCD camera, an arrangement of microlenses and a software capable of reconstructing the entire wavefront using the Zernike polynomials. Within these coefficients is the defocusing coefficient (C5) which we relate to the part of the non-linear optics. As a nonlinear material exhibiting variation of the index of refraction behaves as an induced lens, i.e. the material induces a focusing or defocusing of the beam passing through the sample. The idea then is to pass a collimated beam through the sample and see the induce lens effect through the wavefront sensor and with the value of the coefficient C5 to be able to correctly quantify the value of the nonlinear refractive index. The advantage of this method is that it is easy to implement, the alignment is done directly with the wavefront sensor which facilitates assembly and does not require the construction of an interface for data acquisition because of the sensor software shows on the screen the value of all coefficients. Another advantage of this method is that the sample is fixed which helps us in our objective of applying an electric field to a liquid sample.

Wavefront

The wavefront is called the locus of space in which the points of the medium are reached at the same instant by a given wave. Given a wave propagating in space (or on a surface), wavefronts can be visualized as surfaces (or lines) that move over time away from the source. The wavefront is made up of points that share the same phase. Therefore, at a given instant t, a wavefront is formed by the locus (surface or line) of all points whose coordinates satisfy the relation:

$$\mathbf{k}\cdot\mathbf{r}-\omega t = cte \tag{2.2.18}$$

Where $\mathbf{k}$ is the propagation vector ($|\mathbf{k}| = 2\pi/\lambda$, λ is the wavelength), $\mathbf{r}$ is the position vector of the point where the phase is calculated, ω Is the angular frequency of the wave and t is the time. This relationship arises from the solution of the wave equation.

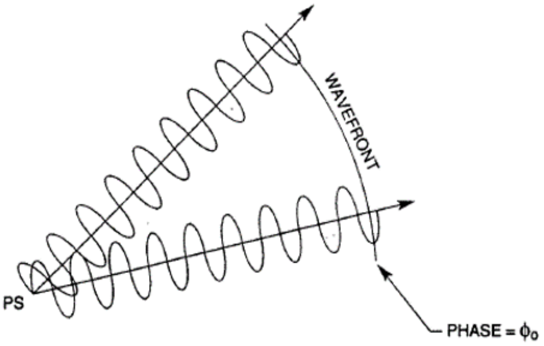

Figure 2.2.10: Pictorial view of a wavefront [40].

The phase of the wave can be affected by the medium in which it propagates. For this, the OPL (optical path length) is defined as the geometric path (C) that travels the wave affected by the refractive index n of the medium:

$$OPL = \int_C n(l)dl \tag{2.2.19}$$

Similarly, the optical path difference (OPD) can be defined as $OPD = OPL_1 - OPL_2$. For a surface wavefront propagating in the z direction, the optical path difference between an arbitrary wavefront point, which we take as a reference, and the rest of the points will be a function of (x, y) which will be denoted $W(x, y)$. This function will be called the 'aberration' of the wavefront. An alternative way of defining the OPD is to use the difference between an aberrated wavefront φ (the actual wavefront that is obtained) and the ideal wavefront φ_0 (the wavefront to be obtained) [40].

The function $W(x, y)$ can be represented mathematically by a polynomial. The two most commonly used polynomial basis in the description of aberrations in optical systems are the Seidel base and the Zernike base. The Seidel base is more used in the design process and Zernike base in the characterization of optical systems and in metrological applications.

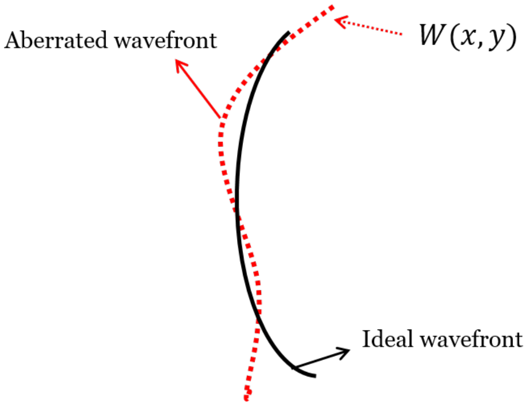

Figure 2.2.11: The diagram establishes the relationship between the aberrated wavefront and the ideal wavefront [40].

Hartmann-Shack wavefront

The HSWFS comprise a CCD camera and a microlens array that is mounted at a defined distance in front of the camera sensor chip. Each microlens generates a spot on the sensor surface. The spot centroid position depends on the wavefront gradient in front of the lens area.

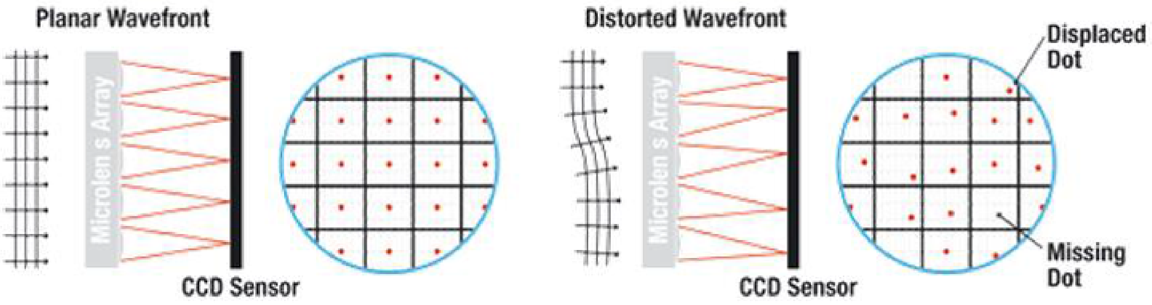

Figure 2.2.12: Each microlens of the lenslet array collects the light incident to its aperture and generates a single spot on the detector plane (CCD camera) that is located at a distance of one focal length behind the lenslets. a) Planar wavefront. b) Distorted wavefront [41, 42].

Each spot is centered behind the lens that generated it only if the incident wavefront is planar and parallel to the plane of the lenslets (Figure 2.2.12a)). These are the Reference Spot Positions, also known as Reference Spotfield. Depending on the distortion of the wavefront incident on the sensor, the current spot positions will be shifted in the X and Y directions away from the optical axis Z of its associated microlens (see Figure 2.2.12b)). The displacement is described by the angle α.

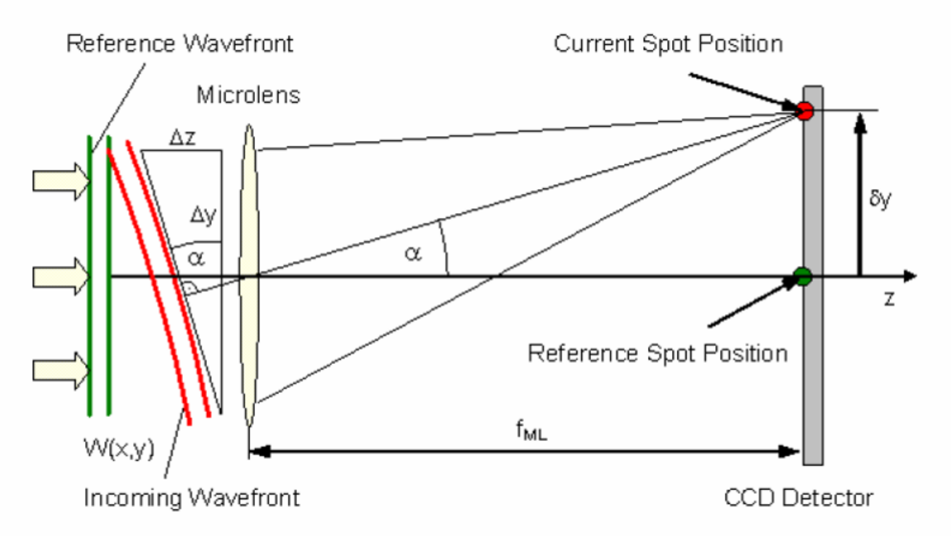

Figure 2.2.13: Schematic representation of the deviation of the spot caused by the distortion in the incident wavefront [41, 42].

From the above sketch (Figure 2.2.13) it can be seen that this deviation is caused by the deviation of the wavefront incident on the microlens from the reference wavefront, or in geometrical terms:

$$\tan\alpha = \frac{\Delta z}{\Delta y} = \frac{\delta y}{f_{ML}} \tag{2.2.20}$$

If $W(x,y)$ describes the shape of the wavefront, then its partial derivatives relative to x and y are determined by the spot shift dx and dy respectively, as well as by the distance between microlens and detector, which usually is equal to the focal length of the microlens f_{ML}:

$$\tfrac{\partial}{\partial x}W(x,y) = \tfrac{\delta x}{f_{ML}} \quad \tfrac{\partial}{\partial y}W(x,y) = \tfrac{\delta y}{f_{ML}} \tag{2.2.21}$$

Spot deviations δx and δy are determined by calculating the centroid coordinates of all detectable spots and subsequently subtracting the corresponding reference coordinates. The wavefront shape function $W(x,y)$ is the result of a 2-dimensional integration process of these spot deviations.

Zernike polynomials are often used for this purpose since they are made up of terms that are of the same form as the types of aberrations often observed in optical tests (Zernike, 1934).

The wave aberration function of such systems can be expanded in a power series or a complete set of orthogonal polynomials. The derivation below follows reference [41, 43, 42]:

$$W(\rho,\theta) = \sum_{n=0}^{\infty}\sum_{m=0}^{n} c_{nm} Z_n^m(\rho,\theta) \tag{2.2.22}$$

Where c_{nm} are the expansion coefficients that depend on the location of the point object, n and m are positive integers including zero, $n - m \geq 0$ and even, and

$$Z_n^m(\rho, \theta) = [2(n+1)/(1+\delta_{m0})]^{1/2} R_n^m(\rho)\cos(m\theta) \tag{2.2.23}$$

Is an orthonormal Zernike polynomial, the radial polynomials can be derived as a special case of Jacobi polynomials

$$R_n^m(\rho) = \sum_{s=0}^{(n-m)/2} \frac{(-1)^s (n-s)!}{s!(\frac{n+m}{2}-s)!(\frac{n-m}{2}-s)!}\rho^{n-2s}. \tag{2.2.24}$$

Their orthogonality and normalization properties are given by

$$\int_0^1 R_n^m(\rho) R_{n'}^m(\rho)\rho d\rho = \frac{1}{2(n+1)}\delta_{nn'} \tag{2.2.25}$$

$$\int_0^{2\pi} \cos(m\theta)\cos(m'\theta) d\theta = \pi(1+\delta_{m0})\delta_{mm'}. \tag{2.2.26}$$

The Zernike expansion coefficients are given by

$$c_{nm} = \frac{1}{\pi}\int_0^1 \int_0^{2\pi} W(\rho, \theta) Z_n^m(\rho, \theta)\rho d\rho d\theta \tag{2.2.27}$$

In Table (2.1) contain the 6 first Zernike polynomials. The Figure (2.2.14) show the two- and three- dimensional plots of the 6 first Zernike polynomials. Each term contains the appropriate amount of each lower order term of the Zernike minimizes the rms wavefront error to the order of that term. Adding other aberrations of lower order can only increases the rms error. Furthermore, the average value of each term over the unit circle is zero.

Order	Mode	Frequency	Polynomial	Name
1	0	0	1	Piston
2	1	-1	$\rho\sin(\theta)$	Tilt y
3	1	1	$\rho\cos(\theta)$	Tilt x
4	2	-2	$\rho^2\sin(2\theta)$	Astigmatism ±45
5	2	0	$2\rho^2 - 1$	**Defocus**
6	2	2	$\rho^2\cos(2\theta)$	Astigmatism 0º/90º

Table 2.1: Zernike index scheme [43].

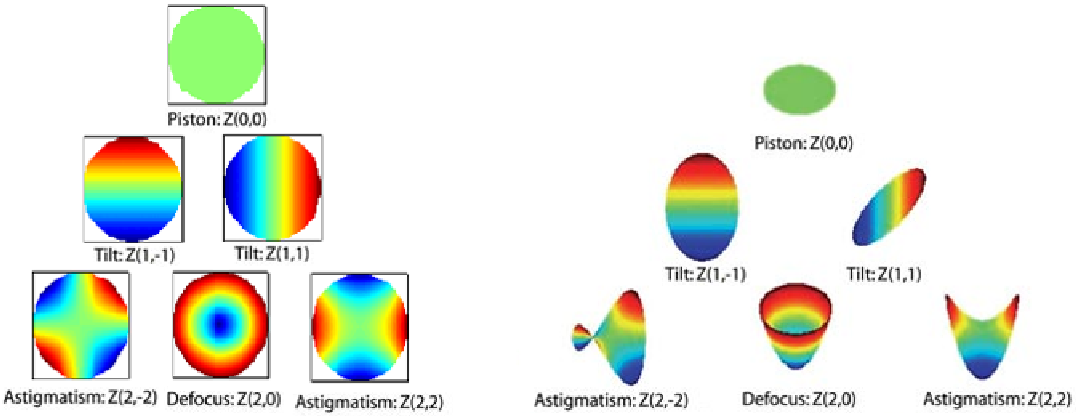

Figure 2.2.14: Zernike polynomials in 2D and 3D. The Z_0^2 is the defocus [43].

Beam collimated technique with Hartmann-Shack

As shown schematically in Figure (2.2.15), the setup is very simple, we have a polarizer and a half-wave plate ($\lambda/2$) for controling the laser intensity. The beam diameter was collimated and reduced to $\sim 1.1mm$ using a keplerian telescope (T1) such that the beam Rayleigh length remained much larger than the sample thickness. At the exit of the sample the laser beam was magnified with a second telescope (T2) to obtain a beam waist about $3mm$ and imaged on a HS wavefront analyzer. The use of the second telescope is necessary to obtain a better approximation of the values of the wavefront since the more light reaches the detector, the more accurate the reconstruction of the wavefront. The wavefront data was acquired using a software provided by Thorlabs (the company where the device was purchased from).

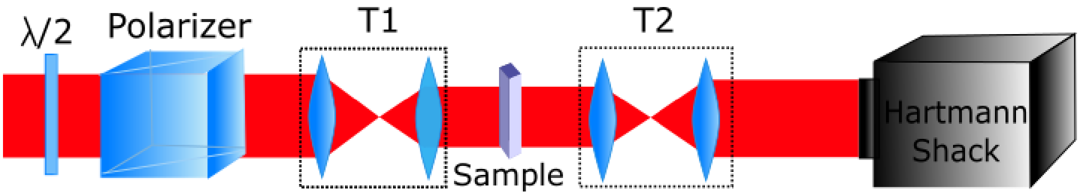

Figure 2.2.15: Beam collimated technique using a Hartmann-Shack device.

A wavefront reference was taken using lower intensities with the sample placed in the collimated beam. In that case the measured wavefront changes are based on this reference to allow accurate measurements of further wavefront distortions induced by higher intensities. We have used the initial 6 Zernike modes indicated in Table (2.1) to fit the measured wavefront within the pupil area (the piston term, not measurable with the HS sensor has been excluded). Figure 3 shows the Zernike coefficients used to describe the wavefront aberrations. While Zernike coefficients corresponding to tilt and astigmatism (C2, C3, C4, C6) remain approximately constant there is a dependence of the defocus coefficient C5 with the laser intensity. In accordance with the Zernike orthogonality properties [14], the defocus Zernike is thus enough to describe the wavefront distortions caused by nonlinear effects.

$$W_{TOTAL} = W(z=0) + W_L(z=L) + W_{NL}(z=L) \tag{2.2.28}$$

Where, $W(z=0)$ contains the wavefront profile with the wavefront aberrations of setup experimental.

$W_L(z=0)$ contains the aberrations induced by linear refraction and imperfections of the sample.

$W_{NL}(z=L)$ contains the accumulated nonlinear phase change in the sample.

In analogy with Z-scan technique, we can affirm that the n_2 is proportional to the n_2 calculated with Z-scan technique with the calibration factor f.

$$n_2 = f\frac{\lambda}{2\pi I(r,t)L_{eff}}C_5 \tag{2.2.29}$$

C_5 can be measured in waves or radians.

Calibration factor

The general calibration method was as follows. First, one needs to determine f for the used setup. In order to do this, we got a 2mm thick quartz cuvette containing CS_2 and measured C_5 as a function of the laser intensity (by controlling its pulse energy). The results for $76MHz$ and $1kHz$ repetition rates can be seen in Figure 2.2.16.

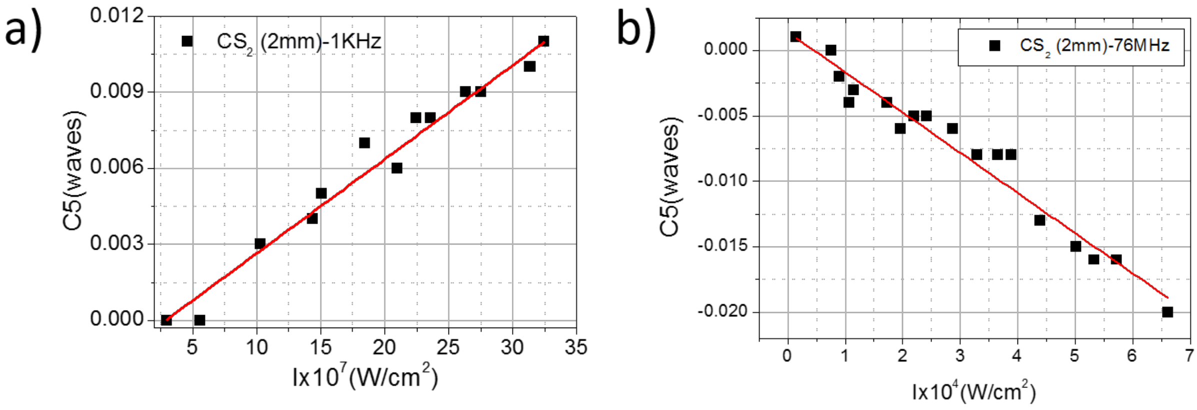

Figure 2.2.16: Calibration system using CS_2 leading to the determination of f by measuring the slope of the fitted straight line for laser: a) 1kHz and b) 76MHz.

By knowing the slope of the fitted straight line and using the well known value of n_2 for the CS_2 under such excitation conditions, $n_{2,CS_2}^{76MHz} = -4.4\times10^{-15}cm^2/W$ [38, 30], one finds $f = 2.1\times10^{-3}$ and the system is now calibrated. Similar procedure has been performed for the excitation at 1 kHz, and for such low repetition rates one knows for

$n_{2,CS_2}^{1kHz} = 2.1 \times 10^{-15} cm^2/W$ [38] we find that $f \sim 1$. The slope of the curve gives directly the sign of the nonlinearity.

3 Gold nanorod clusters supported in PVA

3.1 Introduction

This chapter describes the results of the linear and nonlinear optical characterization of gold nanorods supported in PVA published in the reference [15]. The samples employed in this chapter were synthesized and partially characterized (linear characterization) by Dr Richard Vaia and his team at the Materials and Manufacturing Directorate, Air Force Research Laboratory, Ohio, USA. The theoretical calculation for the electric field enhancement was performed by Prof. Paras Prasad and his work team at the Buffalo University, Buffalo, NY, USA.

In the search of new nanostructured materials for photonic applications, metals such as gold, silver, and platinum have been studied in order to exploit the plasmonic enhancement in the local field at the metal-dielectric interface [3, 2, 1]. Among those, gold nanorods (GNRs) have been studied, and different applications have arisen, from biophotonics to laser Q-switching [44, 45, 46, 47]. Special interest in this particular material stands from the anisotropic behavior of the localized surface plasmon resonance (LSPR) leading to a transverse (T-LSPR) and a longitudinal (L-LSPR) resonant behavior. In nonlinear optics (NLO), it has been demonstrated that L-LSPR plays a major role as compared to the T-LSPR, which is due to the larger field enhancement arising from the free-electrons oscillating along the longitudinal axis.

From the experimental point of view, GNR has been studied in solutions or thin film environment. For the fundamental studies, certainly the environment influence can easily be taken into account, and in fact, several important conclusions have been drawn on the role of the surface plasmon resonance in GNR, with the longitudinal and transverse SPR modes arising due to the anisotropic shape of the GNR. From the technological point of view, if the nanorods can be in a "solid state" environment, it can be more convenient for several applications. Furthermore, in general, the GNR are prepared in such a way that they are spatially random in their supporting media. Alignment of the GNR can be very interesting, and in colloidal suspension electric field can be applied for that. However, once again, for certain application, this is not very useful, since the required field is typically of the order of 10kV or more. Therefore, using some stretching technique, a proper alignment of the GNR in a thin film can be performed, as demonstrated in this work as well as in refs [48, 49]. PVA has been a preferred supporting polymeric film due to its well-known properties.

3.2 Fabrication of GNR Cluster-PVA and morphological characterization

Fabrication of GNR-PVA nanocomposite[1]: The concentrated GNR ($L/d \sim 2.1$, length: $L = 51.6 \pm 4.6nm$, and width: $d = 24.3 \pm 1.3nm$) in aqueous solution ($\sim 20nM$) were prepared by modified seed mediated method [50] and subsequential purification procedure (centrifugation at 14000 rpm for 10 min) - TEM image of GNRs is shown in Figure 3.2.1a). GNR cluster-PVA nanocomposites were fabricated employing depletion induced cluster formation technique. Briefly, 10 wt. % PVA aqueous solution was prepared by dissolving PVA (Mw: 89 k, 98-99 % Hydrolyzed, Aldrich) with 1 wt. % of ethylene glycol. Ethylene glycol was added to lower the glass transition of polymer film to facilitate the stretching process. The mixed solution was stirred for 12 hours at 50 °C. 100 µl of concentrated GNR solution was added to 2 g of polymer solution and stirred for 1 hour at room temperature. GNR clusters were formed in solution due to depletion interaction induced by the high molecular weight (89k) and high concentration of PVA. Figure 3.2.1b shows the UV-Vis absorption of GNRs in water and 10 wt. % PVA aqueous solution. In water, GNR are individually dispersed showing L-LSPR at $640nm$. In 10 wt. % PVA solution, due to depletion induced aggregation, the L-LSPR peak becomes broadened and both blue and red shifts were observed due to the formation of clusters which contain both side by side and end to end interaction among rods. T-LSPR peak was also broadened and red shifted. Note that the aggregation is reversible. By lowering the PVA concentration, the original L-LSPR is recovered, confirming the entropically-derived depletion interactions. Films were formed by casting 2g of GNR cluster-PVA solution on 2” × 2” glass substrate. The film was dried naturally for $24h$ at room temperature.

The polymer film was carefully peeled from the substrate. The film thickness was approximately $100\mu m$. The final concentration of GNRs in the film is about 0.2 wt. % ($10nM$). The uniaxial alignment was obtained by stretching the film in the oven at $80°C$ with a draw ratio of 4 which is typical stretching ratio employed to align the GNRs inside the stretched films [9]. Note that the film containing individually dispersed GNRs at the same concentration was prepared in parallel by lowering the PVA concentration to 5%.

---

[1] The samples were fabricated by Rich Vaia and his work team at the Air Force Research Laboratory.

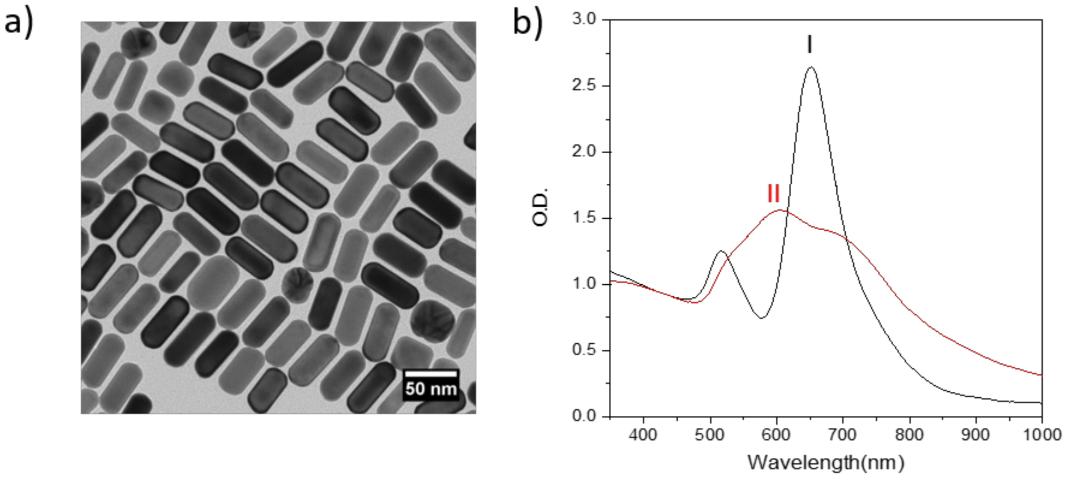

Figure 3.2.1: a) TEM image of GNRs used to fabricate the PVA nanocomposite. Measured dimensions of 51.6 nm(length) x 24.3 nm(width). b) UV-Vis absorption spectra of GNRs dispersed in water (I) and PVA solution (II). [15].

3.3 Linear Optical Characterization

Figure 3.3.1a) schematically shows the stretching process. Figure 3.3.1b) shows the absorption spectra before and after stretching the film. Individually dispersed GNR-PVA nanocomposite was prepared and the UV-Vis absorption showed distinct L-LSPR and T-LSRP peaks which is similar to the GNR dispersed in water (shown as dashed line in Figure 3.3.1 b)). The UV-Vis absorption of GNR cluster-PVA film is not identical to the clusters in PVA solution mainly due to additional aggregation during the drying process. The overall optical density of GNR in the stretched film is smaller than in the unstretched film due to the decreased thickness of the film following stretching. The thickness of the stretched film was $\backsim 50\mu m$ which is consistent with the anticipated thickness considering Poisson ratio of PVA. When the incident light is polarized parallel and perpendicular to the stretch direction, a stretched GNR cluster-PVA film shows distinct absorption spectra (Figure 3.3.1c)).

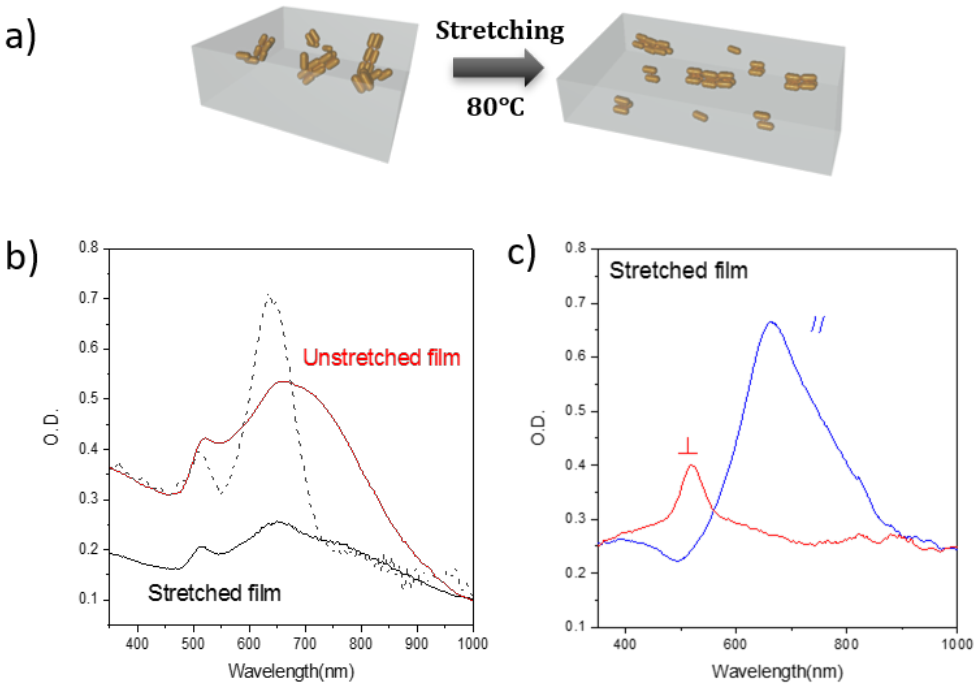

Figure 3.3.1: a) Schematic diagram of the film stretching process. b) UV-Vis absorption spectra of GNR cluster-PVA film before and after stretching. Dashed line shows UV-Vis absorption spectra of individually dispersed GNR in PVA film. c) UV-Vis absorption spectra of the stretched GNR cluster-PVA film upon excitation with the optical field polarized parallel and perpendicular to the stretching direction [15].

When the incident light is polarized parallel to the stretching direction, it only excites the L-LSPR while perpendicularly polarized light only excites the T-LSPR. The unstretched film shows the same absorption spectra irrespective of the light polarization directions. Accordingly, the unstretched film shows the same color in both polarization directions while the stretched film shows distinct color depending on the polarization of the light (Figure 3.3.2).

Figure 3.3.2: Optical microscopy images of the unstretched and stretched GNR cluster-PVA film under white light illumination with polarization (‖) and perpendicular (⊥) to the stretch direction [15].

The structure of clusters was determined via SAXS/TEM analysis. TEM analysis confirms that GNRs in the polymer composite were present as a form of clusters (Figure 3.3.3a) and 3.3.3b)). The average number of rods in an aggregate was 6 (size of the clusters is $101nm \times 54nm$). Therefore, the concentration of clusters can be approximated as 1.7 nM.

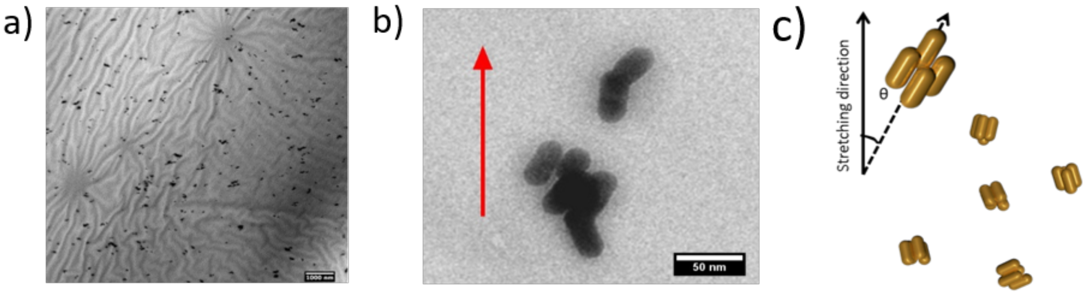

Figure 3.3.3: a) and b) TEM images of GNR clusters in PVA film. The scale bar is 1000 nm in a) and 50 nm in b). The red arrow indicates stretching direction. c) Schematic to measure the angle θ to calculate Herman's orientation function [15].

The alignment of the aggregates in the stretched film was estimated from SAXS by calculating Hermans' orientation function. For the unstretched film, $f \sim 0$, consistent with random orientation of the GNRs. In contrast, for the stretched film, $f \sim 0.4 - 0.47$, which indicates relatively aligned GNRs along the stretching direction. The orientation function estimated from TEM images is consistent with the SAX measurements. Note that the Hermans' orientation function of affine uniaxial elongation of non-interacting, individual rods is theoretically predicted to be $f \sim 0.8$ for a draw ratio of ~ 4.27 The lower degree of alignment is likely due to rotational drag associated with the viscoelastic nature of the polymer matrix, and has been reported previously [36]. Figure 3.3.4a)-b) shows the concentration of clusters aligned at different angles with respect to the uniaxial elongation direction, as derived from the azimuthal SAX intensity ($f = 0.47$ (blue)) and the average cluster concentration (1.7 nM). For an ensemble of non-interacting rods, this orientation distribution function is [51]

$$W = \frac{\lambda^3}{4\pi(\cos^2\theta + \lambda^3 \sin^2\theta)^{3/2}}, \tag{3.3.1}$$

where W is the orientational probability density function, λ is the drawing ratio, and θ is the orientation angle. The experimental distribution is well described by theoretical prediction for $\lambda = 1.7$, consistent with the smaller Hermans' orientation function discussed above. Nevertheless the shape of the distribution is well described by affine rotation of an initially random distribution of isolated rods even though the matrix retards alignment (Figure 3.3.4c)).

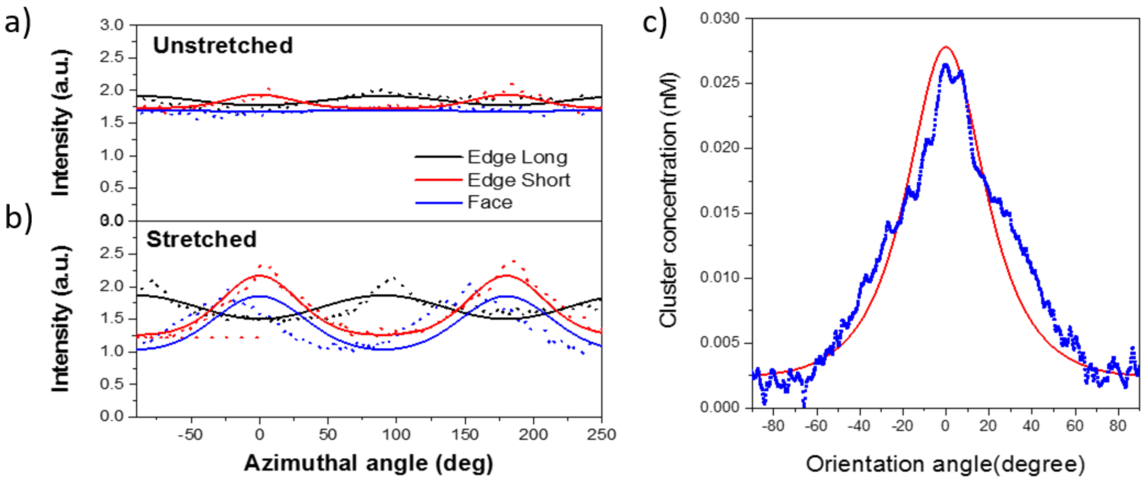

Figure 3.3.4: SAXS azimuthal profiles of (a) unstretched and (b) stretched GNRs in PVA film along the edge-on and face-on directions. c) Theoretically predicted cluster concentration at different orientation angle (red) compared with the experimental value obtained from SAXS analysis (blue) [15].

Characterization: UV-Vis-NIR spectra were acquired with a Cary 5000 UV-Vis-NIR spectrophotometer for the solution and Craic 1000 microspectrophotometer for the film. Mean size of GNR clusters and the orientation parameters were evaluated by TEM (Philips CM200 LaB6 at 200kV and FEI Talos at 200 kV). Nanocomposite films with $100nm$ thickness for electron microscopy (TEM) imaging were prepared by cryomicrotomed at $-80^{o}C$ using a RMC PowerTome XL ultramicrotome and a diamond knife.

3.4 Nonlinear Optical characterization

As pointed out before, NLO characterization of GNR in thin films and colloidal environment has been performed. Optical sources characteristics for the reported NLO studies range from fs to ns pulse duration, $300nm$ to $1550nm$, and most of the work employed the Z-scan technique, as summarized by Olesiak-Banska and co-workers [52].

In this work, we employed a Ti-sapphire regenerative amplifier operating at 800 nm, with repetition rate $20Hz$, and $100fs$ pulse duration. The low repetition was used in order not to damage the thin film sample.

The system was calibrated using CS_2 (See 2.2.7). The beam polarization could be adjusted in order to orient it properly with respect to the longitudinal or transverse SPR mode.

3.4.1 Nonlinear absorption

Using the open aperture (OA) Z-scan setup, one can infer the NLA properties of the sample (See Figure 3.4.1a) to 3.4.1c)). From the Z-scan measure, it is inferred that saturated absorption is taking place, as already observed in the Figure 3.4.1a),b) and ref [48].

The measured open-aperture Z-scan transmission curves are presented in Figures 3.4.1a)-c). As expected, the original GNRs/PVA film showed similar transmission responses upon the excitation with two different polarizations Figure 3.4.1a). The transmission peaks appearing at $z = 0$ were caused by the absorption saturation of the GNRs because of the high laser intensity near the focus. For a stretched film, on the other hand, there was a big difference in the Z-scan curves. In the case of parallel polarized excitation, the NLA effects were very obvious (Figure 3.4.1b)) while for the perpendicular-polarized excitation the NLA effects were not observed Figure 3.4.1c). The polarization independent and dependent transmission curves in Figure 3.4.1a)-c) clearly illustrate the anisotropic nonlinear effects induced by the alignment of GNRs. To quantify the absorptive nonlinearity of our samples, the experimental data were normalized and fitted by using the OA-Z-scan equation (2.2.16).

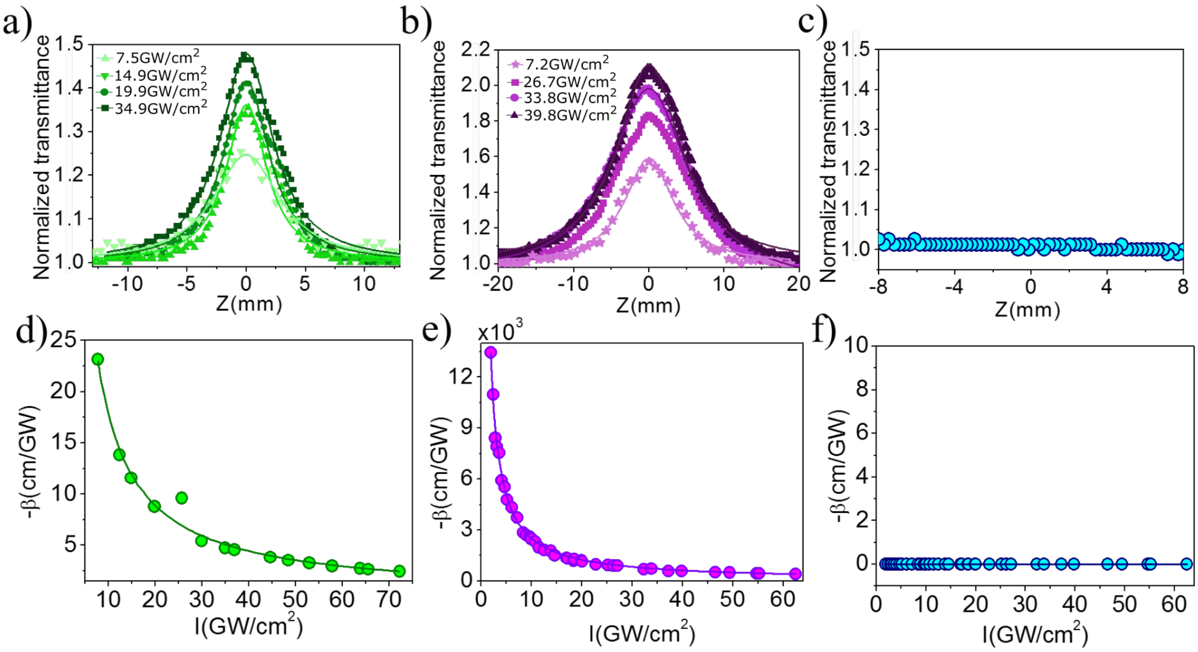

Figure 3.4.1: Traces of open aperture Z-scan for: a) Unstretched b) Stretched with polarization parallel to LSPR c)Stretched with polarization parallel to TSPR. Intensity behavior of the β_2 for: d) Unstretched and e) Stretched samples with polarization parallel to LSPR; and f) Stretched sample with polarization perpendicular to the stretching direction.

To ensure the accuracy in comparisons between different samples, we performed a series of intensity-dependent Z-scan measurements. The results are shown in Figure 3.4.1d) and 3.4.1e), for the unstretched and stretched samples, with the later taking into account the incident polarization with respect to the stretching direction. We employed the same analysis to determine the absorption coefficient as in ref [48], the data was fitted as well with:

$$\beta_2 = \frac{\beta_0}{1 + I_0/I_{SAT}}. \tag{3.4.1}$$

where I_{SAT} is the saturation intensity of the NLA and β_0 is the NLA coefficient under low-intensities excitation, i.e., an intensity I_0 much lower than the saturation intensity I_{SAT}, so that the inequality $I_0/I_{SAT} << 1$ holds. In fact, the nonlinear saturation effect arises from a quasi-resonant one-photon induced nonlinear absorption (see linear absorption spectra in Figure 3.4.3), whose Z-scan signature is shown in Figure 3.4.1, and is quite different from NLA due to two-photon absorption. We keep the notation I_{SAT} bearing in mind the above definition.

The numerical values for β_0 and I_{SAT} are given in table 3.1. It should be observed that for the excitation polarization perpendicular to the LSPR mode, the nonlinear absorption is negligible (Figure 3.4.1f)). The NLA enhancement between the LSPR mode in the stretched sample is 57 times higher than that in the unstretched one, due to the very strong anisotropy. This related mainly to the plasmonic effect arising from the clustering of the GNR, as will be discussed later.

Sample	$\boldsymbol{\beta_0 \times 10^3}$**(cm/GW)**	$\mathbf{I_{sat}}$**(GW/cm^2)**
Unstretched	-1.815	0.256
Stretched Longitudinal	-102.800	0.026
Stretched Transversal	~ 0	$---$

Table 3.1: Measured values of nonlinear absorption coefficient and saturation intensity of the GNR cluster-PVA films for an irradiation wavelength of 800 nm.

3.4.2 Nonlinear Refraction

To obtain the NLR coefficients, a closed aperture (CA) Z-scan was used. By measuring the nonlinear transmission we verified that the NLR coefficient n_2 is positive for the unstretched sample (Figure 3.4.2a)) and for stretched sample when the polarization was parallel to the LSPR (Figure 3.4.2b)), therefore leading to self-focusing in both cases. For the stretched sample with the pump polarization parallel to the TSRP, the sign of the refractive nonlinearity was inverted (Figure 3.4.2c)). The induced nonlinear phase shift was less than π, as required by the theoretically analysis in all cases.

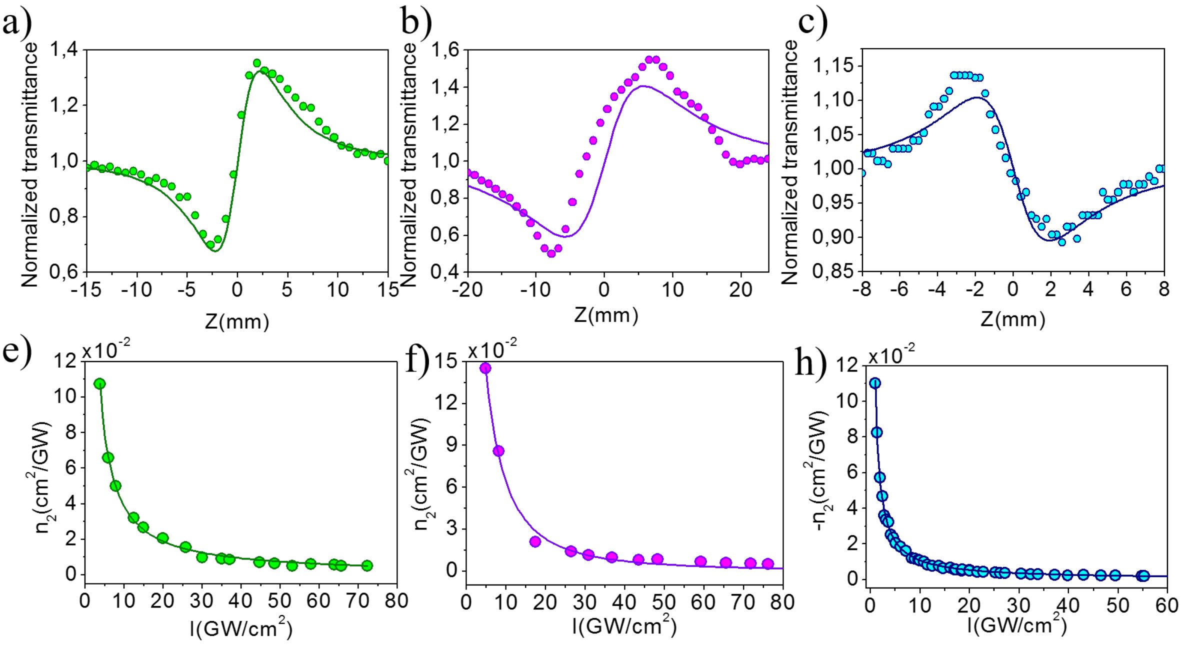

Figure 3.4.2: A typical CA Z-scan curve for the S4 sample, where the positive sign of the nonlinearity for a) Unstretched and b) Stretched with polarization parallel to LSPR, and negative sign for c) Stretched with polarization parallel to TSPR. NLR as a function of intensity: d) Unstretched; e) Stretched with input beam polarization parallel to the stretching direction and f) Stretched with the input beam polarization perpendicular to the stretching direction.

However, as in the case of the NLA, the NLR was intensity dependent (see Figures 3.4.2d)-g)), and at least two approaches could be used to describe the experimental results:

1. The influence of high order terms in the nonlinear optical susceptibility expansion, as in [53, 54]. In this approach, and the NL phase obtained in the Z-scan experiment is written as:

$$\Delta\Phi_0 = \Delta\Phi_0^{(3)} + \Delta\Phi_0^{(5)} + \Delta\Phi_0^{7} + \Delta\Phi_0^{(9)} + \cdots \tag{3.4.2}$$

where $\Delta\Phi_0^{(3)}$, defined in the section 2.2.1 and $\Delta\Phi_0^{(5)}$, $\Delta\Phi_0^{(7)}$, and $\Delta\Phi_0^{(9)}$ are related to the susceptibilities of the third, fifth, seventh, and ninth order, respectively.

$$\begin{array}{cc} \Delta\Phi_0^{(5)} = kn_4 I_0^2 \left[\frac{1-\exp(-2\alpha_0 L)}{2\alpha_0}\right], & \Delta\Phi_0^{(7)} = kn_6 I_0^3 \left[\frac{1-\exp(-3\alpha_0 L)}{3\alpha_0}\right] \\ \Delta\Phi_0^{(9)} = kn_8 I_0^4 \left[\frac{1-\exp(-4\alpha_0 L)}{4\alpha_0}\right] & \dots \end{array} . \tag{3.4.3}$$

In addition, considering $\Delta\Phi_0 \ll 1$, and $S \ll 1$, and analogously to the procedure of [24], an expression for the laser transmittance in the far field is obtained as the function of the sample's position, z, that can be written as an expansion of the equation (2.2.13). Doing the theoretical fit using these equations similar to that in ref [53] would lead to invoke the 9th order term in the intensity, which would imply the observation of the 21st order in the nonlinear coefficient. However, the very high number of adjustable terms make this model very susceptible to the adjustment parameters, which is not appropriate.

2. A saturation of the nonlinear index of refraction. We applied a similar analysis as in [55] in order to evaluate the experimental data obtained with the GNR cluster-PVA film. It is important to emphasize that the following physical aspects were considered: (a) we verified that the absorption spectra of the sample did not change before and after the measurements (See Figure (3.4.3)); (b) the measured nonlinear phase shift was less than π and (c) the intensity range employed, up to $70GW/cm^2$, was less than that reported in the work in GNR in colloids [52] and of the same order as employed in the recent work of ref [56] In our case, the best fit to the experimental data was given by:

$$n_2 = \frac{n_{2,0}}{1 + I/I_{SAT}}, \tag{3.4.4}$$

where n_2 given by eq. (3.4.4) is the saturated value of the nonlinear refraction, $n_{2,0}$ is the value at low intensities and I_{SAT} is the saturation intensity.

Figures 3.4.2e) to 3.4.2f) show the experimental results of n_2 as a function of intensity, where the solid line is a fit using eq. (3.4.4). The values of the NLR and corresponding I_{SAT} were obtained from the fittings and are shown in table 3.2. Notice the change in sign for the TSPR, from focusing to defocusing nonlinearity. This is the first time this behavior is observed and measured in PVA-GNR or other film supporting GNR.

Sample	$\mathbf{n_2 \times 10^{-7}(cm^2/W)}$	$\mathbf{I_{sat}(GW/cm^2)}$
Unstretched	1.44	0.25
Stretched Longitudinal	2.63	0.28
Stretched Transversal	−5.98	0.018

Table 3.2: Measured values of nonlinear refraction coefficient and saturation intensity of PVA-GNRs films for an irradiation wavelength of 800 nm.

The absorption spectra were done before and after measurement, in order to guarantee that the high intensities did not introduce damage to the samples. The bankruptcy on the x-axis of figure 3.4.3b) and 3.4.3c) is due to the equipment.

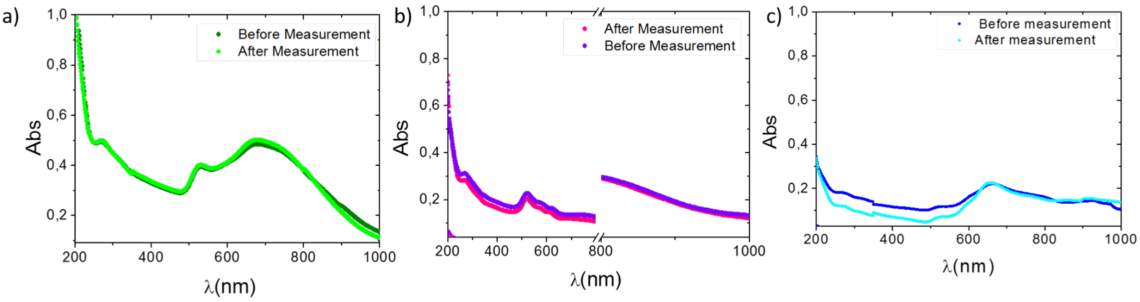

Figure 3.4.3: Linear absorption spectra before and after measurement. a) unstretched, b) strectched longitudinal and c) stretched transversal.

3.5 *M*odeling of plasmon local field

[2] As mentioned above, the observed enhancement (see Table 3.1) in nonlinear optical response of the stretched nanocomposite film, containing clusters of GNRs, can be attributed to coupled plasmon local field, confined at the plasmonic hot spots within the clusters. With this in mind, we applied full-wave electromagnetic analysis to study the collective plasmon effect of clustered nanorods as a function of the number of GNRs in a cluster, as well as of the spacing between separate GNRs in the cluster. Specifically, we studied a nanocomposite comprised of hemi-sphere capped cylinders suspended in a dielectric host as shown in Figure 3.5.1. The optical response of these nanocomposites was obtained using full-wave time-harmonic field analysis as implemented in the COMSOL finite element-based RF solver (`www.comsol.com`). For gold NRs at optical frequencies, the relative dielectric permittivity was modeled using an analytical expression that is based on the Drude-Lorentz model and matches the measured optical response of gold [57]. The computational domain is shown in Figure 3.5.1. A single NR has the following dimensions: length $L = 50nm$, diameter $D = 24nm$, capping hemi-sphere radius $R = 12nm$. The wall-to-wall distance between the rods in each of the triplet, sextet and nonet clusters is set to $5nm$. The end-to-end distance between the rods in the nonet cluster is $4nm$, and in the sextet cluster this distance is varied between 4, 8, 12 and $16nm$. The host dielectric is lossless, with the refractive index $n = 1.53$, corresponding to that of PVA. The full-wave analysis is carried out for the scattered field with the background electric field strength set to $1V/m$. Throughout this section we assume that the incident background field is a uniform plane wave at normal incidence that is linearly polarized at 45 degrees with respect to $x-$axis, unless otherwise is stated. Note that NRs/cluster rotation axis is oriented at 45 degrees to the polarization direction in order to capture both transverse and longitudinal plasmon modes.

One should bear in mind that since the transverse and longitudinal resonances are spectrally resolved/separated, the local plasmon fields at these resonances can be considered quasi-independent of each other, and so are the enhancement factors of the nonlinear properties of the composite material.

---

[2] This section is a textual copy of the reference [15], where I directly collaborated in writting article.

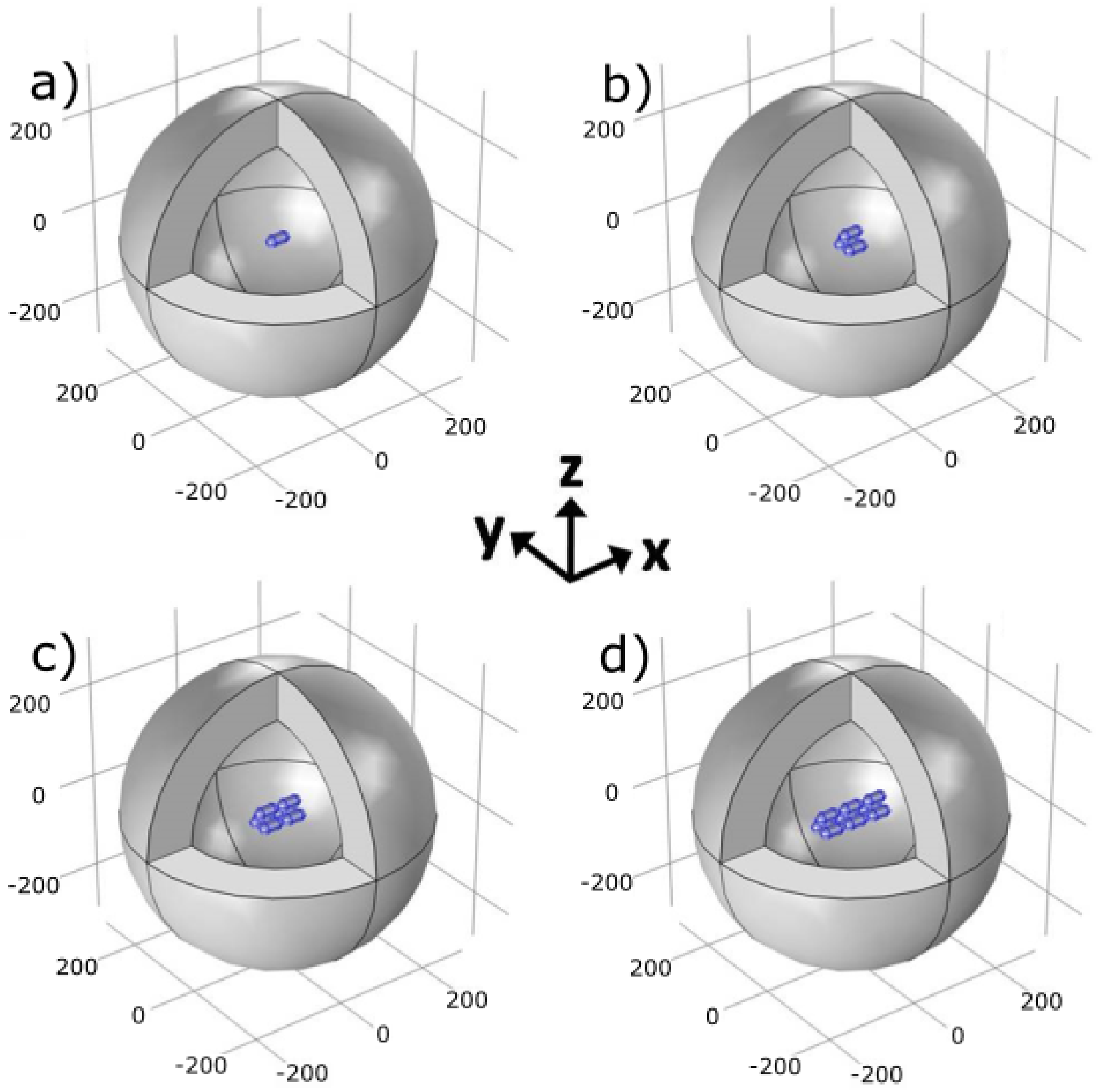

Figure 3.5.1: Computational domain with (a) a single rod, (b) a triplet cluster, (c)a sextet cluster, and (d) a nonet cluster [15].

In this work we were particularly interested in analyzing the enhancement of nonlinear absorption/refraction due to the longitudinal plasmon resonance (the excitation wavelength for the nonlinear characterization is $800nm$), as experimentally verified. It should be noted that fixing the relative orientation between the field vector and NR/cluster rotation axis is absolutely justified because, first, we were comparing relative strengths of local plasmon field generated by a single rod and different size clusters, and, second, the anisotropy of the film samples was induced in the actual experiment via stretching, so that the relative orientation of the field polarization and the clusters axis was a priori known. To model a non-stretched composite, it is more appropriated to illuminate a cluster of any given size by linearly polarized light with a few different orientations of the electric field vector with respect to the main axis of the cluster, to be able to perform orientational averaging.

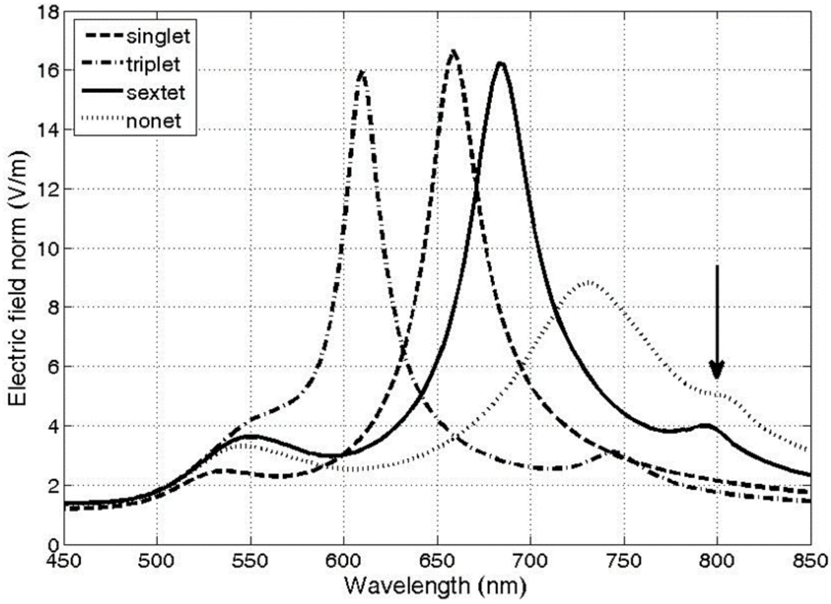

Figure 3.5.2: Surface average of the electric field strength vs wavelength for a single rod, a triplet, a sextet and a nonet clusters. The arrow indicated the wavelength of excitation [15].

The results of calculations are presented in Figures 3.5.2-3.5.3. The spectra of surface averaged electric field strength for a single Au nanorod, a pyramidal arrangement of three rods, and more complex clusters consisting of six (2 pyramidal batches) and nine (three pyramidal batches) rods are presented in Figure 3.5.2. Apparently, plasmonic hot spots between the hemispherical caps of the rods in the sextet and nonet cluster arrangements result in much higher, compared to the single rod and the triplet, local field strength at the wavelength of two-photon excitation (also bear in mind 6- and 9-fold increase of the surface area with respect to the single rod, Figure 3.5.2).

The reason is end-to-end near field coupling between the rods. The distribution of the local field at this particular wavelength of 800 nm for each arrangement of the rods is shown in Figure 3.5.3. The local field is enhanced about 6-fold as compared to the single rod.

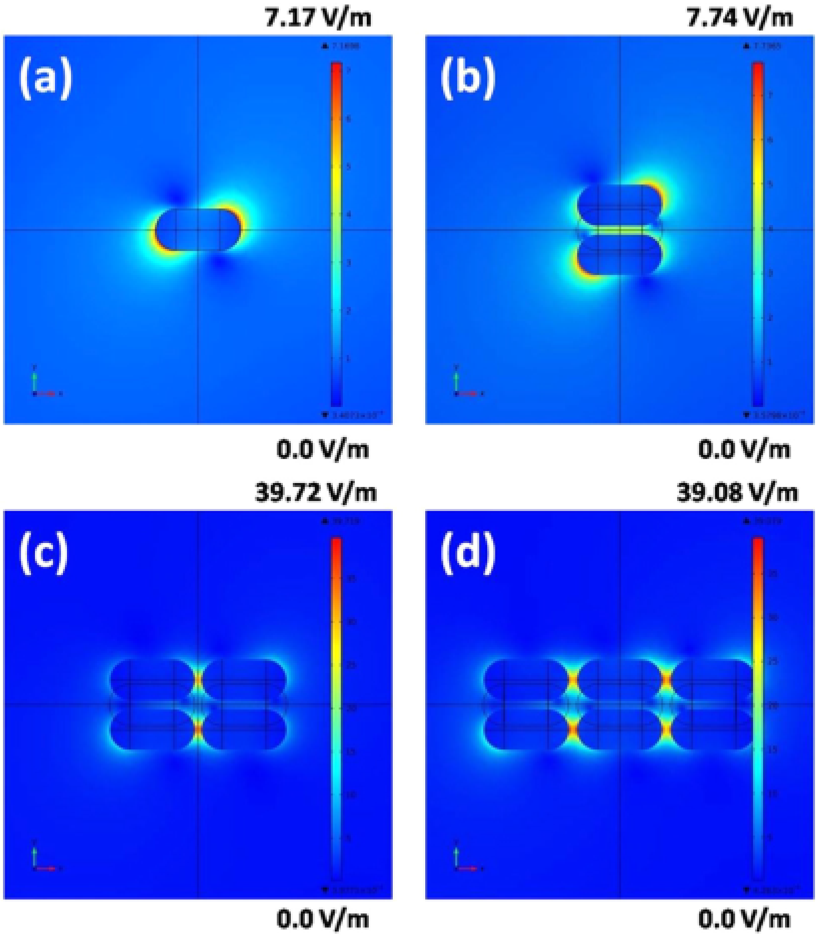

Figure 3.5.3: The distribution of the local field at 800 nm for (a) a single rod, (b) a triplet, (c) a sextet, and (d) a nonet cluster [15].

Plasmon coupling in nanorod aggregates can be qualitatively described by exciton-coupling (or plasmon hybridization) model [58, 59]. In accord with this model, red and blue shifts of the transverse and longitudinal resonances in the extinction spectra of the clusters depend on polarization of the incident field with respect to GNR axis and the arrangement of rods in the assembly (end-to-end or wall-to-wall). The results of our full-wave analysis agree well with this theory, as from the point of view of the exciton-coupling model there is a combination of both H- and J-type aggregates for both senses of polarization (transverse and longitudinal) in the sextet and nonet clusters. The longitudinal plasmon resonance splits into two peaks in this case, both are red-shifted with respect to that of the single rod. However, these peaks may be not resolved in an experiment. Instead, one broad, averaged out peak is usually observed because of different inhomogeneities in individual rod size, number of rods in different clusters, distance between individual rods and such. For example, in the sextet cluster, which is more thoroughly studied here since it corresponds to the experimental situation (see Figure 3.3.4, section II), varying the end-to-end distance, d, between the rods sitting on one inter-particle axis results in a clear red shift of the split longitudinal plasmon resonance as d decreases, because of the increased coupling between the rods in J-type aggregate (Figure 3.5.4).

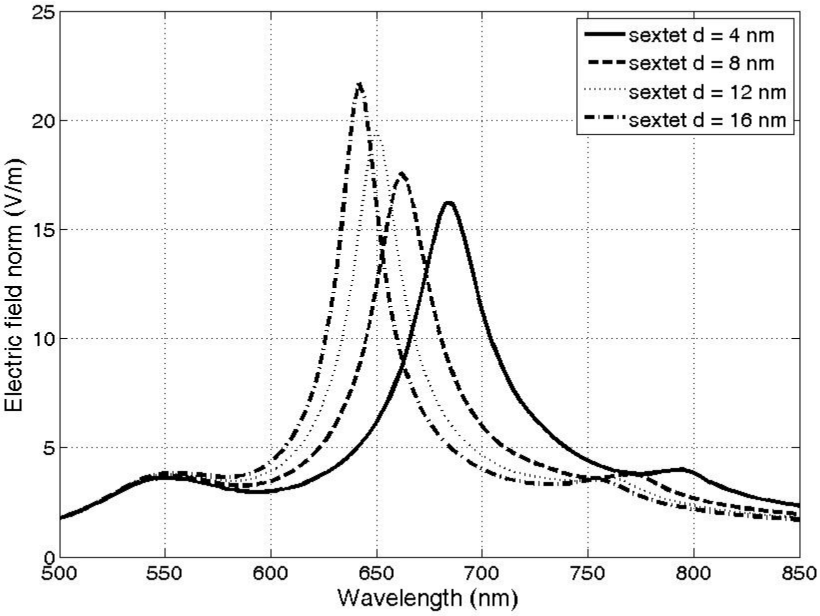

Figure 3.5.4: Surface average of local field strength vs wavelength for a sextet cluster with different end-to-end distances, d [15].

The increased coupling also leads to the local plasmon field growing up dramatically. Compared to the local field of the single rod, the field at the hot spots of the tightest sextet cluster (end-to-end separation of 4 nm) is enhanced 6-fold (see Figures 3.5.3 and 3.5.5). Note that at the same end-to-end separation (4 nm) the enhancement of the field at the hot spots in the nonet cluster is slightly weaker. The saturation of local plasmon field can be one reason.

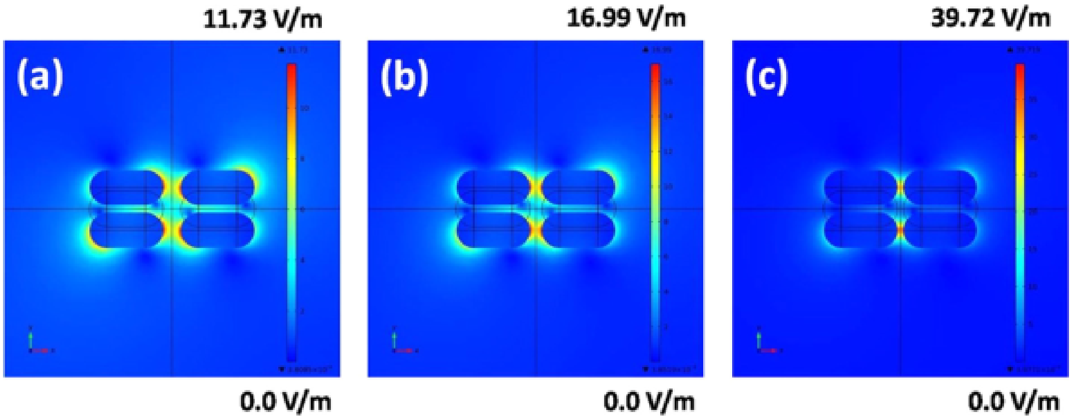

Figure 3.5.5: The distribution of the local field at $800nm$ for a sextet cluster with rod end-to-end distance, d, of (a) $12nm$, (b) $8nm$ and (c) $4nm$ [15].

At a first glance the experimentally obtained 57-fold enhancement of NLA appears to be much smaller than predicted by calculations. Let us analyze two situations:

1. The enhancement for the perfect arrangement of the sextet clusters with the end-to-end distance of 4 nanometers relative to a single nanorod, which means comparing a clustered sample to nanorod dispersion (Figure 3.5.3).
2. The relative enhancement for the perfect arrangement of the same sextet clusters with the electric field polarized parallel, perpendicular and at 45 degrees to the cluster's rotation axis.

In the first case, the 6-fold enhancement of the local field at $800nm$ wavelength results in the $6^4 = 1296$-fold enhancement of nonlinear absorption. However, in this case comparison is done between a clustered and a non-clustered samples, when stretching is not considered. In the second case, illustrated in Figure 3.5.6, the difference between the local plasmon fields induced by the transverse (Figure 3.5.6(a)) and longitudinal (Figure 3.5.6(c)) polarization is almost 7-fold, which reflects the fact, that no enhancement of two-photon absorption was observed in the case when the incident light was polarized perpendicular to the stretching direction. In the unstretched sample the relative orientation of clusters rotation axes and the polarization direction is not fixed. Some of the clusters can be parallel to the polarization vector, some can be perpendicular and some can have 45 degrees orientation. With the strength of the local plasmon field in the case of pure longitudinal plasmon excitation 1.4 times that of the case when the field is polarized at 45 degrees with respect to the cluster rotation axis (Figures 3.5.6(b)) and 7-fold increase compared to the pure transverse excitation, a very crude averaged value of the relative local field enhancement between a stretched and an unstretched samples would be 4-fold, which equates to $4^4 = 256$-fold enhancement of nonlinear absorption. This is the case when only sextet clusters are present in the composite. With some isolated rods and a certain percentage of smaller than sextet clusters the predicted enhancement of the nonlinear absorption would come closer to the experimental number.

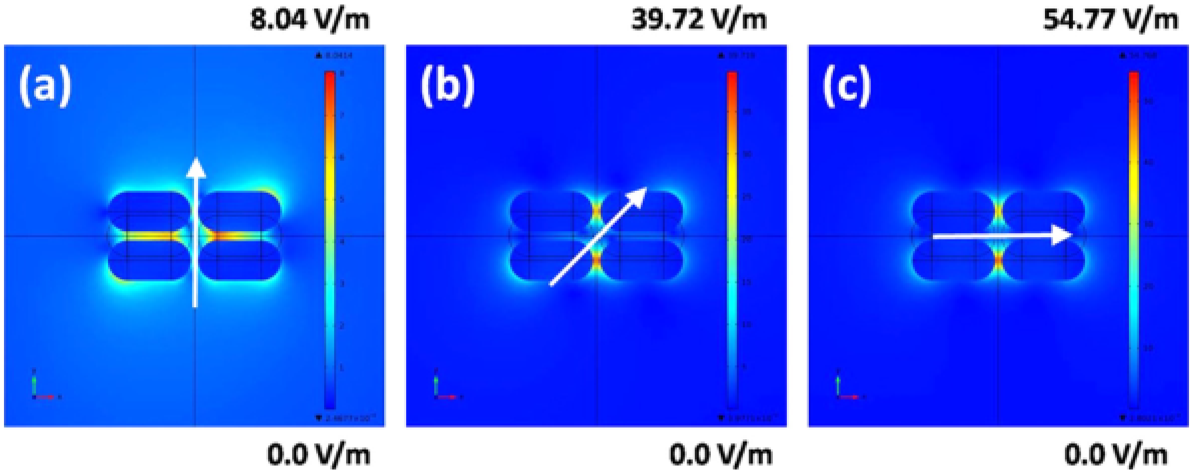

Figure 3.5.6: The distribution of the local field at 800 nm for a sextet cluster with the end-to-end separation of $4nm$ and the incident electric field polarized (a) perpendicular to the cluster axis; (b) at 45 degrees to the axis of the cluster; and (c) parallel to the axis of the cluster. The white arrows indicate the polarization direction [15].

3.6 Discussion

The physical origin of the NLA has been clarified before as due to one-photon absorption in the LSPR wavelength region [52], arising from the local field enhancement introduced by plasmon oscillations as well as nonradiative plasmon decay. In this way, electron—hole pairs are efficiently created in the sp band of the GNR. The collective assembly of the aligned GNR leads to the noticeable saturation of the NLA, as observed here. This enhancement has been confirmed using full wave electromagnetic analysis, and the predict enhancement matched well the observed NLA enhancement factor. The use of femtosecond pulses also plays an important role, since the time scale of the dynamics of the electron-phonon processes involved is of the order of a few picoseconds [60, 61, 56]. We did not observe any other effects in the NLA, such as reverse NLA due to two-photon absorption, as in refs [52, 60], both in water solution. NLR has also been studied in earlier work. The obtained values of n_2 for polarizations parallel ($n_{2||}$) and perpendicular ($n_{2\perp}$) to the assembly of GNR in the electrospun film [56] or solution [62, 63] are summarized in table 3.3, together with our results. No clustering effect is reported in ref [56]. The saturation of the NLR most certainly arises from the same physical origin as the saturation of the NLA, the one-photon absorption in the LSPR wavelength region. In refs [63, 56] the magnitude of the nonlinear refractive index in the parallel polarization to the LSPR, was higher than in the transverse polarization, i.e. parallel to the TSPR. This data is not available from ref [62] In our case, this ratio of ~ 0.43, i.e., the NLR with the polarization paralell to the TSPR was higher than the polarization parallel to the LSPR.

$Reference,$ $technique$	$\lambda_{pump},$ τ_{pump}	I_{pump}	$n_{2,Random}$ (cm^2/W)	$n_{2,\parallel}$ (cm^2/W)	$n_{2,\perp}$ (cm^2/W)	$Enhancement$ $factor$ $(n_{2\parallel}/n_{2\perp})$
$Zhang\,et\,al.$ $Z - scan$	$800nm$ $100fs$	$25GW/cm^2$	$--$	26.41×10^{-12}	3.52×10^{-12}	7.5
$*Padilha\,et\,al.$ $Z - scan$	$770nm$ $140fs$	$***$	-7.8×10^{-15}	-9.4×10^{-15}	-5.0×10^{-15}	~ 1.9
$**Tsutsui\,et\,al.$ $Z - scan$	$800nm$ $90fs$		1.64×10^{-15}	$--$	$--$	$--$
$This\,work,$ $Z - scan$	$800nm$ $100fs$	$< 5GW/cm^2$	1.44×10^{-11}	2.63×10^{-11}	-5.98×10^{-11}	~ 0.43

Table 3.3: Tabulated values of nonlinear refraction coefficients of GNRs in colloid [63, 62] and films [56, 15] for an irradiation wavelength around $800nm$.

* GNR in Toluene suspension, aligned with electric field ~11kV/cm
**GNR in suspension, not aligned
***Energy of 12nJ/pulse

An interesting feature is the change in the sign of the nonlinearity from the polarization excitation parallel to the LSPR compared to excitation of the TSPR. Sign reversal of NLR is known from gold nanoparticles in soda-lime glass substrate [64], and has been explained as due to the annealing process employed for the nanoparticles size control. In GNR in solution prepared by electrochemical methods [65], change in sign of the NLR has been observed and demonstrated to be due to change in shape of the nanorods to more spherical nanoparticles due to the laser irradiation. For the results shown here, the sign reversal of the NLR is mainly due to the pump wavelength position respective to the TSPR and LSPR resonances. In the former case, the pump wavelength is well below the TSPR absorption, thus leading to a positive (self-focusing) nonlinearity, as observed in Figure 3.4.2. On the other hand, being closer and on the red wavelength side of the LSPR absorption (see Figure 3.4.2) the manifested self-defocusing nonlinearity is therefore explained. Again, a one-photon process was dominant in the NLR, and lead to a saturated behavior.

3.7 Conclusions

We have described the fabrication, morphological and nonlinear optical characterization of gold nanorod cluster-PVA nanocomposites prepared by modified seed mediated method and subsequential purification procedure. Uniaxial alignment was obtained by mechanically stretching the PVA-based films. Using the Z-scan technique with an excitation source at 800 nm and 100 fs pulses, saturation of both nonlinear absorption and nonlinear refraction were observed. The experimental results, supported by finite element analysis of local electric field distribution in the arrays of gold nanorod clusters, were explained in light of a plasmonic effect arising from the gold nanorod clusters aligned in the stretched polymeric matrix. The theoretical calculation of the electric field enhancement due to the clustering of the GNR ($\sim$ 50) showed a remarkable agreement with the measured NLA coefficient enhancement ($\sim$ 57) when the relative concentration (theory to experiment) was taken into account. As we mentioned before, the overall behavior for our results is quantitatively consistent with models of local field enhancement within the clusters, and thus establishes a rational for the morphological design of optical nanocomposites with plasmonic nonlinearity. For further understanding of the role of the GNR clusters, studies employing confocal microscopy shall be performed to analyze single and clustered GNR.

4 Control of the optical behaviour of AuNRs in Cargille Oil with Electric Field

4.1 Introduction

A method used to induce alignment moments of AuNRs suspended in liquid solutions is applying a electric field. Electric fields generated between micrometer spaced electrodes did achieve high enough field strengths to induce alignment moments that overcame the Brownian motion in a colloidal AuNR solution. However, in the reference [66], besides generating alignment moments, the electric field also induced dielectrophoretic forces in the rods, which caused their accumulation around the electrodes and hence a nonuniform spatial distribution.

To counter accumulation around the electrodes effect, we prepared a cuvette with Indium Tin Oxide (ITO) films deposited on the glass slides used to make it lamines to avoid introducing electrodes into the solution. ITO is one of the most widely used transparent conducting oxides because of its two main properties: its electrical conductivity and optical transparency, as well as the ease with which it can be deposited as a thin film. As with all conductive films, a compromise must be made between conductivity and transparency, since increasing the thickness and increasing the concentration of charge carriers increases the material's conductivity, but decreases its transparency (see Figure 4.1.1a)). The lamina ITO was corroded making the design of the electrodes as shown in Figure 4.1.1b) (See Appendix B).

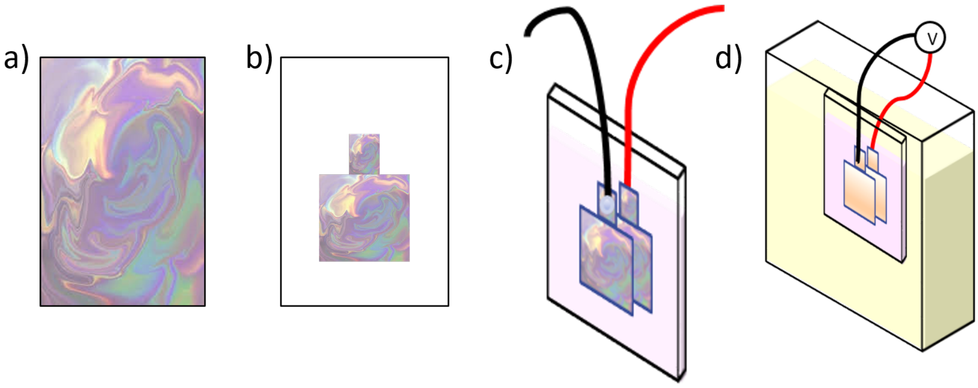

Figure 4.1.1: Cuvette: a) Representation of the ITO lamina b) Electrode (ITO lamina corroed) c) cuvette of $1mm$ d) final configuration.

For the application of the voltage it necessary another Teflon cuvette holder of $35mm$. This has two windows ($1mm$ thick microscope slides) along light propagation direction, separated by $34mm$ and containing transformer oil (Lubrax AV 24) to avoid dielectric breakdown (See Figure 4.1.1c) and 4.1.2b)). A cuvette is needed to avoid creating arc due to high voltage. In the interior was placed to $1mm$ cuvette containing gold nanoparticles in Cargille oil (Figures 4.1.1c) and 4.1.2c)). The real cuvettes used in the experiment showed in Figure 4.1.2.

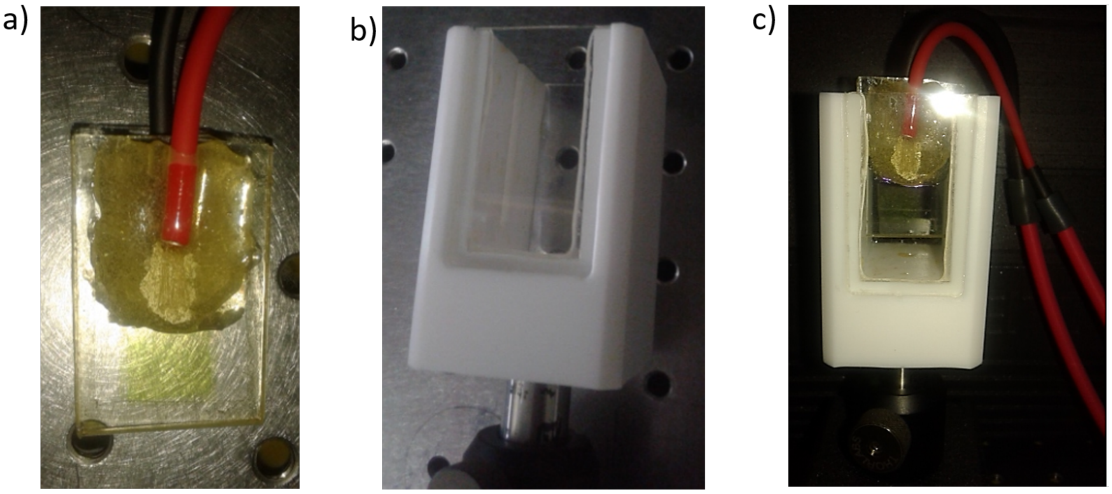

Figure 4.1.2: The cuvettes used in the experiment. a) cuvette of $1mm$ with electrodes. b) Teflon cuvette holder c) Final configuration.

To perform the linear and nonlinear optical experiments as a function of the NRs electric-field induced orientation was used the high voltage system consisted in a sinusoidal function generator (SRS DS345) feeding a 2000x voltage amplifier (Trek 20/20C).

The NRs can be aligned in colloids with external electric fields, thus allowing dynamically controlling the system's optical properties.

4.2 Gold Colloid Preparation

Gold Nanorods with aspect ratio $L/d \sim 3.2$, length $L = 74mm$ and width: $d = 23nm$ originally in deionized water (Nanopartz, product number A12-25-700-CTAB, 60 ppm) dispersed in Cargille oil (Series A, nD=1.5700) were employed.

In order to transfer the NRs from deionized water to Cargille oil, the nanoparticles were first transferred to an organic medium (toluene) by taking $1mL$ of a solution composed by $0.1g$ of thiol-terminated polystyrene and $4mL$ of tetrahydrofuran (THF). This solution was mixed to $2mL$ of the AuNRs solution in DI water in a vial, which in sequence was sonicated for 1 minute. This last step was repeated placing another $1mL$ of the polystyrene-THF solution into the vial. The mixture stand for 15 minutes and then the supernatant was removed. At this point, the AuNRs stuck on the vial wall. $2mL$ of toluene were added to the vial to redisperse the AuNRs. The transfer of AuNRs from toluene to Cargille oil is made by first placing in the glass vial a given volume of the oil and upon it the same quantity of AuNRs in toluene. After a few days, toluene evaporates and the AuNRs will have diffused into the oil. These samples were prepared by Isabel Carvalho and collaborators at Pontificia Universidade Catolica de Rio de Janeiro (PUC).

4.3 Linear Optical Characterization

In order to study the influence of the electric field in colloidal samples, we performed extinction measurements using unpolarized white light (Ocean Optics HL-2000-LL) and recording the extinction with a USB spectrometer (Ocean Optics HR4000) as a function of the voltage applied to the ITO pads.

The experimental results for the unpolarized linear optical transmission of GNRs are shown in Figure 4.3.1a). The response from nanorods is dependent on the electric field applied with the maximum absorption located at $775nm$ for L-SPR mode like to references [67, 68]. The Figure 4.3.1b) shown the variation of the maximum peak of the L-SPR with the electric field. The longitudinal peak is suppressed when the electric field is applied. The peak of the transverse mode T-SPR is located at $550nm$ but the little visibility of the transverse mode and the broadening of the longitudinal mode in Figure 4.3.1a) is due to the aggregation of the nanorods in the colloidal sample.

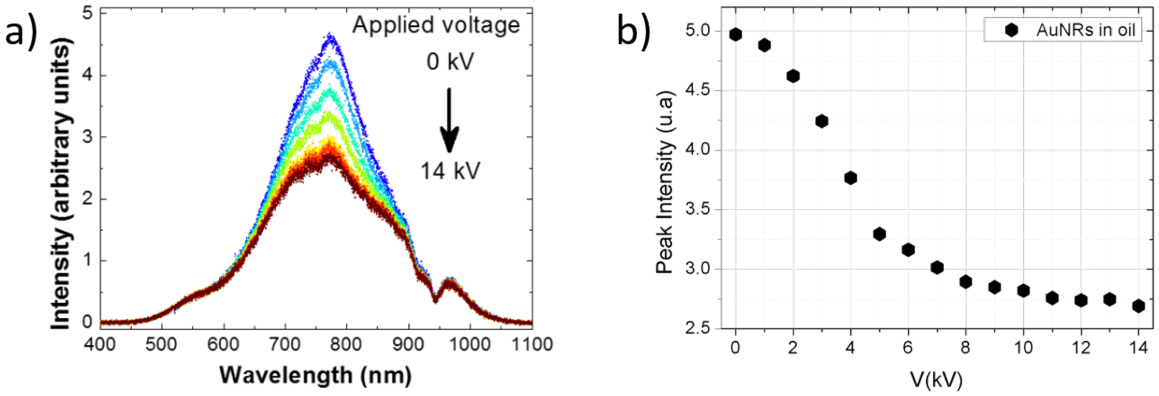

Figure 4.3.1: a) The extinction coefficient in arbitrarie units with applied voltage and b)Variation of the absorption peak as we increase the applied voltage.

4.4 Nonlinear Optical Characterization

For to explore the nonlinear properties of AuNRs colloids in Cargille oil, we use the two techniques: Beam Collimated Hartmann-Shack and Dual arm Z-scan.

The initial idea was to use the Hartmann-Shack wavefront sensor due to the experimental setup is simple to implement and because the sample is fixed, which helps us in our objective of applying an electric field to a liquid sample. Once we obtained a robust and safe configuration for the application of the electric field, we decided to use the Z-scan technique to observe the behavior of the nonlinear absorption with the application of the electric field.

In 2009, Padilha *et al.* partially oriented Au NRs dispersed in toluene inside a 3 mm thick cuvette. They measured the dependence of the NLR and NLA index n_2, β_2 with the application of voltages up to $11kV$ for laser polarizations perpendicular and parallel to the applied electric field, obtaining the n2 value compared to when one does not apply any voltage, and saturated absorption for any value of the electric field applied [63].

This article was the only find in the literature in the study of the NLO properties using the electric field in colloids of metallic nanoparticles.

4.4.1 Beam collimated using a HSWFS

The experimental scheme used is the so-called collimated beam configuration. We investigated two different excitation regimes: In the first one, a Ti:Sapphire laser (Coherent Mira, $800nm$, $150fs$, $76MHz$, beam diameter: $1.13mm$), and due to its high repetition rate one observes thermal effects. In the second one, an Ti:Sapphire laser (Coherent Libra, $800nm$, $120fs$, $1kHz$, beam diameter: $0.78mm$), allowing to investigate electronic effects.

In order to guarantee that the contributions of the nonlinear properties are due only to the nanoparticles, we quantify the contribution of Cargille oil to the colloid nonlinear refraction. In the first time, we measured the variation of the C5 with the intensity for both regimes of the repetition rate. In the Figures 4.4.1a) and 4.4.1c) we have the negative contribution for NLR. How the n_2 is proportional to C5 and using the equation (2.2.29) with respective factor correction, we obtain the values for the nonlinear refraction coefficients. The values calculated are $n_2^{76MHz} = -8.8 \times 10^{-15} cm^2/W$ and $n_2^{1kHz} = -5.0 \times 10^{-16} cm^2/W$. The n_2^{76MHz} is an one order of magnitud higher than n_2^{1kHz}. Due to the Cargille oil having a nonlinear contribution, we need to calculate de dependence of this nonlinearities with the electric field. In the Fugures 4.4.1b) and 4.4.1d) show the Δn_2 as a function of the applied voltage. Moreover, the n_2 not change and there is no dependence of the such properties with the applied voltage. The value of the intensity was fixed.

The Δn_2 was defined as:

$$\Delta n_2 = n_2(E \neq 0) - n_2(E = 0). \tag{4.4.1}$$

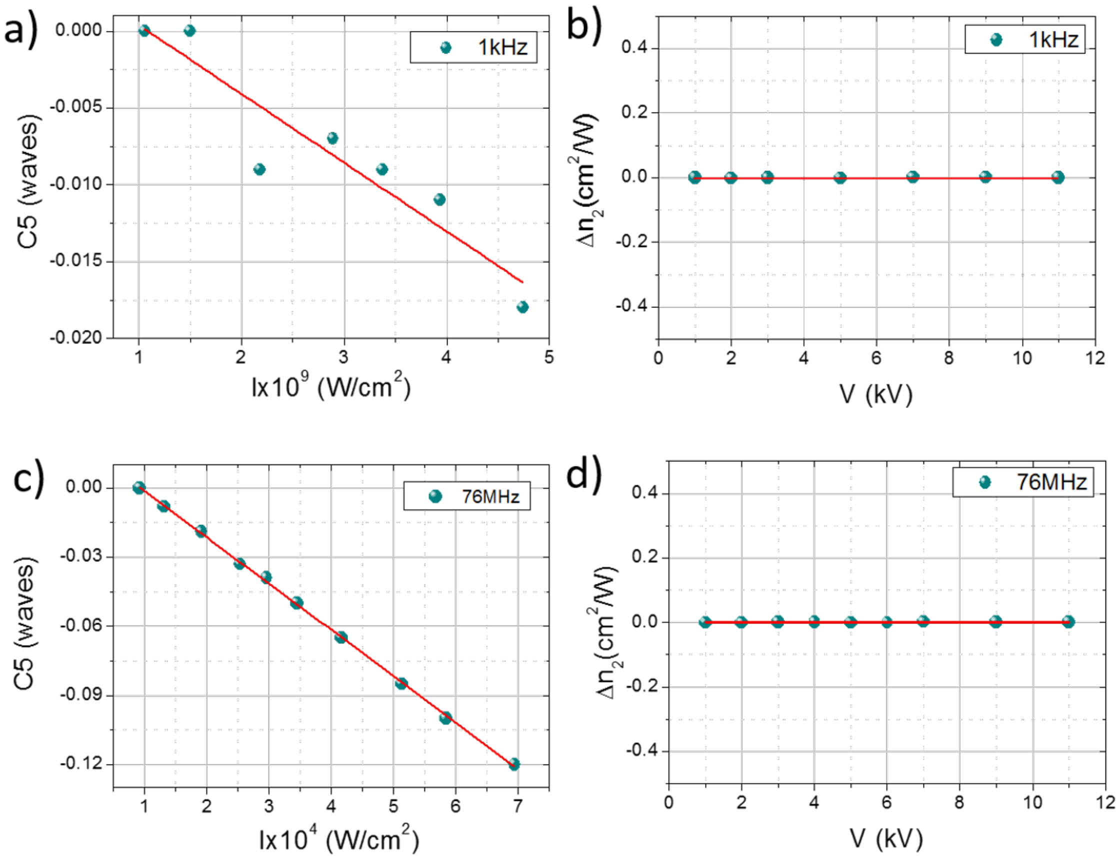

Figure 4.4.1: Measurements of the NLR properties of the Cargille oil. Dependence of the C5 with the intensity for a) $1kHz$, d) $76MHz$ and the variation of the NLR with the electric field for b) $1kHz$ and d) $76MHz$.

We performed the same protocol for investigating the behavior of Δn_2 from the AuNRs as a function of the applied voltage V, for a fixed excitation laser intensity. For high repetition rate, the value of the intensity was $4.5{\times}10^5 W/cm^2$. The Δn_2 value for $V = 0$ was taken 0. Increasing the voltage applied in intervals of $1kV$ we can to observed the influence of the electric field in the nonlinearities of the AuNRS (Figure 4.4.2). From $9kV$ the variation of n_2 seems to be constant. For low repetition rate the value of the intensity was $8.8 \times 10^9 W/cm^2$. We can to observed the same tends of the NLR. The variation in both cases was approximately six times of the initial value.

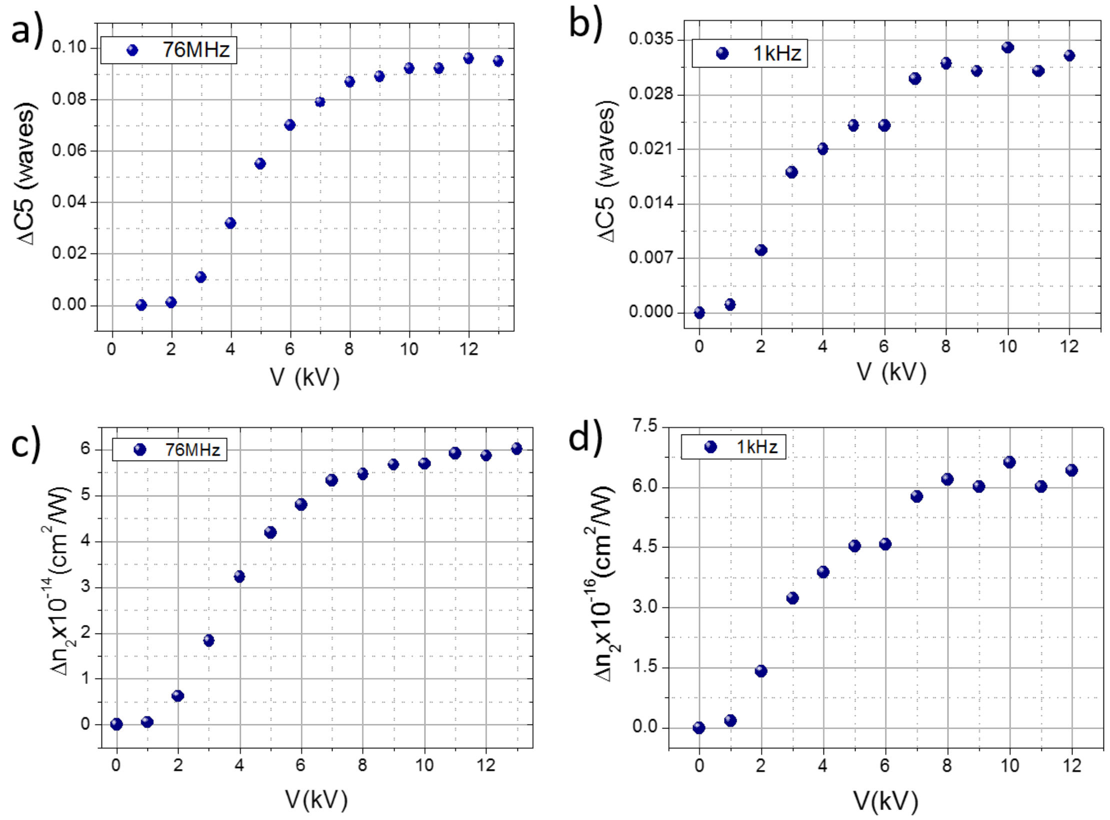

Figure 4.4.2: Variation of defocusing Zernike coefficient with applied tension in excitation regime: a) 1kHz and b) 76 MHz .

To obtain the value of the n_2 of the AuNRs at zero applied voltage, we got the $C5$ measured for the Cargille oil at the intensity $4.5 \times 10^5 W/cm^2$ (high repetition rate) and $8.8 \times 10^9 W/cm^2$ (low repetition rate) and subtracted this value from that obtained for the colloid. The results thus reflect directly the influence of the AuNRs presence. We got $n_2 = -1.0 \times 10^{-13} cm^2/W$ for $76MHz$ and $n_2 = -1.5 \times 10^{-16} cm^2/W$ for $1kHz$. The results for Δn_2 are shown in Figure 4.4.2. The diference of n_2 between the two regimes is of 3 orders of magnitude. However, the trends are the same in both cases.

Repetition rate	*Diameter beam (mm)*	*Intensity* (W/cm^2)	$n_2(cm^2/W)$ *Cargille Oil*	$n_2(cm^2/W)$ $AuNRs\,(E=0)$
1kHz	0.78	8.8×10^9	$-5,01 \times 10^{-16}$	$-1,5 \times 10^{-16}$
76MHz	1.13	4.5×10^5	$-5,75 \times 10^{-14}$	$-1,0 \times 10^{-13}$

Table 4.1: Values of n_2 for the Cargille oil and AuNRs without the applied electric field.

One can understand this by recognizing that the L-SPR is the one which strongly absorbs light and converts it into heat via Joule effect. The application of the external voltage makes the average angle between the NRs longer axis and the laser polarization direction increase. Thus, there is smaller coupling between light and the L-SPR, leading to a smaller energy dissipation as heat and thus decreasing the thermal effects.

4.4.2 Z-scan measurements

The previous experiments (Section 4.4) showed that it is possible to control the nonlinear refractive index of AuNRs colloids, which is potentially interesting for applications in devices. However, for applications, one should be concerned with the absorption features of their active elements. Thus, in order to make a complete characterization of such systems, it is important to study how their nonlinear absorption coefficient β_2 behaves when the samples are subjected to a high applied voltage along the excitation light's propagation direction. Since our composite cuvette showed itself to be very robust and safe in dealing with high voltages, we decided to make Z-Scan measurements for investigating the behavior of n_2 and β_2 in these Au NRs colloids.

For the Z-Scan measurements we used only the high repetition rate excitation (76MHz) in order to check the behavior of the nonlinearities (both, NLA and NLR) in the presence of a applied field. We then studied the agreement between the results obtained using this technique and the results reported in Section 4.4. The experimental setup used was described in the section 2.2.2.

Nonlinear Refraction (Closed-aperture Z-scan)

The results for closed-aperture Z-scan can be seen in Figure 4.4.3. As the applied voltage increases, the nanoparticles tend to align in the direction perpendicular to the incident light and the index of nonlinear refraction "decreases". The sign of the NLR is negative in agreement with results did with Beam collimated HS and is due to self-defocusing. The solids lines representing the fitting curves doing with the equation (2.2.13). In the Figure 4.4.3b) we presenting the traces of Z-scan for $0kV$ and $10kV$ to apreciate better the diferences.

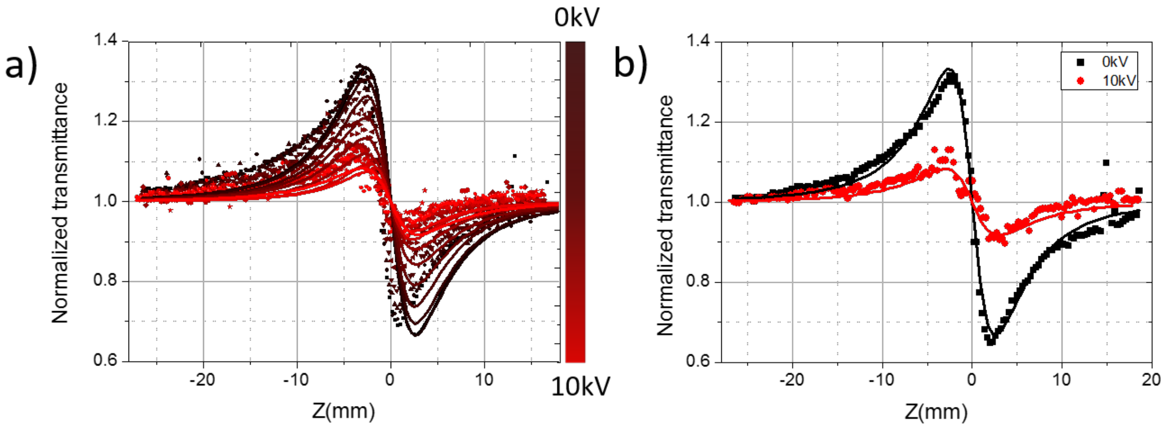

Figure 4.4.3: Traces of closed aperture Z-scan. a)Variation of the NLR with the applied voltage. b) Closed Z-scan for 0kV and 10kV

The values for n_2 was obtained with the fitting for the Closed-Z scan. In the Figure 4.4.4a) plots the n_2 values with the applied voltage. The intensity used was $I_0 = 2.53GW/cm^2$.

In order to compare the values obtained in the two configurations, we plots in Figure 4.4.4b) both results and show a good agreement between both techniques.

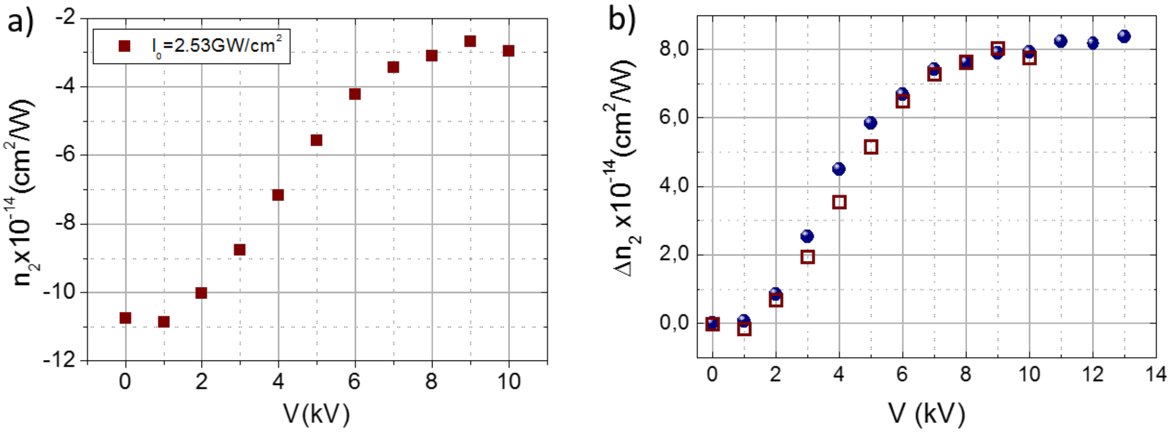

Figure 4.4.4: a)Variation of n_2 with applied voltage. b) Comparation between Z-scan Technique (red squares) and Beam Collimated Hartmann-Shack (Blue points).

Nonlinear Absorption (Open-aperture Z-scan)

We want to know how is the behavior of the nonlinear absorption. The results for NLA is shown in Figure 4.4.5. The black squares representing the experimental data and the red solid curve representing the fitting with the equation (2.2.16). We observed nonlinear absorption. However when the applied voltage reached the vale of $5kV$ NLA has vanished or reduced to the noise level.

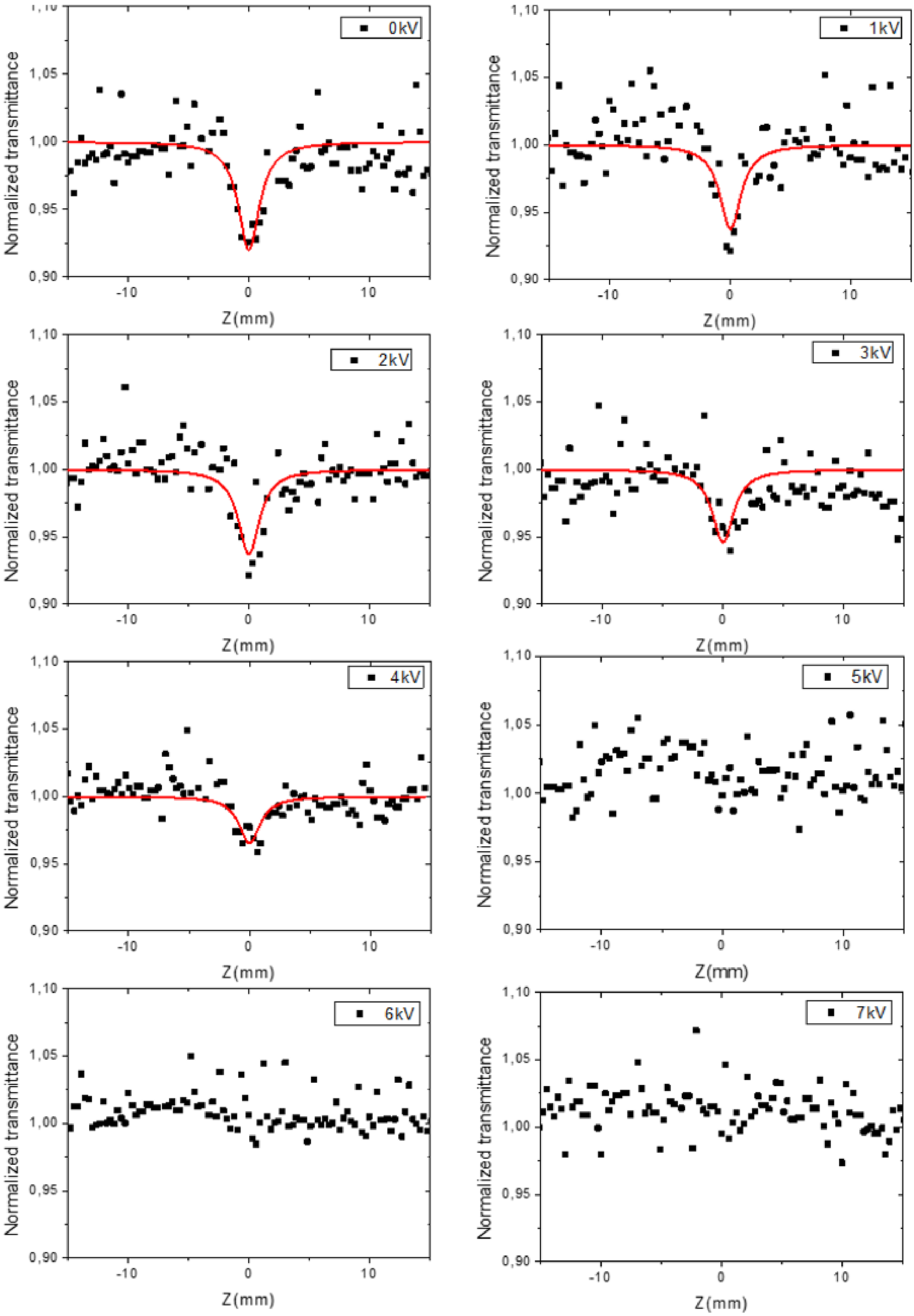

Figure 4.4.5: Open Z-scan curve for the AuNRs in Cargille oil varing the voltage. When the voltage is increased the nonlinear absorption vanishes. The red curve is the fitting using the equation (2.2.16).

In the Figure 4.4.6, we put in the same picture the data for $0kV$ and $10kV$ to observe the difference. The values for β_2 was calculated using the equation (2.2.16) for the fitting. The variation of the NLA with the voltage is shown in Figure (4.4.6)a).

We have positive values for β_2. The maximum values are for $0kV$ and are suppressed for values of the applied voltage bigger than $5kV$.

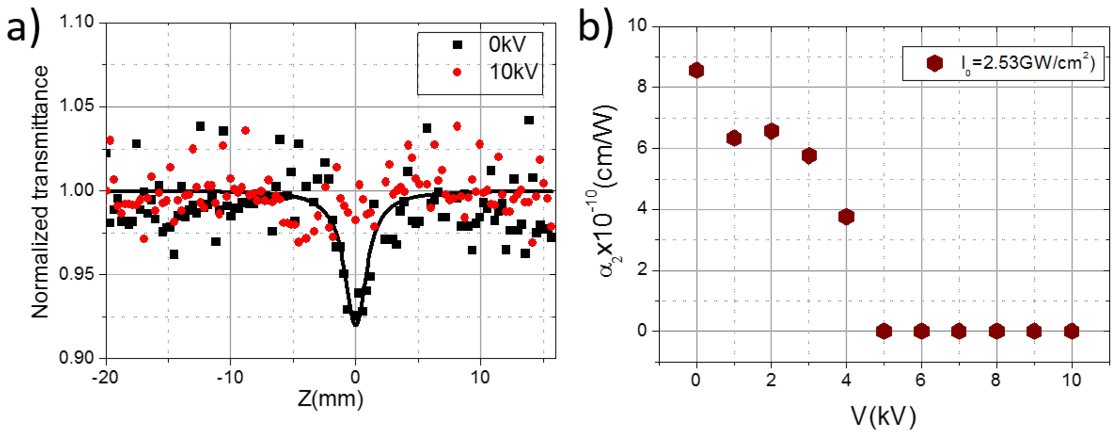

Figure 4.4.6: a)NLA for the 0 kV and 10kV. The black curve is the fitting for $0kV$. b)Variation of NLA coefficient with the applied voltage.

4.5 Discussion on the influence of linear absorption and n_2 in NLA of AuNRs colloids

Since the nonlinear refractive index for both repetition rates does not change the sign, we can ensure that the predominant effect of the nonlinearity is thermal. For that, we can not be expected to find positive values for NLA in the open-aperture Z-scan experiments. In this way, we performed a literature search and found the work of reference [69], which the authors relevant to our discussion.

In the case of Kerr-type nonlinearities, the expressions relating the refractive index and the absorption coefficient with the intensity of the electromagnetic wave are expressed in the equations (2.2.3) and (2.2.4). In a system showing a negligible absorption ($\alpha_0 \approx 0$), the nonlinear refractive index n_2 and the nonlinear absorption coefficient β_2 are proportional to the real and imaginary parts of $\chi^{(3)}$ through the following expressions in the international system (SI) of units:

$$\chi_R^{(3)} = (4/3)n_0^2\epsilon_0 c n_2 \tag{4.5.1}$$

$$\chi_I^{(3)} = \left(n_0^2\epsilon_0 c\lambda/3\pi\right)\beta_2 \tag{4.5.2}$$

In spite of the assumption of negligible absorption implicit in Eqs. (4.5.1)-(4.5.2), they have been used very often for finding the values of $\chi_R^{(3)}$ and $\chi_I^{(3)}$ in absorbing systems k, particularly since Z-scan measurements became one of the most popular methods for the assessment of third-order nonlinearities. In reference [69] the authors derive a set of expressions relating $\chi_R^{(3)}$, $\chi_I^{(3)}$, n_2 and β_2 valid for absorbing systems.

$$\chi_R^{(3)} = (4n_0\epsilon_0 c/3)\,(n_0 n_2 + k_0 k_2) \tag{4.5.3}$$

$$\chi_I^{(3)} = (4n_0\epsilon_0 c/3)\,(n_0 k_2 + k_0 n_2) \tag{4.5.4}$$

Both expressions (4.5.3) and (4.5.4) reduce to the relations given in Eqs. (4.5.14.5.2) when the absorption of the system is negligible ($\alpha_0 \approx 0$). In absorbing systems, the NLA and NLR are thus the consequence of the interplay between the real and imaginary parts of the first- and third-order susceptibilities, and n_2 and β_2 are no longer proportional to the real and imaginary parts of $\chi^{(3)}$. This can be seen more clearly when looking at the inverse expressions obtained from Eqs. (4.5.3) and (4.5.4):

$$n_2 = \frac{3}{4\epsilon_0 c\,(n_0^2 + k_0^2)}\left[\chi_R^{(3)} + \frac{k_0}{n_0}\chi_I^{(3)}\right] \tag{4.5.5}$$

$$k_2 = \frac{3}{4\epsilon_0 c\,(n_0^2 + k_0^2)}\left[\chi_I^{(3)} - \frac{k_0}{n_0}\chi_R^{(3)}\right] \tag{4.5.6}$$

Using $\beta = 4\pi k/\lambda$.

$$\beta_2 = \frac{3\pi}{\lambda\epsilon_0 c\,(n_0^2 + k_0^2)}\left[\chi_I^{(3)} - \frac{k_0}{n_0}\chi_R^{(3)}\right] \tag{4.5.7}$$

If $\chi_I^{(3)} = 0$ in the equations (4.5.5) and (4.5.7), we have:

$$n_2 = \frac{3}{4\epsilon_0 c\,(n_0^2 + k_0^2)}\left[\chi_R^{(3)}\right] \tag{4.5.8}$$

and,

$$\beta_2 = \left(-\frac{\alpha_0}{n_0}\right) n_2 \tag{4.5.9}$$

This indicates that the NLA has a positive signal when the nonlinear refraction has a negative signal in absorbing media near of the resonance. We can conclude that the results for NLA are not due to two-photon absorption and instead, are due to the influence of α_0 and n_2 in the values for β_2. This is the most important result, supported by the theoretical prediction made by Coso in the reference [69].

4.6 Conclusions

Using the Beam Collimated Hartmann-Shack we characterized nonlinear optical properties in AuNRs in Cargille oil. The technique use a Hartmann-Shack sensor used in adaptative optics. The advantages of this method remain in the easy implementation, the facility for performing optical alignement of the system and the sample is fixed. As the electric field applied is very intense, we used a cuvette of $35mm$ with transformer oil and a cuvette of $1mm$ containing the sample. The NLR was measured using the H-S technique for both regime (at 150fs, 76MHz) and (100fs, 1kHz). The NLR shown negatives values related to self-defocusing. When we increasing the electric field the longitudinal plasmonic mode decreasing and the NLR increasing. The variation of the NLR in both regimes was six times the initial value. The initial idea for to use the both regimes was studied the electronic and thermal effects in the nonlinearities. But we can not observe changes in the signal of the n_2 indicating that the predominant contribution of the NLO properties is thermal.

The Z-scan technique was used for measuring both, nonlinear refraction and nonlinear absorption to understand the behavior of these in AuNRs in Cargille oil under electric field application. This was done for high repetition rate excitation and we confirm the self-defocusing behavior of the NLR and good agreement between the values measured in both methods (Z-scan and Beam Collimated Hartmann-Shack). On the other hand, the behavior of the nonlinear absorption was unexpected. Positive values for the NLA was find. The majorities of the papers in the literature showing a saturation of the nonlinear absorption for Gold nanorods. On the other hand, the excitation beam was $800nm$, and this value is strongly resonant with the longitudinal SPR.

This led us to search the literature for mechanisms to explain this behavior. Coso and Solis [69] demonstrated that many scientists make a mistake when calculating the magnitude of the third-order susceptibilities. They affirm that when dealing with absorbing media, one needs to use other equations to obtain this values. Their approach lead us to understand our results. The sample is initially ($E = 0$) an absorbing sample (high α_0), and when we applied the electric field the values for the α_0 is decreasing (making the sample less absorbing). The positive value for the NLA when $E = 0kV$ is a direct result of the high values for α_0 at $800nm$ and the negatives values of n_2.

5 Self-assembled Gold nanospheres metasurfaces

5.1 Introduction

This chapter describes the results of the linear and nonlinear optical characterization of gold nanospheres metasurfaces. This work was did in colaboration with Jake Fontana et. al. and was published in the reference [17].

The prefix “meta” (μετα in Greek) means “beyond,” and in this sense, the name “metamaterials” signifies systems that are beyond conventional materials. The word “metamaterial” first appeared in literature in 2000 when Smith *et. al.* published their seminal paper on a structured material with simultaneously negative permeability and permittivity at microwave frequencies [70]. Metamaterial is a material engineered to have properties that are not found in nature, their properties derive not from the properties of the base materials, but from their newly designed structures. Shape, geometry, size, orientation, and arrangement gives them their smart properties capable of manipulating electromagnetic waves. The materials are usually arranged in repeat patterns, at scales that are smaller than the wavelengths of the incident electromagnetic fields.

Optical metamaterials are classified into two categories according with [71]:

1. *Metamolecules*, which are individual elements with inherent metamaterial properties and can be macroscopic in quantity.
2. *Metasurfaces,* which are thin, high-density, films of ordered plasmonic nanoparticles leading to novel optical, electronic and chemical properties.

For many applications, metasurfaces can be used in place of metamaterials. Metasurfaces have the advantage of taking up less physical space than full three-dimensional metamaterial structures; consequently, metasurfaces offer the possibility of less-lossy structures. Metasurfaces have a wide range of potential applications in electromagnetics (ranging from low microwave to optical frequencies). Some optical properties are: Negative, zero and large positive refractive índices, subwavelength resolution lenses and innovative waveplates. However, creating these metasurfaces efficiently, with nanoscopic scale feature resolution, uniformly over macroscopic scale areas, remains challenging. Moreover, measuring the optical response from these sub-wavelength thick metasurfaces is non-trivial and critical to enable the development of dispersion engineered coatings.

5.2 Self-assembly technique

Self-assembly is a process by which discrete components are driven to organize spontaneously into well-defined geometries by specific interactions. Self-assembly is typically associated with thermodynamic equilibrium, the organized structures being characterized by a minimum in the system's free energy. Essential in Self-assembly is that the building blocks organize into ordered, macroscopic structures, either through direct interactions (e.g., by interparticle forces), or indirectly using a template or an external field [72, 73]. There are differents forces, among these:

- Covalent bond
- Van der Waals
- Electrostatic
- Hydrogen bonding
- Hydrophobic
- Steric
- Magnetic force
- Electrical force

In this section we describe the method used by Jake Fontana and his team for the fabrication and linear characterization of the samples. In this case the metasurface assembly is based on a phase separation and surface tension gradient technique [74, 75].

This technique combines *(i)* the phase transfer of nanoparticles using a water miscible organic solvent, *(ii)* the self-assembly of nanoparticles into macroscopic (>cm), high-density, monolayer films using phase separation and *(iii)* the transport of the nanoparticle-ligand films onto non-functionalized substrates using surface tension gradients.

The $15.4 \pm 1.8nm$ diameter was determined through transmission electron microscopy (Figure 5.2.1) gold nanosphere suspension ($OD \sim 1$ in 1 cm) is placed into a 20 ml glass scintillation vial. A SiO_2 (Corning 1737) substrate, cleaned in potassium hydroxide dissolved in methanol at a concentration of 5% (w/v), was placed inside the vial containing the nanospheres. A 1-propanethiol solution (442 mM) was prepared in 1 ml tetrahydrofuran (THF). The 1 ml of the ligand solution in THF was then added into the vial containing the nanospheres and shaken for $15s$. The glass substrate was repositioned near vertical against the wall of the vial after shaking and the reaction mixture was pipetted onto the substrate, re-wetting the surface. The 1-propanethiol capped gold nanospheres phase separate from the fluid mixture to the air-fluid interface and are transported onto the wetted substrates via surface tension gradients creating macroscopic scale metasurface.

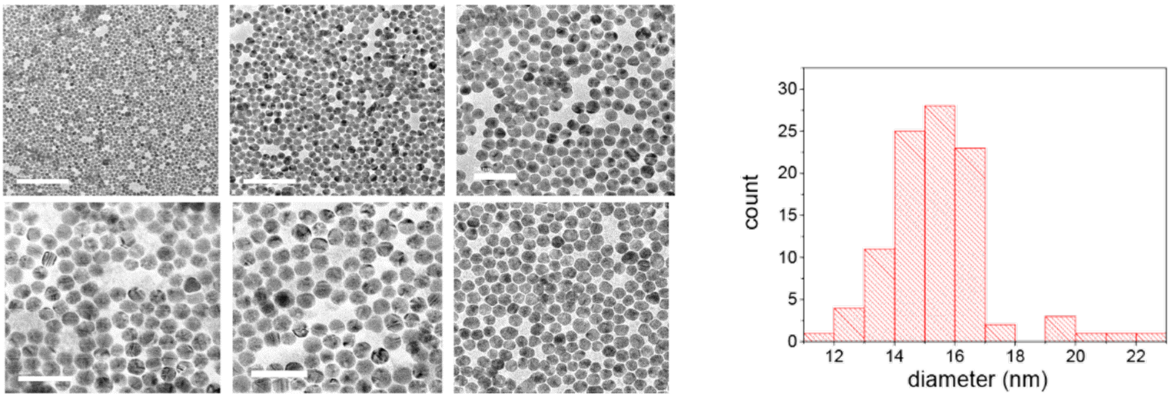

Figure 5.2.1: a) Representative transmission electron microscopy images of the metasurface. b) Gold nanospheres size distribution determined from the TEM images.

A schematic illustrating the metasurfaces consisting of a monolayer of gold nanospheres functionalized with ligand shells on a glass substrate is shown in Figure 5.2.2(a). Transmission electron microscopy (TEM) imaging (JEOL JEM-2200FS field emission electron microscope with $200kV$ accelerating voltage) of the metasurfaces were performed to examine the nanoscale organization of the nanospheres and determine the minimum interparticle distance. For such purposes, the metasurfaces were placed onto a holey carbon TEM grid by lifting the metasurface from the air-fluid interface during the self-assembly reaction. This created μm scale domains of quasi-hexagonally close packed monolayer metasurfaces, similar in local morphology to the glass substrates, but smallerrom the FFT analysis the center-to-center distance between the nanospheres was determined to be domain sizes. A representative TEM image of a metasurface is presented in Figure 5.2.2(b) showing a monolayer metasurface with local quasi-hexagonally close packing. From the TEM images the fast Fourier transform (FFT) was calculated using ImageJ (inset Figure 5.2.2(b)). FFT analysis can determine the crystalline structure and orientation of nanoparticles as well as the presence of any defects. From the FFT analysis the center-to-center distance between the nanospheres was determined to be $16.0 \pm 0.6nm$. The calculated particle diameter is $15.4nm$. Thus the gap between the particles is $0.6nm$. Figures 5.2.2(c) and 5.2.2(d) are images of a metasurface reflecting and transmitting white light, respectively, demonstrating surface areas on the centimeter size scale. The gold colored reflection in Figure 5.2.2(c) is a result from the large density of gold nanospheres. When backlit with white light and viewed in transmission, Figure 5.2.2(d), the spatially uniform blue color indicates that the plasmon resonances are well preserved, confirming the metasurfaces are a monolayer over the film area.

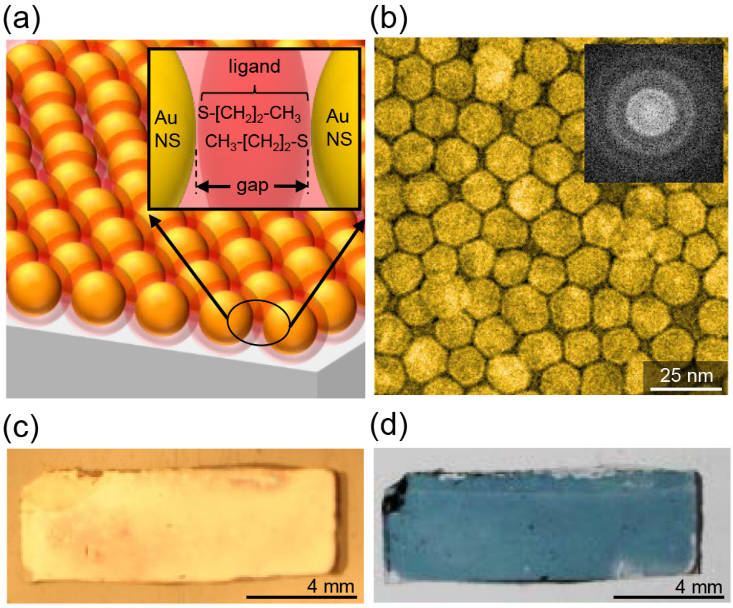

Figure 5.2.2: (a) Metasurface schematic consisting of a monolayer of gold nanospheres capped with ligand shells and supported by a glass substrate. (b) Representative false-colored TEM image of a metasurface composed of a monolayer gold nanospheres capped with 1-propanethiol shells on a holey carbon TEM substrate. The inset is a Fourier transform of a TEM metasurface image. Optical images of a metasurface on a glass substrate reflecting (c) and transmitting (d) light.

The n-alkanethiol ligand length, were n is the number of carbon atoms, and interparticle gap size are correlated in 5.2.3. The energy minimized ligand length, bound to gold, was determined using ACD/Chemsketch 2012 (solid black dots). The interparticle gap between close-packed gold nanospheres capped with n-alkanethiol shells has experimentally been shown to depend linearly on the length of the ligands, increasing at $0.12nm$ per n (solid red line) [76, 77]. A constant offset of $0.24nm$ accounts for the Au-S bond. The energy minimized ligand lengths and experimentally determined slope from literature are in good agreement, implying that the gap is set predominantly by the length of the ligand. Specifically for 1-propanethiol ($n = 3$) corresponds to an interparticle gap of $0.59nm$, in reasonable agreement with the experimental FFT results.

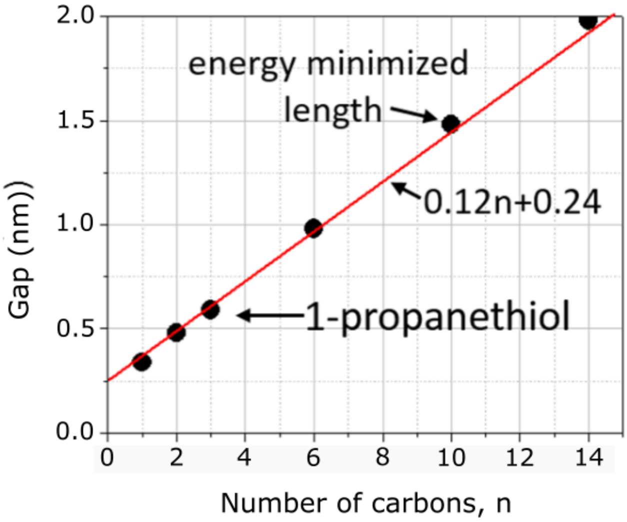

Figure 5.2.3: Correlation between the number of carbons in the n-alkanethiol ligands and the interparticle gap.

To further validate the interparticle gap three-dimensional finite element simulations were carried out using COMSOL Multiphysics 5.2. The metasurface was modeled as a hexagonal close-packed 15.4nm diameter gold nanosphere monolayer on a glass substrate ($n = 1.53$) with periodic boundary conditions. The refractive index of the gold was interpolated from literature [78]. Since excess ligands is deposited onto the film during the self-assembly process the nanospheres are fully coated with 1-propanethiol ($n = 1.44$). The model used unpolarized light to approximate the experimental conditions and the absorbance was calculated from the simulations. The absorbance from the metasurface was calculated as a function of interparticle gap from 2.0 to 0.2nm in 0.2nm intervals, Figure 5.2.4a). As the interparticle gap decreases the capacitance in between the nanospheres increases, resulting in the absorbance peak red-shifting from 629nm to 940nm for gaps 0.2nm to 2.0nm. By comparing the simulated and experimental absorbance peaks we can verify the interparticle gap. The experimental absorbance measurements from the metasurfaces were made using unpolarized white light incident perpendicular to the metasurfaces on SiO_2 substrates. The normalized experimental absorbance spectra from a metasurface is shown in Figure 5.2.4b) (blue points). The quality factor is defined by

$$Q = \frac{\lambda_0}{\delta\lambda_{FWHM}}, \tag{5.2.1}$$

where λ_0 is the absorbance peak wavelength and $\delta\lambda_{FWHM}$ is the full width at half maximum (FWHM) of the absorbance peak. The quality factor for experimental espectra is relatively large, $Q = 3.8$ indicating that the nanospheres are not aggregated (touching). The quality factor of the simulated spectrum is higher, $Q = 7.4$, than the experiments due to a prefect hexagonally close packed lattice. Yet, overall we observed a very good agreement between the simulated and experimental spectra demonstrating the metasurface are hexagonally close packed monolayer films of gold nanospheres capped with alkane ligands. Overlaying the absorbance spectra retrieved from the simulations, Figure 5.2.4b) (solid red line), with the experimental spectra we find good agreement with the experimental (753nm) and simulated (760nm) absorbance peak wavelength for a simulated interparticle gap of 0.6nm. We also find the shape of the spectra are similar with the experimental and simulated observation of a higher order mode at approximately 550nm. The simulations, energy minimization and FFT results all strongly indicate that the interparticle gap is predominantly set by the length of the ligand.

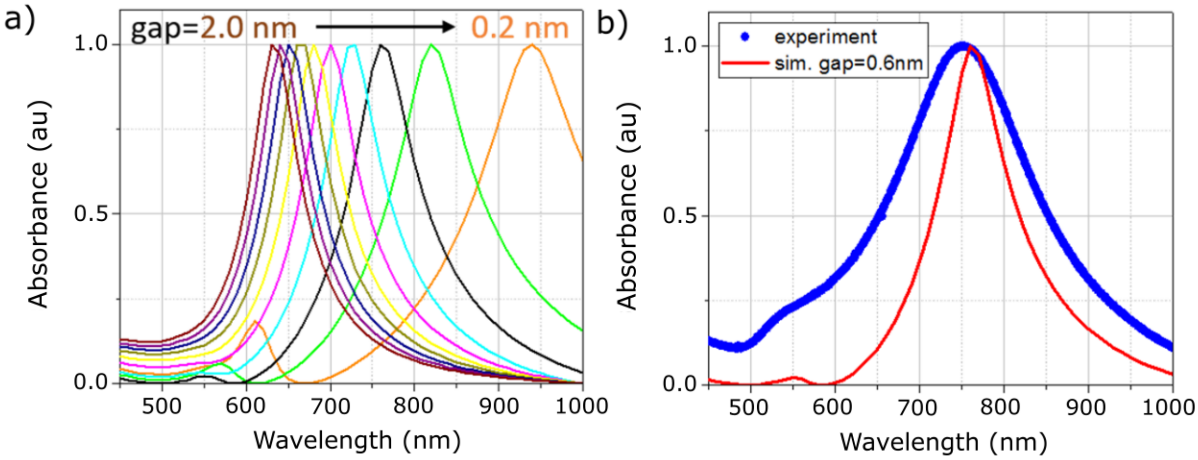

Figure 5.2.4: a) The simulated normalized absorbance peak wavelength shift of the metasurface as a function of interparticle gap from 2.0nm to 0.2nm in 0.2nm intervals. b) Comparing the normalized experimental (blue points) and simulated ($gap = 0.6nm$, solid red line) absorbance peaks of the metasurfaces.

To understand the response of the metasurface, relative to an isolated dimer, further simulations were undertaken. Figure 5.2.5 is the absorbance peak wavelength as a function of interparticle gap for the metasurface (red circles) and an isolated dimer (purple squares). Both were fit, and agree well, to the plasmon ruler equation [79] of the form,

$$\lambda = ae^{-(x/b)} + \lambda_0 \tag{5.2.2}$$

where $a = 571nm$, $b = 460nm$, $\lambda_0 = 0.550nm$ are for the metasurface (solid red line) and $a = 571nm$, $b = 245nm$, $\lambda_0 = 0.474nm$ are for the dimer (solid purple line). However, the absorbance peak wavelength from the metasurface is significantly more red-shifted (205nm at $gap = 0.2nm$) relative to the dimer, highlighting the importance of near-neighbor interactions to effectively enhance the capacitance (local electric field) in between the nanospheres in the metasurface [80]. These collective enhancements can be applied to create sensitive surface-enhanced Raman scattering sensors [74].

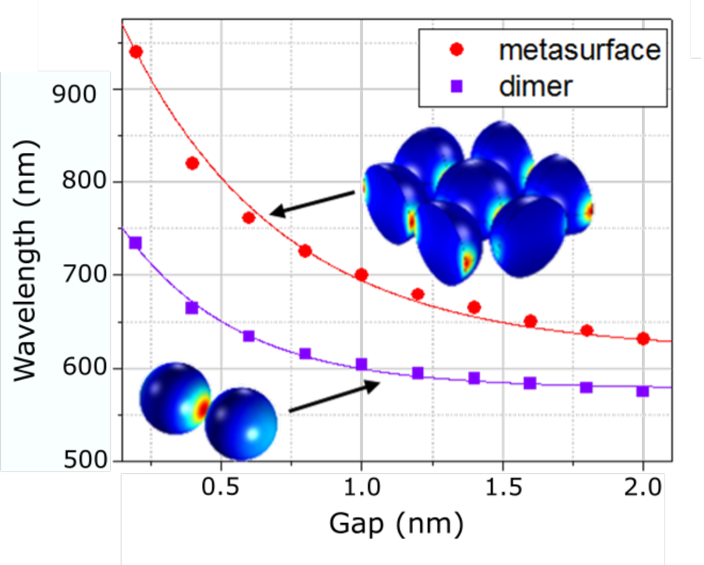

Figure 5.2.5: The shift in the absorbance peak wavelength of the metasurface (red dots) and an isolated dimer (purple squares) as a function of interparticle gap. The simulations fit for the metasurface (solid red line) and dimer (solid purple line).

5.3 Linear Optical Characterization

The linear refractive index of the metasurface was determined using spectroscopic ellipsometry (J.A. Woollam Co., V-VASE) by comparing the measured data and a model calculation. Ellipsometry measurements were performed off the air-nanosphere interface of the metasurface from $(400 - 1500)\,nm$ in $10nm$ steps at an angle of 60°. The probed area on the metasurface was approximately $7mm^2$. Scotch tape was used on the backside of the glass substrate to scatter and prevent any secondary reflections from the glass-air interface. Figure 5.3.1 shows the real and imaginary parts for 5 metasurfaces with the same characteristics. Was necessary to synthesized differents samples for the same gap $(0.6nm)$ for to guaranteed the uniformity, and reproducibility.

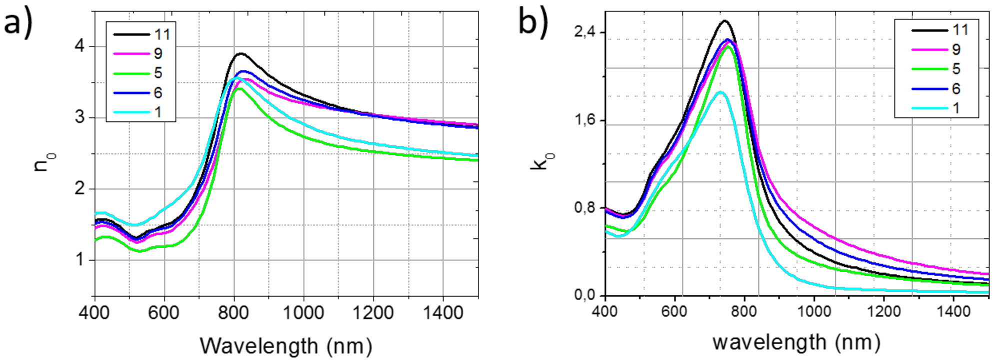

Figure 5.3.1: Real (a) and imaginary (b) parts of the linear index of refraction of the metasurfaces.

To retrieve the optical response of the metasurface a 3 layer model was used comprised of the glass substrate, gold nanospheres and an ambient layer. The metasurface layer was modeled as a homogenous layer since it is deeply sub-wavelength. The thickness of the metasurface layer was set at $16.6nm$ ($15.4nm$ diameter gold nanospheres and $1.2nm$ ligand layer). Figure 5.3.2(a-b) shows the experimental (blue solid line) and fitted (black dashed line) spectroscopic ellipsometry angles Ψ and Δ, averaged over five metasurface samples shown in the Figure 5.3.1.

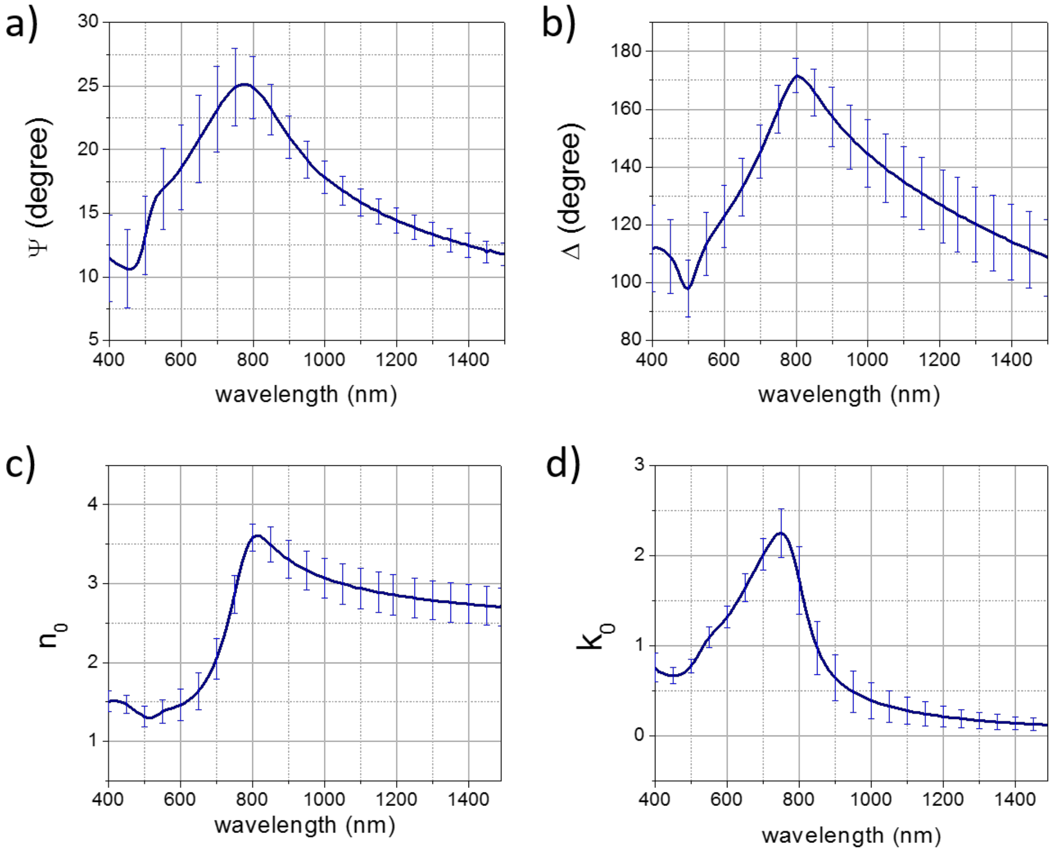

Figure 5.3.2: Spectroscopic ellipsometry data (solid blue lines) of Ψ (a) and Δ (b) averaged over five metasurface samples. The dashed black lines are the 3-layer model fitted to the experimental data. Real (c) and imaginary (d) parts of the linear index of refraction of the averaged metasurfaces obtained from the fits from (a-b).

The linear real and imaginary parts of the refractive index, n_0 and $k_0 = \lambda\beta_0/4\pi$, of the metasurface are shown in Figure 5.3.1. The average was do and is shown in the Figure 5.3.2(c-d). The real part of the linear refractive index shows a large dispersion ranging from values of 0.87 to 4.1. This indicates the metasurface has an optical response varying from less than vacuum to Germanium-like [23] within a spectral range of $280nm$, significantly larger than previous studies of self-assembled plasmonic nanospheres films [81, 82, 83, 24].

The absorption peak wavelength occurs at $749nm$, Figure 5.3.2d), in agreement with the spectroscopy data collected in Figure 5.2.4c). We find no evidence of a lower energy charge transfer plasmon mode, Figure 5.3.2d), at near infrared wavelengths and from Figure 5.2.4c) the absorbance peak wavelength is modeled well using a purely capacitive (insulating) $0.6nm$ gap. These results demonstrate that a classical description (without charge transfer) is appropriate to model these sub-nanometer gap metasurfaces, since ambiguities exists in the literature [84, 85, 86].

The figure of merit, that is the absolute maximum of the real to imaginary parts of the refractive index, is expected to be near unity for plasmonic metals at visible frequencies and indeed we find for these metasurfaces the average figure of merit is $|n_0^{max}| / |k_0^{max}| = 1.3$. The Figure of merit is shown in the 5.3.3. We can to observed very high values increasing quase-linearly since 800nm reaching values up to 22 in the near infrared. This is very important for applications suchs as al-optical switches.

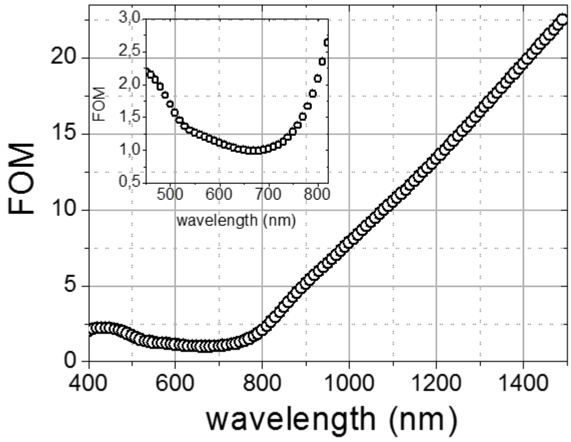

Figure 5.3.3: The average figure of merit. $FOM = |n_0/k_0|$. The inset in the figure is the FOM in the visible region.

5.4 Nonlinear Optical Characterization

To study the nonlinear optical behavior of the metasurfaces we employed the well-known Z-scan method [26, 27] described in the section 2.2.2. The optical source for the experiment was a Ti-sapphire regenerative amplifier operating at $800nm$ and a $1kHz$ repetition rate, with $100fs$ pulse duration. To calibrate the system a standard material, CS_2, with well-known nonlinear optical properties was used [26]. From the CS_2 measurements and an aperture corresponding to $S = 0.4$ in the Z-scan setup, the beam waist was determined to be $21\mu m$ at the focus, which was then used to calculate the intensities. Four metasurface samples were measured at three different lateral positions in each film. If the Z-scan measurements were repeated at fixed lateral position on the films, the results were constant (within the 5% of laser fluctuation), ensuring damage was not occurring due to the large laser intensities. Figure 5.4.1 shows the Z-scan signatures, averaged over the four samples, of the NLA and NLR. A blank SiO_2 substrate was first characterized, shown in Figure 5.4.1(a), even for high intensities no nonlinear signal was detected. Figure 5.4.1(b) is a typical signature for one of the metasurfaces at $10GW/cm^2$, showing saturated absorption and negative (self-defocusing) nonlinear refraction.

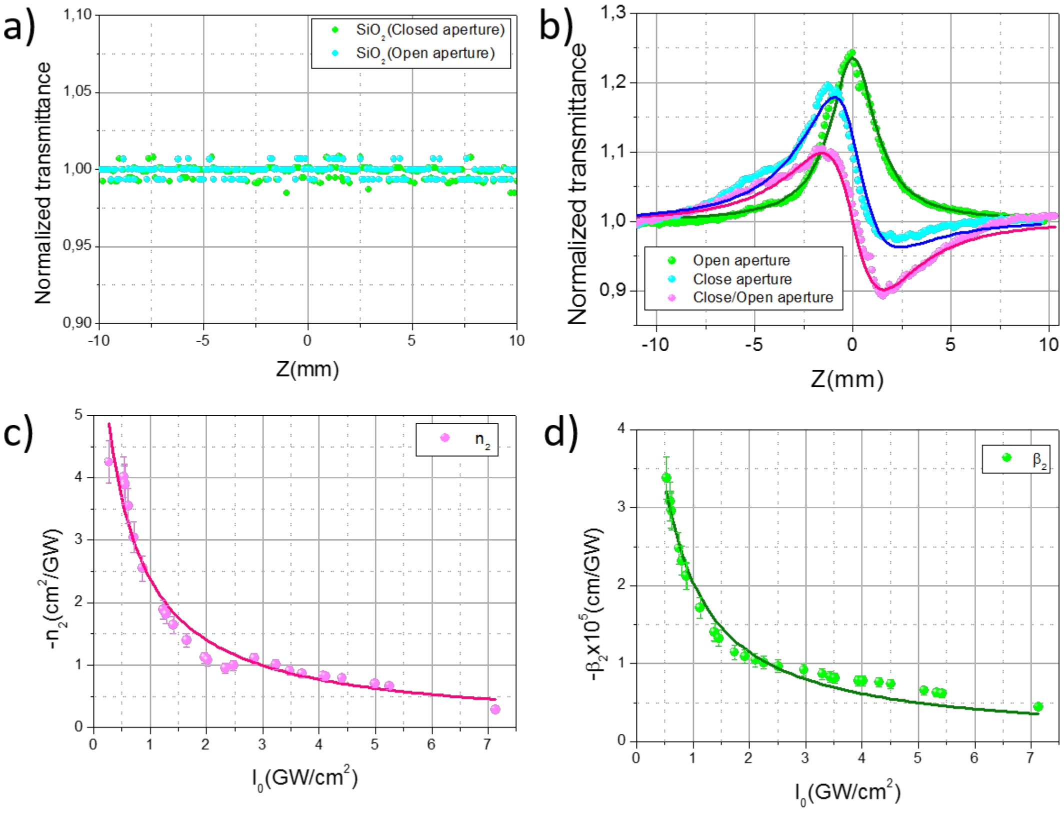

Figure 5.4.1: Average NLA and NLR measurements for (a) glass substrate at $I_0 = 5.87GW/cm^2$. (b) Gold metasurface Z-scan signature for open and closed aperture at $I_0 = 10GW/cm^2$. (c-d) experimentally determined average values of NLA and NLR coefficients for all samples, showing saturation behavior as a function of incident power density

Figures 5.4.1(c-d) show the intensity dependence for the NLA and NLR, where it can be readily observed that all samples present saturated absorption behavior, leading to saturation of the NLA as a function of incident intensity. The NLR also presented saturation of the nonlinearity as a function of incident intensity.

The saturation behavior for the NLA and NLR were fitted to $\beta_2 = \beta_{2sat}/(1 + I_0/I_{sat})$ and $n_2 = n_{2sat}/(1 + I_0/I_{sat})$, following [87, 55]. The saturated behavior of the NLA can be explained by the strong one-photon absorption arising from the plasmonic resonant excitation at $800nm$, close to the linear absorption peak at $753nm$ (see Figure 5.2.4b). As a consequence, it also leads to a saturation and negative sign for the NLR. Table 5.1 shows the values for n_2 and β_2 for the gold metasurfaces, compared with the data for other gold nanostructures [64, 88, 89], including periodically assembled gold nanofilms [90] and gold nanorods in thin PVA films [56, 15] To the best of our knowledge, a direct comparison with similar nanostructured metasurfaces cannot be made since it has not been studied before.

Ref	**Nanostructure type**	$\lambda_{\mathbf{pump}}$ **t**	***SPR***	$\mathbf{n_2(cm^2/W)}$	$\boldsymbol{\beta_2}\mathbf{(cm/W)}$
[17]	**Gold Metasurface**	**800nm** **100fs**	$\sim$ **753nm**	$\mathbf{-7.9\times10^{-9}}$	$\mathbf{-0.90\times10^{5}}$
[64]	*Gold thin film* (15nm)	800nm 100fs	$\sim 560nm$	-5.5×10^{-11}	$\sim 6.2\times10^{2}$
[88]	*Gold thin film* $(5-52)nm$	532nm 35fs	$\sim 550nm$	Not detected	$\sim 1.0\times10^{6}$
[89]	*Gold ultrathin films* (0.05nm)	532nm 30ps	$\sim 550nm$	Not detected	$\sim 5\times10^{6}$
[90]	*Gold thin film periodically organized* (14nm)	532nm 25ps	$\sim 600nm$	$-2.89\times10^{-10}/n_0^2$	$-7.6\times10^{1}/n_0^2$
[56]	*Gold nanorods in electrospun films*	800nm 100fs	$500nm\ \parallel$ $820nm\ \perp$	$3.5\times10^{-12}\ \parallel$ $26\times10^{-12}\ \perp$	Not studied
[15]	*Gold nanorods in PVA stretched films*	800nm 100fs	$530nm\ \parallel$ $670nm\ \perp$	$1.4\times10^{-11}\ \parallel$ $6.0\times10^{-11}\ \perp$	$1\times10^{3}-1.02\times10^{5}$

Table 5.1: Comparison of NLR and NLA absorption in gold nanostructured materials.

In [64], Au thin films were deposited on glass (soda-lime) substrates and annealed to form Au nanoparticles on the surface of the glass. Optical nonlinear properties were studied, before and after annealing, as a function of the thickness of the deposited film (before annealing) and of the height of the NPs (after annealing). For the nonlinear characterization was used TM-EZ scan technique at 800nm and 150fs before and after annealing. Results showed that n_2 and α_2 at 800nm undergo a sign change after the annealing process for the 15 nm deposited film. On the other hand, the 15 nm deposited film does not present a surface plasmon signal before annealing; rather, its absorbance spectra resembles the extinction spectra for bulk Au. With the annealing, large Au NPs are formed and the absorbance spectra presents a SPR peak at 560 nm, leading to an increase of n_2.

In [90], well-ordered 2-D gold nanoparticle arrays were fabricated using nanosphere lithography. The nonlinear optical properties of the nanoparticle arrays were investigated using the z-scan technique at 532nm with 25ps pulses. The FOM of the nanoparticle arrays is about one order of magnitude larger than that of the ultra-thin gold film consisting of randomly distributed spheroidal clusters. The enhancement of the optical nonlinearity could be due to the strong local field near the triangular nanoparticles. It is worth noting that, in well-ordered nanoparticle arrays, the homogeneity in size, shape, and distribution of the nanoparticles make it possible to get a better understanding of the origin of the

enhancement of the nonlinearity, and then to further optimize the value of the FOM.
In a recent report, Boyd and co-workers [91] reviewed the third order optical nonlinearity of several gold based nanostructures, and pointed out the differences in measured nonlinear optical coefficients, both NLR and NLA, with respect to the experimental conditions (pump wavelength, pulse duration, technique employed). In their literature survey, NLR values ranged from $\sim 10^{-8} cm^2/W$ to $\backsim 10^{-12} cm^2/W$ and NLA ranged from $10^3 cm/GW$ to $10^6 cm/GW$, with pulse durations ranging from $100fs$ to $750ps$. If we consider the $100fs$ pump pulse regime, whereby interband ($5d$–$6sp$) and hot electron contribution should be taken into account [91], the values of the NLR obtained in our work are two orders of magnitude larger than in other gold nanostructured materials studied at the same pump pulse duration regime. For the NLA, the values are the same order of magnitude, of course, the pump wavelength with respect to the plasmonic peak absorption wavelength plays an important role.

5.5 Conclusions

In summary, we have described the preparation, morphology, linear and nonlinear optical characterization of metasurfaces consisting of a quasi-hexagonally close packed monolayer of gold nanospheres capped with alkanethiol ligands on glass substrates. We show the interparticle gap is predominantly set by the length of the ligand, and demonstrate that a classical description is sufficient to model these sub-nanometer gap metasurfaces. These nanoengineered metasurfaces have a linear refractive index, determined using ellipsometry, ranging from $n_0 = 0.87 - 4.1$ between $600nm$ and $800nm$, which opens up many possibilities for basic and applied studies in a single material. Nonlinear optical characterization was also carried out, and the results were compared to other gold based nanostructures. A significant point of our nonlinear results compared to literature, with respect to the same pump pulse time scale, is that the negative (self-defocusing) NLR in our metasurface is at least two orders of magnitude higher (at saturation intensity), whereas the saturated NLA is of the same order as other gold nanostructures (see table 5.1). By controlling the pump duration and wavelength parameter space, and taking into account the dynamics of gold excitations, the nonlinearities can be managed and properly exploited for photonics applications.

6 Conclusions and future work

Gold nanostructures have been studied during decades. The behavior of the optical properties corresponds to different physical process depending on the shape, size, geometry, thickness, arrangement, methods of the synthesizing, among others. There are review articles demonstrating the challenges for understanding the behavior of the linear and nonlinear properties of metals. In this thesis, we studied nanomaterials based on Gold.

The anisotropy in the optical properties of the Gold nanorod cluster-PVA was studied in a separate experiment. Uniaxial alignment was obtained by mechanically stretching the PVA-based films. Using TEM and SAXS we could quantify the alignment of the clusters NRs. NLO was studied at $800nm$, $100fs$ and $20Hz$ (the low repetition rate was used to avoid damage in the samples) and we discovered that the local field in the clusters leads to enhancement of the NL properties. An interesting feature is a change in the sign of the nonlinearity from the polarization excitation parallel to the LSPR compared to excitation of the TSPR. Saturation of the NLA was observed for randomly and parallel to the alignment direction with an enhancement of 57 times and zero values for the polarization excitation parallel to TSPR demonstrating again the anisotropy of the material.

In another study, measurements in AuNR in Cargille oil under applied electric field demonstrated the influence of the linear absorption in the NLO properties. For NLR was used two techniques: Z-scan and Beam collimated Hartmann-Shack. We find self-defocusing and increasing in the values of the NLR with the application of the electric field (i.e. decreasing the LSPR). We find a good agreement the results obtained by using both techniques. When we did the NLA measurements for $76MHz$, whereby thermal effects dominate, we find a positive NLA which is associated to two-photon absorption, but in reality, this positive value is due to the high linear absorption at $800nm$ combined with negatives values of n_2.

We studied metasurfaces with a refractive index ranging from $n_0 = 0.87 - 4.1$ between $600nm$ and $800nm$. These metasurfaces were fabricated by the self-assembly methods and provided uniforms samples, with a sub-nanometer interparticle gap and large area (few centimeters). For the nonlinear characterization it demonstrated that the metasurfaces have a saturated self-defocusing NLR saturated two orders of magnitude higher when compared with another Gold-nanostructures and saturation of the NLA due to the high values of the α_0 at $800nm$.

As for future work, we want to extend the research of the NL responses of the metasurfaces in a broadband in wavelength – towards the optical communication region - using a white-light Z-scan and observing the nonlinear optical response dependence of the refraction index. The linear FOM for this material showed high values ~ 22, making it promising for applications such as all-optical switches. Furthermore, we want to explore the action of the random laser of the metasurfaces doping with dyes.

Regarding the GNR in PVA, we plan to explore the enhancement of the local field of the clusters of NRs experimentally in PVA using microscopy techniques.

A new cuvette will be designed to explore the dependence of the polarization of the incident light with the electric field applied to AuNRs in colloids to extend the linear and nonlinear characterization of this samples.

References

[1] Mark I. Stockman. Nanoplasmonics: past, present, and glimpse into future. *Opt. Express*, 19(22):22029–22106, Oct 2011. 16, 45

[2] Prasad P. N. *Nanophotonics*. Wiley, New York, 2004. 16, 45

[3] Martti Kauranen and Anatoly V. Zayats. Nonlinear plasmonics. *Nat Photon*, 6(11):737–748, November 2012. 16, 45

[4] Jiafang Li, Honglian Guo, and Zhi-Yuan Li. Microscopic and macroscopic manipulation of gold nanorod and its hybrid nanostructures. *Photon. Res.*, 1(1):28–41, Jun 2013. 16

[5] Stephan Link and Mostafa A. El-Sayed. Spectral properties and relaxation dynamics of surface plasmon electronic oscillations in gold and silver nanodots and nanorods. *The Journal of Physical Chemistry B*, 103(40):8410–8426, 1999. 18

[6] Stefan Stoenescu, Vo-Van Truong, and Muthukumaran Packirisamy. Dichroic optical properties of uniaxially oriented gold nanorods in polymer films. *Plasmonics*, 9(2):299–307, 2014. 18, 19

[7] Aneta J. Mieszawska, Grzegorz W. Slawinski, and Francis P. Zamborini. Directing the growth of highly aligned gold nanorods through a surface chemical amidation reaction. *Journal of the American Chemical Society*, 128(17):5622–5623, 2006. PMID: 16637614. 18

[8] Jorge Pérez-Juste, Isabel Pastoriza-Santos, Luis M. Liz-Marzán, and Paul Mulvaney. Gold nanorods: Synthesis, characterization and applications. *Coordination Chemistry Reviews*, 249(17):1870 – 1901, 2005. 36th International Conference on Coordination Chemistry, Merida, Mexico, July 2004. 18, 19

[9] Bianca M. I. van der Zande, Laurent Pages, Rifat A. M. Hikmet, and Alfons van Blaaderen. Optical properties of aligned rod-shaped gold particles dispersed in poly(vinyl alcohol) films. *The Journal of Physical Chemistry B*, 103(28):5761–5767, 1999. 18, 46

[10] Wenshan Cai and Vladimir Shalaev. *Optical Metamaterials: Fundamentals and Applications.* Springer. 19

[11] Yongmin Liu and Xiang Zhang. Metamaterials: a new frontier of science and technology. *Chem. Soc. Rev.*, 40:2494–2507, 2011. 19

[12] Jeffrey N. Anker, W. Paige Hall, Olga Lyandres, Nilam C. Shah, Jing Zhao, and Richard P. Van Duyne. Biosensing with plasmonic nanosensors. *Nat Mater*, 7(6):442–453, Jun 2008. 19

[13] Xiang Zhang; Zhaowei Liu. Superlenses to overcome the diffraction limit. *Nature Materials*, 7:435–441, 2008. 19

[14] Dmitri K. Gramotnev and Sergey I. Bozhevolnyi. Plasmonics beyond the diffraction limit. *Nature Photonics*, 4:83–91, 2010. 19

[15] Melissa Maldonado, H. T. M. C. M. Baltar, Anderson S. L. Gomes, R. Vaia, K. Park, J. Che, M. Hsiao, Cid B. de Araújo, A. Baev, and P. N. Prasad. Coupled-plasmon induced optical nonlinearities in anisotropic arrays of gold nanorod clusters supported in a polymeric film. *Journal of Applied Physics*, 121(14):143103, 2017. 19, 45, 47, 48, 49, 50, 55, 56, 57, 58, 59, 61, 62, 86

[16] Leonardo Menezes, M. Maldonado, L. Araujo, G. K. B. da Costa, J. Fontana, I. C. Carvalho, and A. S. L. Gomes. Nonlinear refractive index of electric field-oriented au nanorods. *CLEO Europe*, CE-8.4 TUE (Oral presentation):221, 2017. 19

[17] Jake Fontana, Melissa Maldonado, Nicholas Charipar, Scott A. Trammell, Rafaela Nita, Jawad Naciri, Alberto Pique, Banahalli Ratna, and Anderson S. L. Gomes. Linear and nonlinear optical characterization of self-assembled, large-area gold nanosphere metasurfaces with sub-nanometer gaps. *Opt. Express*, 24(24):27360–27370, Nov 2016. 19, 76, 86

[18] Fournet G. Guinier A. *Small-Angle sccatering of X-rays.* London:Wiley, 1955. 20, 22

[19] J. S. Higgins and R. S. Stein. Recent developments in polymer applications of small-angle neutron, x-ray and light scattering. *Journal of Applied Crystallography*, 11(5):346–375, Oct 1978. 20, 22

[20] Benjamin Chu and Tianbo Liu. Characterization of nanoparticles by scattering techniques. *Journal of Nanoparticle Research*, 2(1):29–41, 2000. 20, 22

[21] A. Prasad, R. Shroff, S. Rane, and G. Beaucage. Morphological study of hdpe blown films by saxs, sem and tem: a relationship between the melt elasticity parameter and lamellae orientation. *Polymer*, 42(7):3103 – 3113, 2001. 20, 22

[22] H. G. Tompkins. *A user's guide to ellipsometry.* Academic Press, 1993. 20

[23] G.E. Jellison Jr. Optical functions of gaas, gap, and ge determined by two-channel polarization modulation ellipsometry. *Optical Materials*, 1(3):151 – 160, 1992. 20, 83

[24] H.-L. Zhang, S.D. Evans, and J.R. Henderson. Spectroscopic ellipsometric evaluation of gold nanoparticle thin films fabricated using layer-by-layer self-assembly. *Advanced Materials*, 15(6):531–534, 2003. 20, 83

[25] J.A. Wollan Co. *Tutorial: introduction to ellipsometry.* 20, 24, 25, 26

[26] Cid B de Araújo, Anderson S L Gomes, and Georges Boudebs. Techniques for nonlinear optical characterization of materials: a review. *Reports on Progress in Physics*, 79(3):036401, 2016. 20, 29, 33, 35, 36, 84

[27] M. Sheik-Bahae, A. A. Said, T. H. Wei, D. J. Hagan, and E. W. Van Stryland. Sensitive measurement of optical nonlinearities using a single beam. *IEEE Journal of Quantum Electronics*, 26(4):760–769, Apr 1990. 20, 84

[28] Manuel R. Ferdinandus, Matthew Reichert, Trenton R. Ensley, Honghua Hu, Dmitry A. Fishman, Scott Webster, David J. Hagan, and Eric W. Van Stryland. Dual-arm z-scan technique to extract dilute solute nonlinearities from solution measurements. *Opt. Mater. Express*, 2(12):1776–1790, Dec 2012. 20, 34

[29] Andrea Gnoli, Luca Razzari, and Marcofabio Righini. Z-scan measurements using high repetition rate lasers: how to manage thermal effects. *Opt. Express*, 13(20):7976–7981, Oct 2005. 20, 35, 36

[30] D. Rativa, R. E. de Araujo, A. S. L. Gomes, and B. Vohnsen. Hartmann-shack wavefront sensing for nonlinear materials characterization. *Opt. Express*, 17(24):22047–22053, Nov 2009. 20, 36, 43

[31] R. W. Carpenter, J. Bentley, and E. A. Kenik. Small-angle electron scattering in the transmission electron microscope. *Journal of Applied Crystallography*, 11(5):564–568, Oct 1978. 22

[32] P.P. Kane, G. Basavaraju, J. Mahajani, and A.K. Priyadarsini. Elastic and compton scattering of 1.17 and 1.33 mev gamma rays through small angles. *Nuclear Instruments and Methods*, 155(3):467 – 474, 1978. 22

[33] Brian Richard Pauw. Everything saxs: small-angle scattering pattern collection and correction. *Journal of Physics: Condensed Matter*, 25(38):383201, 2013. 22

[34] Nobutami Kasai Masao Kakudo. *X-ray diffraction by polymers.* New York: Elsevier, 1992. 22

[35] R. J. Samuels. *Structured polymer properties.* Wiley, 1974. 23

[36] Hilmar Koerner, Weidong Liu, Max Alexander, Peter Mirau, Heather Dowty, and Richard A. Vaia. Deformation-morphology correlations in electrically conductive carbon nanotube- thermoplastic polyurethane nanocomposites. *Polymer*, 46(12):4405 – 4420, 2005. In Honor of James E. Mark. 24, 49

[37] N. Bloembergen. *Nonlinear Optics: A Lecture Note And Reprint Volume Frontiers in Physics Series.* 1965. 29

[38] A. S. L. Gomes, E. L. Falc ao Filho, Cid B. de Araújo, Diego Rativa, and R. E. de Araujo. Thermally managed eclipse z-scan. *Opt. Express*, 15(4):1712–1717, Feb 2007. 35, 36, 43, 44

[39] Sumit Singhal, Sirshendu Dinda, and Debabrata Goswami. Measurement of pure optical nonlinearity in carbon disulfide with a high-repetition-rate femtosecond laser. *Appl. Opt.*, 56(3):644–648, Jan 2017. 36

[40] K Creath JC Wyant. Basic wavefront aberration theory for optical metrology. *Applied optics and optical engineering*, 1992. 38, 39

[41] THORLABS. *WFS Series Operation Manual*, OCTOBER 2015. 39, 40

[42] Thorlabs. Hs tutorial. 39, 40

[43] Vasudevan Lakshminarayanan and Andre Fleck. Zernike polynomials: A guide. 58:1678–1678, 04 2011. 40, 41, 42

[44] Suchita A. Kalele, Neha R. Tiwari, Suresh W. Gosavi, and Sulabha K. Kulkarni. Plasmon-assisted photonics at the nanoscale. *Journal of Nanophotonics*, 1(1):012501–012501–20, 2007. 45

[45] Zhe Kang, Xingyuan Guo, Zhixu Jia, Yang Xu, Lai Liu, Dan Zhao, Guanshi Qin, and Weiping Qin. Gold nanorods as saturable absorbers for all-fiber passively q-switched erbium-doped fiber laser. *Opt. Mater. Express*, 3(11):1986–1991, Nov 2013. 45

[46] Wing-Cheung Law, Ken-Tye Yong, Alexander Baev, and Paras N. Prasad. Sensitivity improved surface plasmon resonance biosensor for cancer biomarker detection based on plasmonic enhancement. *ACS Nano*, 5(6):4858–4864, 2011. PMID: 21510685. 45

[47] Xin Liu and Dang Yuan Lei. Simultaneous excitation and emission enhancements in upconversion luminescence using plasmonic double-resonant gold nanorods. *Scientific Reports*, 5:15235–, October 2015. 45

[48] Jiafang Li, Siyun Liu, Ye Liu, Fei Zhou, and Zhi-Yuan Li. Anisotropic and enhanced absorptive nonlinearities in a macroscopic film induced by aligned gold nanorods. *Applied Physics Letters*, 96(26), 2010. 45, 50, 51

[49] Kyoungweon Park, Hilmar Koerner, and Richard A. Vaia. Depletion-induced shape and size selection of gold nanoparticles. *Nano Letters*, 10(4):1433–1439, 2010. PMID: 20349972. 45

[50] Kyoungweon Park, Sushmita Biswas, Sushil Kanel, Dhriti Nepal, and Richard A. Vaia. Engineering the optical properties of gold nanorods: Independent tuning of surface plasmon energy, extinction coefficient, and scattering cross section. *The Journal of Physical Chemistry C*, 118(11):5918–5926, 2014. 46

[51] S. Sinha-Ray, K. Fezzaa, and A. L. Yarin. The internal structure of suspensions in uniaxial elongation. *Journal of Applied Physics*, 113(4), 2013. 49

[52] Joanna Olesiak-Banska, Marta Gordel, Radoslaw Kolkowski, Katarzyna Matczyszyn, and Marek Samoc. Third-order nonlinear optical properties of colloidal gold nanorods. *The Journal of Physical Chemistry C*, 116(25):13731–13737, 2012. 50, 54, 61

[53] E. L. Falcão-Filho, Cid B. de Araújo, and Jr. J. J. Rodrigues. High-order nonlinearities of aqueous colloids containing silver nanoparticles. *J. Opt. Soc. Am. B*, 24(12):2948–2956, Dec 2007. 53

[54] Diego Rativa, R. E. de Araujo, and A. S. L. Gomes. One photon nonresonant high-order nonlinear optical properties of silver nanoparticles in aqueous solution. *Opt. Express*, 16(23):19244–19252, Nov 2008. 53

[55] Jean-Louis Coutaz and Martin Kull. Saturation of the nonlinear index of refraction in semiconductor-doped glass. *J. Opt. Soc. Am. B*, 8(1):95–98, Jan 1991. 54, 85

[56] Hang Zhang, Zhongliang Hu, Zhijun Ma, Mindaugas GeceviÄ?ius, Guoping Dong, Shifeng Zhou, and Jianrong Qiu. Anisotropically enhanced nonlinear optical properties of ensembles of gold nanorods electrospun in polymer nanofiber film. *ACS Applied Materials & Interfaces*, 8(3):2048–2053, 2016. PMID: 26731010. 54, 61, 62, 86

[57] P. G. Etchegoin, E. C. Le Ru, and M. Meyer. Erratum: An analytic model for the optical properties of gold. *The Journal of Chemical Physics*, 127(18), 2007. 55

[58] Prashant K. Jain, Susie Eustis, and Mostafa A. El-Sayed. Plasmon coupling in nanorod assemblies: Optical absorption, discrete dipole approximation simulation,

and exciton-coupling model. *The Journal of Physical Chemistry B*, 110(37):18243–18253, 2006. PMID: 16970442. 58

[59] Alison M. Funston, Carolina Novo, Tim J. Davis, and Paul Mulvaney. Plasmon coupling of gold nanorods at short distances and in different geometries. *Nano Letters*, 9(4):1651–1658, 2009. PMID: 19271775. 58

[60] Hendry I. Elim, Jian Yang, Jim-Yang Lee, Jun Mi, and Wei Ji. Observation of saturable and reverse-saturable absorption at longitudinal surface plasmon resonance in gold nanorods. *Applied Physics Letters*, 88(8), 2006. 61

[61] H. Baida, D. Mongin, D. Christofilos, G. Bachelier, A. Crut, P. Maioli, N. Del Fatti, and F. Vallée. Ultrafast nonlinear optical response of a single gold nanorod near its surface plasmon resonance. *Phys. Rev. Lett.*, 107:057402, Jul 2011. 61

[62] Yushi Tsutsui, Tomokatsu Hayakawa, Go Kawamura, and Masayuki Nogami. Tuned longitudinal surface plasmon resonance and third-order nonlinear optical properties of gold nanorods. *Nanotechnology*, 22(27):275203, 2011. 61, 62

[63] Lazaro A. Padilha, Jake Fontana, Dana Kohlgraf-Owens, Michele Moreira, Scott Webster, Peter Palffy-Muhoray, Pieter G. Kik, David J. Hagan, and Eric W. Van Stryland. Linear and nonlinear optical response of aligned gold nanorods. In *Conference on Lasers and Electro-Optics/International Quantum Electronics Conference*, page JTuD123. Optical Society of America, 2009. 61, 62, 67

[64] E. C. Romani, Douglas Vitoreti, Paula M. P. Gouvêa, P. G. Caldas, R. Prioli, S. Paciornik, Michael Fokine, Arthur M. B. Braga, Anderson S. L. Gomes, and Isabel C. S. Carvalho. Gold nanoparticles on the surface of soda-lime glass: morphological, linear and nonlinear optical characterization. *Opt. Express*, 20(5):5429–5439, Feb 2012. 62, 85, 86

[65] Gong Hong-Mei, Zhou Zhang-Kai, Xiao Si, Song Hao, Su Xiong-Rui, Li Min, and Wang Qu-Quan. Intensity-dependent optical nonlinear absorption and refraction of gold nanorods. *Chinese Physics Letters*, 24(12):3443, 2007. 62

[66] Bianca M. I. van der Zande, Ger J. M. Koper, and Henk N. W. Lekkerkerker. Alignment of rod-shaped gold particles by electric fields. *The Journal of Physical Chemistry B*, 103(28):5754–5760, 1999. 64

[67] Jake Fontana, Greice K. B. da Costa, Joao M. Pereira, Jawad Naciri, Banahalli R. Ratna, Peter Palffy-Muhoray, and Isabel C. S. Carvalho. Electric field induced orientational order of gold nanorods in dilute organic suspensions. *Applied Physics Letters*, 108(8):081904, 2016. 66

[68] Donglin Xie, Marco Lista, Greg G. Qiao, and Dave E. Dunstan. Shear induced alignment of low aspect ratio gold nanorods in newtonian fluids. *The Journal of Physical Chemistry Letters*, 6(19):3815–3820, 2015. PMID: 26722876. 66

[69] Raúl del Coso and Javier Solis. Relation between nonlinear refractive index and third-order susceptibility in absorbing media. *J. Opt. Soc. Am. B*, 21(3):640–644, Mar 2004. 73, 74, 75

[70] C. L. Holloway, E. F. Kuester, J. A. Gordon, J. O'Hara, J. Booth, and D. R. Smith. An overview of the theory and applications of metasurfaces: The two-dimensional equivalents of metamaterials. *IEEE Antennas and Propagation Magazine*, 54(2):10–35, April 2012. 76

[71] Jake Fontana and Banahalli R. Ratna. Toward high throughput optical metamaterial assemblies. *Appl. Opt.*, 54(31):F61–F69, Nov 2015. 76

[72] Marek Grzelczak, Jan Vermant, Eric M. Furst, and Luis M. Liz-MarzÃ¡n. Directed self-assembly of nanoparticles. *ACS Nano*, 4(7):3591–3605, 2010. PMID: 20568710. 77

[73] Rajagopalan Thiruvengadathan, Venumadhav Korampally, Arkasubhra Ghosh, Nripen Chanda, Keshab Gangopadhyay, and Shubhra Gangopadhyay. Nanomaterial processing using self-assembly-bottom-up chemical and biological approaches. *Reports on Progress in Physics*, 76(6):066501, 2013. 77

[74] Jake Fontana, John Livenere, Francisco J. Bezares, Joshua D. Caldwell, Ronald Rendell, and Banahalli R. Ratna. Large surface-enhanced raman scattering from self-assembled gold nanosphere monolayers. *Applied Physics Letters*, 102(20):201606, 2013. 77, 81

[75] Jake Fontana, Jawad Naciri, Ronald Rendell, and Banahalli R. Ratna. Macroscopic self-assembly and optical characterization of nanoparticle ligand-metamaterials. *Advanced Optical Materials*, 1(1):100–106, 2013. 77

[76] J. Christopher Love, Lara A. Estroff, Jennah K. Kriebel, Ralph G. Nuzzo, and George M. Whitesides. Self-assembled monolayers of thiolates on metals as a form of nanotechnology. *Chemical Reviews*, 105(4):1103–1170, 2005. PMID: 15826011. 79

[77] James E. Martin, Jess P. Wilcoxon, Judy Odinek, and Paula Provencio. Control of the interparticle spacing in gold nanoparticle superlattices. *The Journal of Physical Chemistry B*, 104(40):9475–9486, 2000. 79

[78] E. D. Palik. *Handbook of Optical Constants of Solids*. Elsevier Science, 1985. 80

[79] Ryan T. Hill, Jack J. Mock, Angus Hucknall, Scott D. Wolter, Nan M. Jokerst, David R. Smith, and Ashutosh Chilkoti. Plasmon ruler with angstrom length resolution. *ACS Nano*, 6(10):9237–9246, 2012. PMID: 22966857. 81

[80] Siyu Tan, Fengping Yan, Leena Singh, Wei Cao, Ningning Xu, Xiang Hu, Ranjan Singh, Mingwei Wang, and Weili Zhang. Terahertz metasurfaces with a high refractive index enhanced by the strong nearest neighbor coupling. *Opt. Express*, 23(22):29222–29230, Nov 2015. 81

[81] Hsuen-Li Chen, Hsu-Chun Cheng, Tsung-Shine Ko, Shang-Yu Chuang, and Tien-Chi Chu. Characterizing optical properties of self-assembled gold nanoparticles for surface plasmon resonance device applications. *Japanese Journal of Applied Physics*, 45(9R):6984, 2006. 83

[82] Dehui Wan, Hsuen-Li Chen, Yu-Syuan Lin, Shang-Yu Chuang, Jiann Shieh, and Szu-Hung Chen. Using spectroscopic ellipsometry to characterize and apply the optical constants of hollow gold nanoparticles. *ACS Nano*, 3(4):960–970, 2009. PMID: 19290613. 83

[83] Da-Shin Wang and Chii-Wann Lin. Density-dependent optical response of gold nanoparticle monolayers on silicon substrates. *Opt. Lett.*, 32(15):2128–2130, Aug 2007. 83

[84] Hoon Cha, Jun Hee Yoon, and Sangwoon Yoon. Probing quantum plasmon coupling using gold nanoparticle dimers with tunable interparticle distances down to the subnanometer range. *ACS Nano*, 8(8):8554–8563, 2014. PMID: 25089844. 84

[85] Dario Knebl, Anton Hörl, Andreas Trügler, Johannes Kern, Joachim R. Krenn, Peter Puschnig, and Ulrich Hohenester. Gap plasmonics of silver nanocube dimers. *Phys. Rev. B*, 93:081405, Feb 2016. 84

[86] Shu Fen Tan, Lin Wu, Joel K.W. Yang, Ping Bai, Michel Bosman, and Christian A. Nijhuis. Quantum plasmon resonances controlled by molecular tunnel junctions. *Science*, 343(6178):1496–1499, 2014. 84

[87] Leonardo De Boni, Erin Leigh Wood, Carlos Toro, and Florencio E. Hernandez. Optical saturable absorption in gold nanoparticles. *Plasmonics*, 3(4):171, 2008. 85

[88] E. Xenogiannopoulou, P. Aloukos, S. Couris, E. Kaminska, A. Piotrowska, and E. Dynowska. Third-order nonlinear optical properties of thin sputtered gold films. *Optics Communications*, 275(1):217 – 222, 2007. 85, 86

[89] David D. Smith, Youngkwon Yoon, Robert W. Boyd, Joseph K. Campbell, Lane A. Baker, Richard M. Crooks, and Michael George. z-scan measurement of the nonlinear

absorption of a thin gold film. *Journal of Applied Physics*, 86(11):6200–6205, 1999. 85, 86

[90] Hong Shen, Bolin Cheng, Guowei Lu, Tingyin Ning, Dongyi Guan, Yueliang Zhou, and Zhenghao Chen. Enhancement of optical nonlinearity in periodic gold nanoparticle arrays. *Nanotechnology*, 17(16):4274, 2006. 85, 86

[91] Robert W. Boyd, Zhimin Shi, and Israel De Leon. The third-order nonlinear optical susceptibility of gold. *Optics Communications*, 326:74 – 79, 2014. 87

A Hartmann- Shack Wavefront Sensor

A Thorlabs wavefront (Shack-Hartmann) sensor is comprised oif a camera with a microlens array (MLA) mounted in front of the camera sensor. Two types of wavefront sensors are available with different camera sensors and performance:

- WFS150/300 Series, based on a CCD camera
- WFS20 Series, based on a high resolution CMOS camera head with external control box that allows a remarkably higher measurement speed at an improved measurement accuracy.

WFS150-5C uses a MLA with a chrome mask on it that prevents the light from passing through the spaces between microlenses directly to the sensor. This increases the image contrast of the detected spotfield and improves the instrument accuracy, especially in the case of strong wavefront deformations. The wavelength range is not restricted (no AR coating) and covers the full sensitivity range of the Silicon CCD detector of 300 - 1100 nm (with largely reduced sensitivity at the edges). Taking into account that such a chrome mask cannot be anti-reflection coated, and may reflect up to 25% of the input light back into your measurement setup. It can be helpful to tilt the sensor a bit or insert an attenuator in order to reduce the amount of light reflected back into your measurement setup.

The WFS comprise a CCD camera and a microlens array that is mounted at a defined distance in front of the camera sensor chip. Each microlens generates a spot on the sensor surface. The spot centroid position depends on the wavefront gradient in front of the lens area.

Each microlens of the lenslet array collects the light incident to its aperture and generates a single spot on the detector plane (CCD camera) that is located at a distance of one focal length behind the lenslets. a) Planar wavefront. b)Distorted wavefront.

Coordinate Definitions

The WFS Series Wavefront Sensors use an orthogonal right-hand coordinate system (x, y, z) as shown to the left of the (A.0.1). Imagine that you are looking towards the light source. Then the x-direction points towards right, the y-direction points up, and the optical beam to be analyzed is propagating in z direction towards the entrance aperture of the Wavefront Sensor. The graphs in the Wavefront Sensor GUI (Spotfield, Beam View) are defined in the same way - the positive X axis points rigtwarrds and the Y ais points upwards.

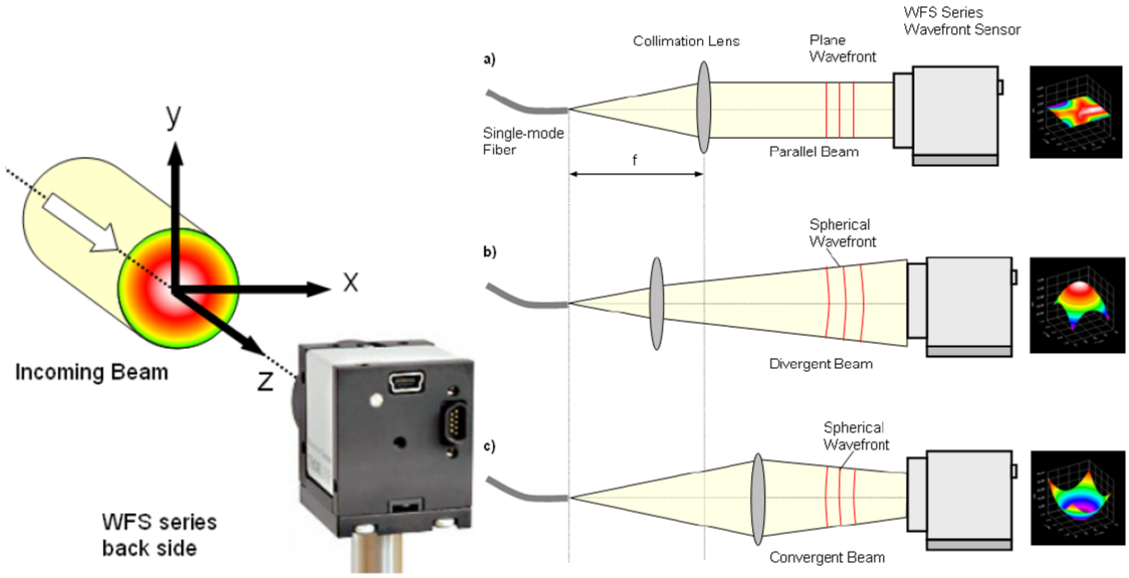

Figure A.0.1: Coordinate system for HSWFS.

In the 3D wavefront graph the beam's cross section in the X-Y plane is drawn at the bottom, and the Z axis points upwards. If the beam is coming from the bottom up, then the displayed 3D curve will represent the wavefront at the top of the beam.

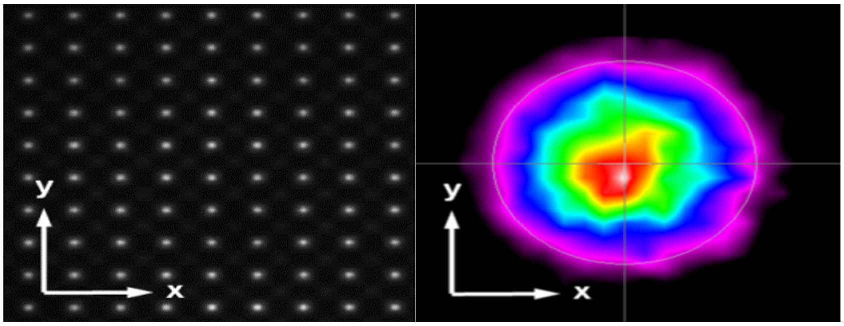

(a) (b)

Figure A.0.2: a) Spotfield graph and b) Beam view graph.

In the 3D wavefront graph the beam's cross section in the $X - Y$ plane is drawn at the bottom, and the Z axis points upwards. If the beam is coming from the bottom up, then the displayed 3D curve will represent the wavefront at the top of the beam.

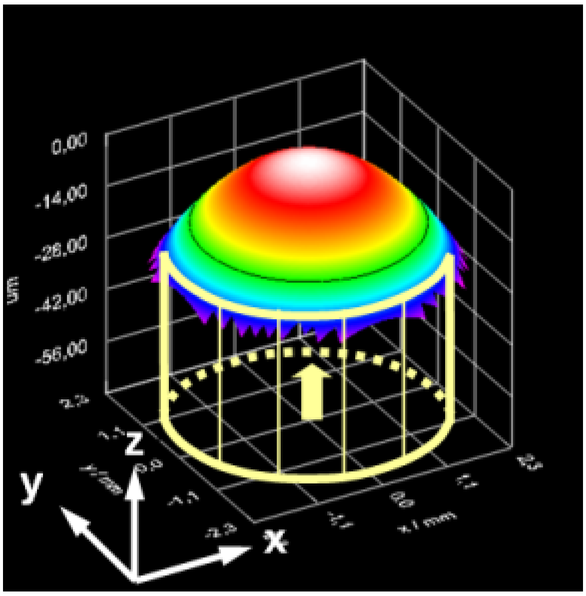

Figure A.0.3: 3-D wavefront graph

Zernike modes

The wavefront can be expressed in terms of a set of Zernike functions, also called Zernike modes.

$$W(x,y) = \sum_{0}^{\infty} c_n Z_n(x,y) \tag{A.0.1}$$

The wavefront $W(x,y)$ is derived from a summation of orthonormal Zernike functions $Z_n(x,y)$ weighted by their amplitudes or Zernike coefficients c_n. Generally a least square Zernike fit is done in order to determine the Zernike coefficients c_n.
A variety of definitions exist for these Zernike functions. The Zernike polynomials are recommended for describing wave aberration functions over circular pupils with a unit radius. Individual terms or modes of a Zernike polynomial are mutually orthogonal over the unit circle and are easily normalized to form an orthonormal basis. Zernike modes are conveniently expressed in either polar or rectangular coordinate reference frames. Rectangular coordinates are x any y both normalized to unit radius 1. Polar coordinates (ρ, θ) are normalized radius coordinate ρ and angular coordinate θ, whereas $\rho = r/a$ with r as physical radial coordinate and a as the pupil radius. The natural scheme for ordering of the Zernike modes is to use a double index corresponding to the radial order n and angular frequency m as following equation.

$$Z_n^m(\rho, \theta) \tag{A.0.2}$$

$n \geq 0$ Radial order
$|m| \leq n$ Angular frequency

$\rho \leq 1$	Normalized radial coordinate
$\theta(0..2\pi)$	angular coordinate
r	physical radial coordinate
a	physical pupil radius

Zernike polynomials have three properties that distinguish them from other sets of orthogonal polynomials.

- First, they have simple rotational symmetry properties that lead to a polynomial product of the form

$$R(\rho)G(\theta'), \tag{A.0.3}$$

where $G(\theta')$ is a continuois function that repeats itself every 2π radians and satisfies the requirement that rotating the coordinate system by an angle α does not change the form of the polynomial. That is,

$$G(\theta' + \alpha) = G(\theta')G(\alpha). \tag{A.0.4}$$

The set of trigonometric functions

$$G(\theta') = e^{\pm im\theta'} \tag{A.0.5}$$

where m is any positive integer or zero, meets these requirements.

- The second property of Zernike polynomials is that the radial function must be a polynomial in ρ of degree n and contain no power of ρ less than m.
- The third property is that $R(\rho)$ must be even if m is even, and odd if m is odd.

The radial polynomials can be derived as a special case of Jacobi polynomials, and tabulated as $R_n^m(\rho)$. Their orthogonality and normalization properties are given by

$$\int_0^1 R_n^m(\rho)R_{n'}^m(\rho)\rho d\rho = \frac{1}{2(n+1)}\delta_{nn'} \tag{A.0.6}$$

and

$$R_n^m(1) = 1. \tag{A.0.7}$$

It is convenient to factor the radial polynomial into

$$R_{2n-m}^m(\rho) = Q_n^m(\rho)\rho^m, \tag{A.0.8}$$

where $Q_n^m(\rho)$ is a polynomial of order $2(n-m)$.$Q_n^m(\rho)$ can be written generally as

$$Q_n^m(\rho) = \sum_{s=0}^{n-m}(-1)^s \frac{(2n-m-s)!}{s!(n-s)!(n-m-s)!}\rho^{2(n-m-s)}. \tag{A.0.9}$$

In practice, the radial polynomials are combined with sines and cosines rather than with a complex exponencial.

B Procediment for to corrode ITO lamines

1. Cover the region where you want to keep the ITO film with insulation tape. The tape should be securely fastened with no bubbles.
2. Mix Zinc powder in water until you have a paste. Place the paste in the region of the ITO film to be corroded so that it covers the entire ITO.
3. Dry the Zinc paste well. Use a hair dryer for this.
4. Quickly introduce (1 second) the sheet into 37% pure hydrochloric acid (undiluted). Repeat several times until the Zinc is corroded (2 or 3 times).
5. Rinse well with water.
6. If the process was carried out correctly, the sheet should be left with white residue that comes out easily when passing the finger. Then remove the insulation tape, and the sheet can undergo a typical cleaning process.